Simulating Magnetic Islands of the H-1NF Heliac using the MHD Equilibrium code HINT

A thesis submitted for the degree of
Doctor of Philosophy
of the Australian National University

Sally Stevens Lloyd

August 10, 2003

The work contained in this thesis is my own original research, except where explicitly stated otherwise. Any material take from other references is acknowledged.

Sally S. Lloyd
August 10, 2003

Acknowledgements

I would like to thank the people and organisations who supported me in this endeavour. In particular I would like to thank my supervisor, Henry Gardner, for his invaluable advice, direction, support and encouragement. My understanding of the theory was aided by several enlightening discussions with Bob Dewar. I would like to thank Takaya Hayashi for making the HINT code available, and for several helpful discussions about it. Computing facilities (a Fujitsu VPP300 and an AlphaServer SC) were provided through the ANU Supercomputer Facility.
The Australian government provided financial support in the form of an APA scholarship.
Rowena Ball gave several helpful comments on the thesis drafts.
Ben and André helped with printing and compilation at the last minute.
Many thanks to Rodney for his emotional support during this time, seeing me through the worst of my doubts and fears

Abstract

HINT was found to be inefficient at relaxing pressure within magnetic islands in low shear stellarators. A modification to the pressure relaxation step was developed to improve the computation speed in this situation. The method is described and shown to increase the convergence speed by up to a factor of 50, without any loss of accuracy.

Using this modification, HINT was applied to calculating equilibrium magnetic fields of the H-1NF Heliac, for several configurations, some of which included islands. The response of the magnetic islands to increases in pressure was investigated for several different configurations of H-1NF over a range of $<\beta>$ up to 3%. These results were compared to the predictions of a theory developed by Cary & Kotschenreuther (1985), Hegna & Bhattacharjee (1989) and Bhattacharjee *et al.* (1995) which considers the contributions to the island width from linear resonant currents and from non-linear resonant currents that develop in response to the island.

Comparisons were made between HINT equilibria with islands and closely related fields without islands which gave insight into the relative importance of the linear resonant currents, the non-linear resonant currents and also into the contribution of global resonant currents, which were not included in the theoretical calculations. The extent to which HINT can model each of these currents is discussed in the light of these results.

Contents

CHAPTER 1

Introduction

Fusion energy is a promising candidate for supplying the world with abundant, safe, clean and sustainable power, providing a solution to the looming world energy crisis. Fusion is made possible by the ability to contain extremely hot hydrogen plasmas within specially shaped magnetic fields. Minimising the diffusion rate of plasma out of these magnetic 'bottles' is essential to achieving a break-even point where the excess energy output from the fusion reaction can be used to generate electricity. Islands and stochastic regions can develop in the magnetic field which substantially degrades plasma confinement. The growth of these islands needs to be better understood via analytic theory, computer simulations and experimental studies so that mechanisms to control them can be developed.

1.1 Why the world needs fusion energy

World energy reserves of fossil fuels amount to 3.5×10^{22} Joules, mostly in the form of low quality coal (T.J. Dolan *et al.* (1995)). At current consumption rates these could continue to provide 85% of global energy consumption for 120 years. However energy demands are increasing rapidly, with the World Energy Council predicting electricity use to increase between 50% and 75% by 2020 (Priddle (1997)). The expected increase in energy consumption would deplete fossil fuel reserves in under 60 years, with significant risk of climate change from the associated release of carbon dioxide. Increased efficiency and conservation measures can reduce energy consumption in the richest countries in the world, but this will be offset by large increases in consumption among poorer countries unless their economic development is forced to stagnate.

The proportion of energy provided by alternative energy sources needs to be increased quickly. The main alternative energy candidates are hydro, solar, wind, biomass, fission and fusion. Hydro-electricity currently provides 6% of global energy but is unlikely to increase significantly (Mourogov (1997)) since most of the viable dam sites are already in use. Solar, wind and biomass all have high space requirements. They currently supply less than 0.1% of the world's energy and while this proportion is increasing rapidly they are only expected to play a minor role in global energy supplies for the foreseeable future (Priddle (1997)). Fission reactors currently provide about 6% of global energy supplies and could expand their contribution.

However, uranium is a finite resource; at current rates of use, known uranium deposits would last 60 years (Priddle (1999)). The reserves would be depleted much more quickly if fission was to replace a substantial portion of the power currently provided by fossil fuels. The efficiency of fuel use could be increased up to 70 times by the improved fuel recycling and the change-over to fast breeder reactors which have been avoided in the past because of fears about safety, and nuclear weapons proliferation (Mourogov (1997)). This use of improved fission reactors could extend the deadline on the world energy crisis until 2100.

The deuterium from just one litre of water, fusing to give helium could generate as much energy as the combustion of 300 litres of gasoline (T.J. Dolan *et al.* (1995)). The most accessible fusion reaction involves deuterium and tritium:

$$^{2}_{1}\mathrm{H} + ^{3}_{1}\mathrm{H} \rightarrow ^{4}_{2}\mathrm{He} + \mathrm{n} + 17.62\mathrm{MeV} \tag{1.1}$$

The high Coulomb-repulsion barrier must be overcome with kinetic energy from thermal motion. An ideal temperature at which to run this reaction is 20keV, over 200 million degrees (Cottingham & Greenwood (1986)). Magnetic confinement or inertial confinement are the only viable containment option at these temperatures.

While deuterium for the above reaction is easily extracted from sea-water the tritium is radioactive and has no natural abundance. It would need to be manufactures by exposing lithium to the fast neutrons produced by the deuterium-tritium reaction (Cottingham & Greenwood (1986)):

$$^{7}_{3}\mathrm{Li} + \mathrm{n} + 2.46\mathrm{MeV} \rightarrow ^{3}_{1}\mathrm{H} + ^{4}_{2}\mathrm{He} + \mathrm{n} \tag{1.2}$$

$$^{6}_{3}\mathrm{Li} + \mathrm{n} \rightarrow ^{3}_{1}\mathrm{H} + ^{4}_{2}\mathrm{He} + 4.8\mathrm{MeV} \tag{1.3}$$

Lithium availability is likely to limit the fully sustainable use of this reaction (Holdren (1978)) but easily available resources will last for several hundred years at least. The experience gained from using these reactors should enable us, within this time frame, to take the next step to using a deuterium-only reaction:

$$^{2}_{1}\mathrm{H} + ^{2}_{1}\mathrm{H} \rightarrow ^{3}_{2}\mathrm{He} + \mathrm{n} + 3.27\mathrm{MeV} \tag{1.4}$$

$$^{2}_{1}\mathrm{H} + ^{2}_{1}\mathrm{H} \rightarrow ^{3}_{1}\mathrm{H} + \mathrm{p} + 4.03\mathrm{MeV} \tag{1.5}$$

Reaction rates at a temperature of 20keV, for deuterium-deuterium reactions are only a hundreth of the rate for the deuterium tritium reaction and only become comparable at temperatures higher than 1000 keV (Cottingham & Greenwood (1986)).

To allow for inefficiencies in power conversion to electricity, a reactor needs to achieve greater energy output from the fusion reaction than the energy input needed to maintain temperature. This is known as the Lawson criteria which provides a measure of how close an experiment's deuterium density, ρ_d, and average particle confinement time, t_c, are to what would be needed for a reactor. For a deuterium-tritium reaction at 20keV the Lawson criteria is $\rho_d t_c > 10^{19}\mathrm{m}^{-3}s$(Cottingham & Greenwood (1986)). Inertial confinement achieves very high densities but has extremely low confinement times. Magnetic confinement tends to use quite low density ($\rho \approx 10^{20}$) and tries to maximise particle confinement times.

1.2 Magnetic confinement devices: tokamaks and stellarators

Charged particles in a uniform magnetic field move in a spiral motion along the field lines with a gyro-radius (or Larmor radius) of $\rho = mv_\perp/qB$. This still holds approximately true for non-uniform fields as long as the amount of field change within a Larmor radius is small (Hazeltine & Waelbroeck (1998)).

This motion allows us to trap the charged particles of a plasma by shaping the magnetic field so that field lines form closed loops. It is not essential to confinement that the field lines exactly close on each other to form finite loops. To confine a set of charged particles within a set volume it is merely necessary that no field lines cross the volume boundary. Because a magnetic field must be divergence free, only volumes that are topologically toroidal can satisfy this condition. This principle forms the basis of a variety of toroidal magnetic confinement devices.

Containing the magnetic field lines within a volume is not sufficient to contain the plasma indefinitely. The toroidal field is necessarily nonuniform and this leads to charged particles drifting slowly across field lines. Collisions between particles will also cause plasma to diffuse across field lines. In addition, currents produced by the movements of the charged particles may change the magnetic field so that the field lines are not confined.

Secondary drifts due to the nonuniformity of the magnetic fields will cause particles to escape from this magnetic field configuration. The particle confinement can be restored by adding a poloidal field, making the field lines spiral around a central magnetic axis. The amount of twist added with a poloidal field is measured by the rotational transform, ι, which is the average number of poloidal transits of a field line for each toroidal transit. The magnetic field lines now form nested toroidal surfaces instead of being simple closed loops. This field line shape allows the averaging and cancellation of drifts over the magnetic surface. Generally the gyro-center of a particle's motion will also form a toroidal surface, displaced from the magnetic surface by less than a Larmor radius (White (1989)). In the absence of collisions, the particle will be perpetually confined.

In a tokamak, the poloidal field component is generated by currents within a plasma. This plasma current has to be driven inductively which makes tokamaks pulsed, rather than steady-state devices. This limits particle confinement times and also complicates the capture of fusion energy as heat and its conversion into electricity.

The field in a tokamak is very nearly axisymmetric, which simplifies calculations of equilibrium magnetic fields and particle orbits and allows many aspects to be determined analytically. Axisymmetry guarantees that the field lines form nested toroidal flux surfaces. Magnetic flux surfaces can be used as the basis of a coordinate system in which the field-line motion becomes trivial and other calculations are also simplified. One of these straight-field-line coordinate systems (Boozer (1981)) uses the contained toroidal flux, ψ, to label the flux surfaces, with a toroidal coordinate, ϕ, and a poloidal coordinate θ chosen so that the field can be written:

$$\mathbf{B} = \nabla\psi \times \nabla\theta + \iota(\psi)\,\nabla\phi \times \nabla\theta \tag{1.6}$$

These coordinates are used throughout this thesis.

In a stellarator, the poloidal field is generated with external currents which removes the problems of current induction and pulsed operation. The magnetic field generated in this way cannot be axisymmetric and the three-dimensionality of the magnetic field brings its own problems. For some stellarators, approximations can be made to reduce the dimensionality of the problem and make it analytically tractable but these are not generally applicable and don't capture all the relevant phenomena. Advances in faster computers have allowed the development of numerical methods to perform three dimensional equilibrium, stability and transport calculations in stellarators.

One characteristic of a fully three-dimensional system is that nested magnetic surfaces are not guaranteed to exist. Stochastic regions or island topologies are generally found over at least some of the plasma region. KAM theory shows that the majority of the plasma volume in a three dimensional torus can contain nested flux surfaces. Small perturbations from an ideal, integrable system give narrow bands of chaotic and island topologies around each rational value of the rotational transform.

1.3 Islands and transport

Islands and stochastic regions are unavoidable in stellarator fields. However, their size can be minimised so that they do not significantly deteriorate confinement.

Diffusive plasma transport is characterised by rapid (or instant) transport parallel to the magnetic field and slow diffusion perpendicular to the magnetic field. This causes the pressure to be constant on a flux surface but allows a pressure gradient to be maintained across magnetic surfaces depending on plasma source terms and the cross-field diffusion rate. Stochastic field-lines cover a volume rather than being restricted to a surface. Very rapid transport along the field lines makes the pressure profile within this stochastic volume flat. In order to maintain the same peak pressure as a field without stochastic regions the pressure gradient in the remaining regions of nested flux surfaces must be higher to compensate for the regions of flat pressure. This will increase diffusive transport losses.

Magnetic islands have flux surfaces within them and can sustain some pressure gradient across these surfaces. In general, unless there is a significant plasma pressure source within an island, the pressure will be flat across the island. Flat pressure across islands will have a similar effect to the regions of flat pressure caused by stochastic field lines, in that pressure gradients in other sections of the plasma will be increased thus increasing total diffusive transport losses.

Cross-field diffusion is due to collisions between particles (with frequency ν) causing particles to shift their gyro-center to a new magnetic field line. The diffusion coefficient resulting from this process is $D = 1/2\nu\rho^2$. Regions of stochasticity less than a gyro-radius wide will have minimal effects on total transport.

With the overlapping of many small islands and stochastic regions surrounding each rational surface, large regions of connected chaos can form extending across

most of the plasma. Plasma is no longer well contained by this field. This can occur as a result of plasma currents which gives a maximum effective pressure that a given stellarator can reach, regardless of energy input.

The study of how islands grow with increasing plasma pressure, how much stochasticity develops at the separatrix and when island overlap leads to large regions of connected chaos is thus very important for optimising stellarator designs to reduce transport and increases the maximum achievable pressure.

1.4 The role of this work in understanding islands

There are two aspects to this thesis. One is the modifications I have developed and tested that significantly increase the speed and accuracy with which the HINT code is able to calculate equilibrium magnetic fields of low shear stellarators with islands. This allows many computational studies of islands at within many different magnetic configurations to be carried out.

In Chapter 3 I outline the theory behind MHD equilibrium codes, summarise the main differences among those available and give details of the HINT code. In Chapter 4 I explain the method I use to improve the speed of HINT's pressure relaxation step and show that the speed is improved without compromising any convergence measures either within this step or for the HINT method overall.

The other main aspect of this thesis is a comparison of the relative contributions of different portions of the plasma current to the growth of islands. I compare contributions that theory predicts these currents have on island growth, with the contributions these currents make to island widths measured in HINT calculations, for some configurations of the H-1NF Heliac. I consider that the plasma current is composed of global (or linear) resonant-currents, global-nonresonant currents and local (or non-linear) resonant currents. These currents are considered separately in analytic theories of the development of magnetic islands introduced in Chapter 2.

Chapter 5 gives details of the H-1NF Heliac configurations that were studied and shows how the HINT simulations with my improved pressure relaxation algorithm was applied to these configurations. It also describes the methods that were used to calculate measures of the equilibrium configurations used in the theoretical calculations. Chapter 6 gives general results of the equilibrium calculations for measures such as changes in magnetic axis profile, ellipticity and indentation of magnetic surfaces, rotational transform profile, magnetic well depth and perpendicular and parallel current distribution and plasma velocity profile. These results are compared with expectations from simple analytic theories or previous results.

Chapter 7 examines the changes to magnetic fields and currents near rational surfaces in the HINT simulations. It analyses these results to determine how much of a role each of the types of plasma current could play in producing the changes to field-line topology. Comparisons are made with theoretical predictions of island growth. In Chapter 8, I discuss the conclusions of this work and their implications. I also suggest where further investigations are needed to clarify aspects of island growth and and stochastic field-line development raised by this study.

CHAPTER 2

Theory of Magnetic Islands

There is no guarantee that nested, toroidal magnetic surfaces exist in a fully three dimensional magnetic field. The best that can be achieved is a field with many narrow island chains, each with a thin stochastic separatrix, separated by regions characterised by nested, toroidal, flux surfaces. If the islands and any stochastic regions are sufficiently narrow, with a majority of intact flux surfaces, then plasma transport will not be significantly degraded compared to an ideal magnetic field entirely characterised by nested flux surfaces. Studies of island behaviour in vacuum and finite-pressure-equilibrium magnetic fields aim to predict the size of large islands and to determine criteria for when the many small island chains will overlap to form large regions of stochasticity.

Section 1 shows how a resonant radial perturbation in the magnetic field distorts the flux surfaces at a rational surface into an island topology. This explains why some magnetic islands and stochastic regions are always present in stellarators. Section 2 explores various island topologies using some simple map models for the field lines. All of the topologies shown here have been seen in simulations of the H-1NF heliac. Aspects of the effects of various magnetic field-line topologies on plasma transport will be discussed. Section 3 draws an analogy to the differential equations governing a simple pendulum and makes quantitative predictions of island size and other properties depending on various characteristics of the field perturbation. In Sect. 4 the field line invariant calculation is extended to the most general perturbation that preserves the divergence free nature of a magnetic field.

Section 5 gives a linear MHD theory for islands, with field perturbations arising from plasma currents generated from the $\mathbf{J} \times \mathbf{B} = \nabla p$ constraint. This section explains why ideal MHD predicts that singular and arbitrary δ function currents form at rational surfaces. Resistive MHD does not accept singular currents but will allow the flux surface topology to change and magnetic islands to develop resolving the anomaly of singular currents. Magnetic field perturbations are associated with perturbation currents either within the plasma or in external coils. In Sect. 6 I explore the relationship between harmonics of the current perturbations and harmonics of the vector potential of the magnetic field in cylindrical coordinates. This is a much simplified case but gives some insights and scalings for field perturbations due to real currents. The last section expounds a nonlinear theory of island development due to Cary & Kotschenreuther (1985), Hegna & Bhattacharjee (1989) and Bhat-

tacharjee *et al.* (1995). The presence of an island will disturb the currents giving the magnetic perturbation that causes the island. This needs to be treated self consistently and solves the problem of the arbitrary current in the linear theory of ideal MHD.

2.1 Perturbing an ideal field to create islands

The ubiquity of islands and stochastic regions in stellarator magnetic fields can be demonstrated by adding a small perturbation to an ideal magnetic field consisting of nested flux surfaces.

Consider an ideal equilibrium magnetic field with toroidally nested flux surfaces. It can be written in straight field-line coordinates (ψ, θ, ϕ) as:

$$\mathbf{B_0} = \nabla\psi \times \nabla\theta - \iota(\psi)\,\nabla\psi \times \nabla\phi$$

In these coordinates the magnetic field has field lines determined by the equations :

$$\frac{d\theta}{d\phi} = \iota(\psi),$$

$$\frac{d\psi}{d\phi} = 0$$

We assume this field has a flux surface, ψ_R, with rational rotational transform $\iota(\psi_R) = m/l$, where m and l are integers. I will refer to this as the rational surface. A field line on the rational surface will close on itself after l periods. We introduce a particular radial field perturbation $(\mathbf{B_1})$, which is resonant with this rotational transform.

$$\mathbf{B_1} = C\sin(l\theta - m\phi)\,\nabla\theta \times \nabla\phi, \tag{2.1}$$

It is convenient to replace θ with the new coordinate $a = \theta - (m/l)\phi$ which rotates with the field lines on the rational surface. On the rational surface, field lines maintain constant values of a and close on themselves after l periods in ϕ. With this field perturbation and coordinate transformation the field-line equations become:

$$\begin{aligned} \frac{d\theta}{d\phi} &= \iota(\psi) \\ \frac{d\psi}{d\phi} &= C\sin(la) \end{aligned} \tag{2.2}$$

The field-line equations are dependent on only two coordinates, a and ψ, which guarantees that the field line motion under this perturbation is integrable and that an invariant of the motion can be found. The rotational transform in the vicinity of a small island can be approximated as linearly dependent on ψ, and with this approximation the field lines equations are similar to the equations governing the motion of a simple pendulum. With linear rotational transform the field lines are

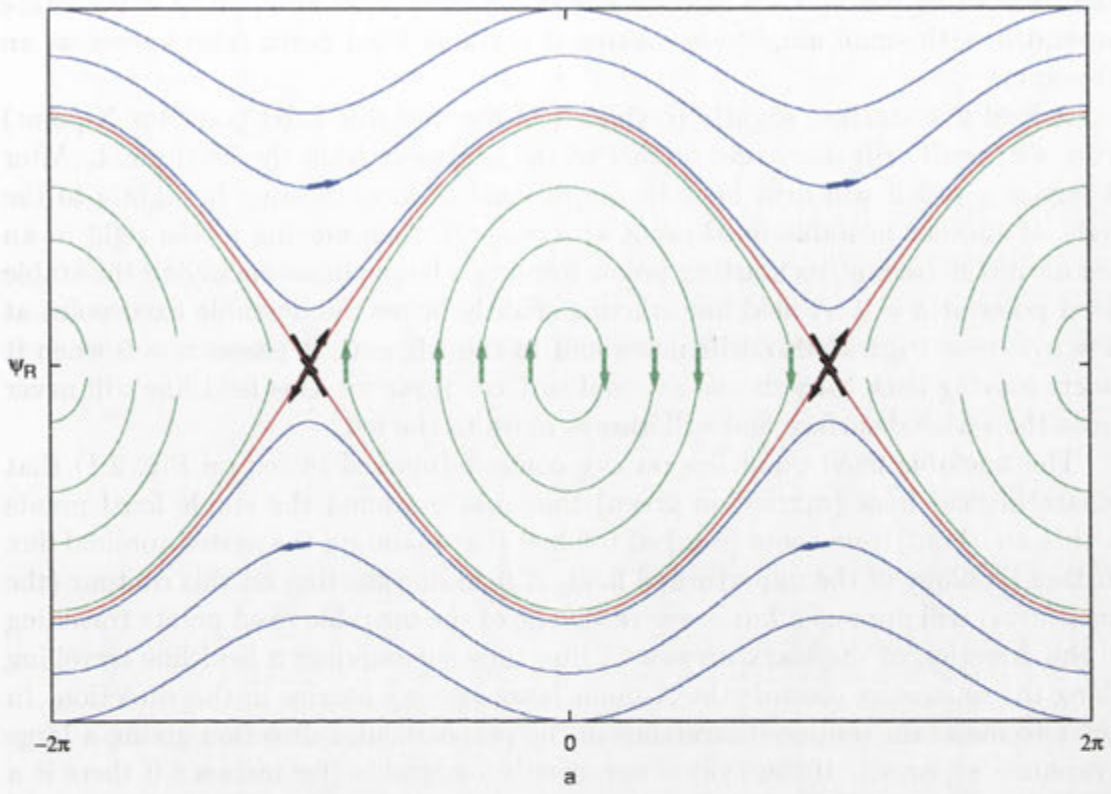

Figure 2.1: contours of the field-line invariant under the influence of a single resonant perturbation. Arrows show the direction of field-line motion along these contours.

constrained to surfaces defined by the invariant χ, analogous to the total energy of a pendulum.

$$\chi = \frac{1}{2}(\psi - \psi_R)^2 + \frac{C_R}{l\,\iota'_R}\cos(la)$$

Calculations using the pendulum analogy will be discussed in more detail in Sect. 3, here I focus on the topological effects of the resonant perturbation. The surfaces of constant χ form an island structure shown in Fig. 2.1.

Let us examine the qualitative behaviour of field lines affected by the resonant perturbation. On the rational surface most of the line of fixed points is disturbed by the resonant perturbation. Only those points where $\mathbf{B_1}$ is zero remain fixed. The fixed points fall into two classes, stable or unstable, depending on the behaviour of nearby field lines. In Fig. 2.1 a field line starting slightly to the right of the fixed point at $a = 0$ will drift downwards. As its ψ decreases the rotational transform changes and the field line starts to drift to the left. In this case the field line soon moves past $a = 0$ where it starts to drift back to the rational surface ψ_R. As it moves upward from ψ_R, ι is more than m/l and the field line drifts back to the right. When it again moves past $a = 0$ it drifts back towards the rational surface

and its starting point. Thus field lines near the fixed point at $a = 0$, $\psi = \psi_R$ rotate around it with small amplitude making it a stable fixed point (also known as an O-point).

A field line starting slightly to the left of the unstable fixed point (or X-point) at $a = \pi/l$ will drift down and further to the left, away from the fixed point. After it passes $a = 0$ it will drift back to the rational surface, crossing it slightly to the right of another unstable fixed point at $a = -\pi/l$, then moving to the right in an arc until it is back at its starting point, forming a large ellipse encircling the stable fixed point at $a = 0$. A field line starting slightly below the unstable fixed point at $a = \pi/l$, $\psi = \psi_R$ will also drift down and to the left until it passes $a = 0$ when it starts moving back towards the rational surface. However, this field line will never cross the rational surface and will always move to the left.

The unstable fixed point lies on a χ contour (marked in red on Fig. 2.1) that separates field lines (marked in green) that rotate around the stable fixed points within an island, from those (marked in blue) that maintain the nested toroidal flux surface topology of the unperturbed field. A field line starting on this contour (the separatrix) will approach but never reach one of the unstable fixed points travelling in the direction of the black arrows. A flux tube surrounding a field line travelling along the separatrix towards the X-point becomes very narrow in this direction. In order to maintain volume it stretches in the perpendicular direction giving a large Lyapunov exponent. If the field is not exactly integrable (for instance if there is a small non-resonant perturbation) chaotic field line behaviour will develop around the X-point and separatrix (Chirikov (1979)).

In general a stellarator magnetic field will include perturbations to resonate with any rational rotational transform. The perturbations may be intrinsic to the design, may come from minute errors in the construction of the device or may be due to plasma current at finite β. At each of the infinitely many rational surfaces within the plasma there will be a narrow island chain with a chaotic separatrix. The higher the order of the rational surface the thinner the island chain but the closer together rational surfaces of this order are. Island chains for higher order rationals are thinner for the same perturbation strength, also the resonant perturbation strengths tend to be smaller.

There are two parts to avoiding containment deterioration due to magnetic islands. The first is to avoid large islands around low order rationals. The second is to ensure that the island sizes for high order rationals are sufficiently small to stop them overlapping to form large regions of connected chaos.

2.2 Examining island topologies using maps

Perturbed field-line topology can be illustrated with a simple twist map. A toroidal field is modelled as a discrete map by considering the sequential crossings of some toroidal plane. The field lines of an integrable magnetic field with rotational transform varying linearly with ψ, can be modelled by the mapping:

$$\theta_n = \theta_{n-1} + A\psi_{n-1} + D \tag{2.3}$$

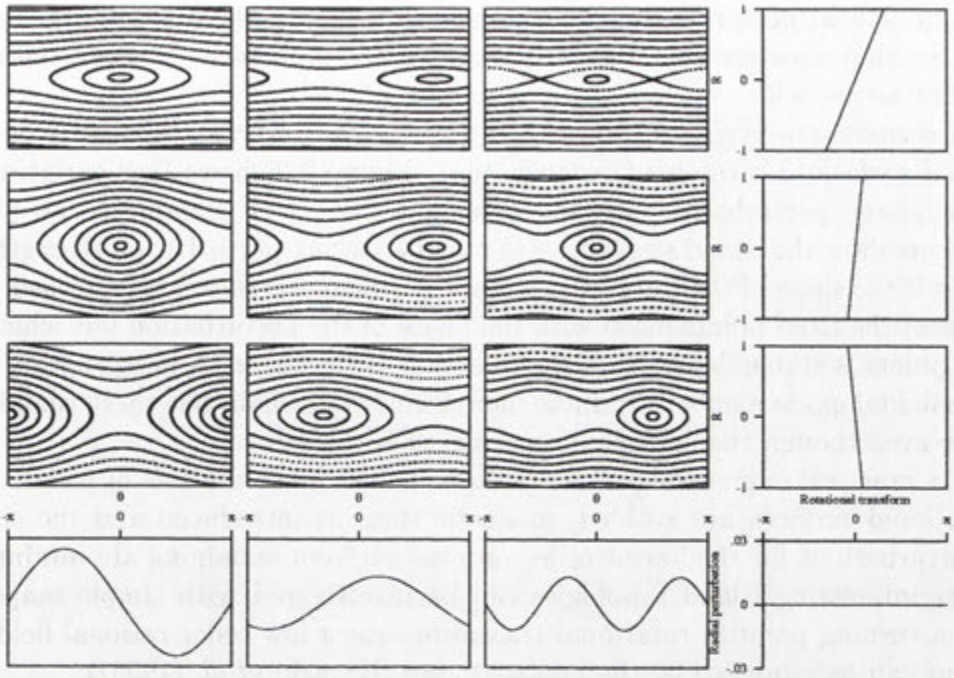

Figure 2.2: Twist maps with various values for shear and size and phase of perturbation

$$\psi_n = \psi_{n-1}$$

At values of ψ where the rotational transform $\iota = A\psi + D$ is zero or some integer multiple of 2π, the map will have a fixed point (in fact, a line of fixed points). Values of ι equal to rational multiples of 2π will form periodic orbits cycling over the order of the rational. We can add a radial field perturbation sinusoidally varying in ϕ as

$$\psi_n = \psi_{n-1} + C\sin(l\theta_n + E) \tag{2.4}$$

Now consider a fixed point of the Eqn. 2.4. It will remain a fixed point only if the radial perturbation at this point is zero (i.e. for $l\theta_n + E = 0, \pi$). The line of fixed points is reduced to a finite set of fixed points alternately stable and unstable. The behaviour of points near the fixed points follows the behaviour of perturbed field lines discussed in the previous section. Points rotate around stable fixed points with a separatrix through the unstable fixed points dividing the island region from the 'nested flux surface' region. There are differences due to the discrete steps of the mapping compared to the field line. Points travelling along the separatrix may jump past the stationary point and the single resonant perturbation can cause additional islands at other ψ. Chaotic trajectories near the separatrix are also possible. The difference between the mapping and a continuous treatment increases if A, D and C are all increased, which increases the effective step size of the mapping. The differences in the discrete mapping are similar to the effects of having many

harmonics of field perturbation to the ideal field. In the mappings shown in this section the step sizes are kept small to minimise the differences between the maps and a continuous field.

This simple map gives a quick way to explore the response of field lines near a rational surface to a resonant perturbation. Figure 2.2 shows how variations in magnetic shear, perturbation size and poloidal mode effect island size and phase. These maps show the island size increases with increasing perturbation strength but decreases if the slope of the rotational transform (magnetic shear) is increased. The positions of the fixed points move with the phase of the perturbation but which set of fixed points is stable depends on the direction of the shear. A perturbation with higher poloidal mode number produces more islands in a chain but these islands are narrower even though the perturbation strength is the same.

In the practical engineering of stellarators, to minimise the size of islands, low order rational surfaces are avoided, magnetic shear is introduced and the size of error perturbations for the lowest order rational surfaces remaining are minimised.

Other interesting island topologies can be investigated with simple maps. If there is a turning point in rotational transform near a low order rational field-line behaviour can be modelled by the nontwist map (Hayashi *et al.* (1995)):

$$\theta_n = \theta_{n-1} + A\psi_{n-1}^2 - D \tag{2.5}$$

$$\psi_n = \psi_{n-1} + C\sin(l\theta_n) \tag{2.6}$$

With A positive and D there are two values of ψ with zero rotational transform and two distinct island chains form at these rational surfaces. These island chains have opposite phases because the direction of magnetic shear changes. As D decreases the two island chains get closer together and the separatrices of the islands eventually join. Decreasing D further will change island topology as shown in Fig. 2.3. When $D = 0$ the turning point in iota and the rational surface coincide the island size shrinks to zero but there is still a fixed point and separatrix, and substantial perturbation of the surrounding flux surface. Decreasing D further removes the separatrix and reduces the perturbation in the flux surface, with the perturbation now sinusoidal.

The island topology at a turning point in ι is quite different from that which occurs when islands of different ι overlap. The map I use to illustrate this is:

$$\theta_n = \theta_{n-1} + A\psi_{n-1} + E \tag{2.7}$$

$$\psi_n = \psi_{n-1} + C\sin(l\theta_n) + D\sin(k\theta_n) \tag{2.8}$$

This map has one island chain at $A\psi + E = 1/l$, and another at $A\psi + E = 1/k$. When the islands are small they have little effect on each other, but when they are large enough to overlap a large stochastic region forms between and around them. Figure 2.4 shows the interaction of a 1/3 island ($l = 3$) with a 1/4 island ($k = 4$). The series of plots on the left of Fig.2.4 show the 1/3 island growing as C is increased with D=0. The series of plots in the middle of Fig.2.4 show the 1/4 island growing as D is increased with C=0. The series of plots to the right of Fig.2.4 shows the interaction of the islands when both perturbations are

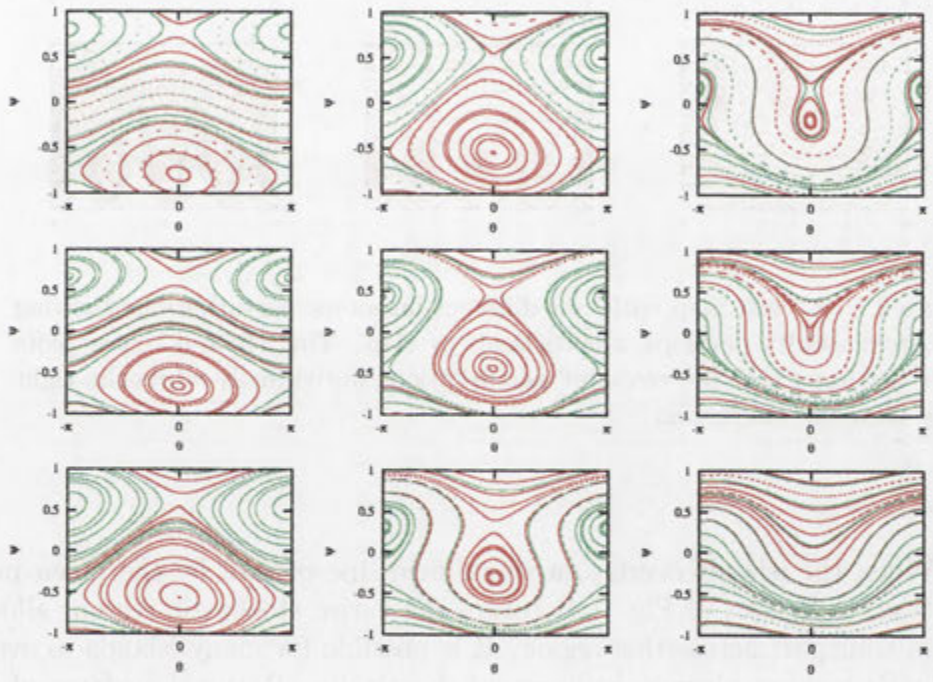

Figure 2.3: Non-twist maps showing the effect of varying the position of the turning point in rotational transform. D decreases top to bottom and left to right reaching zero at the middle right plot.

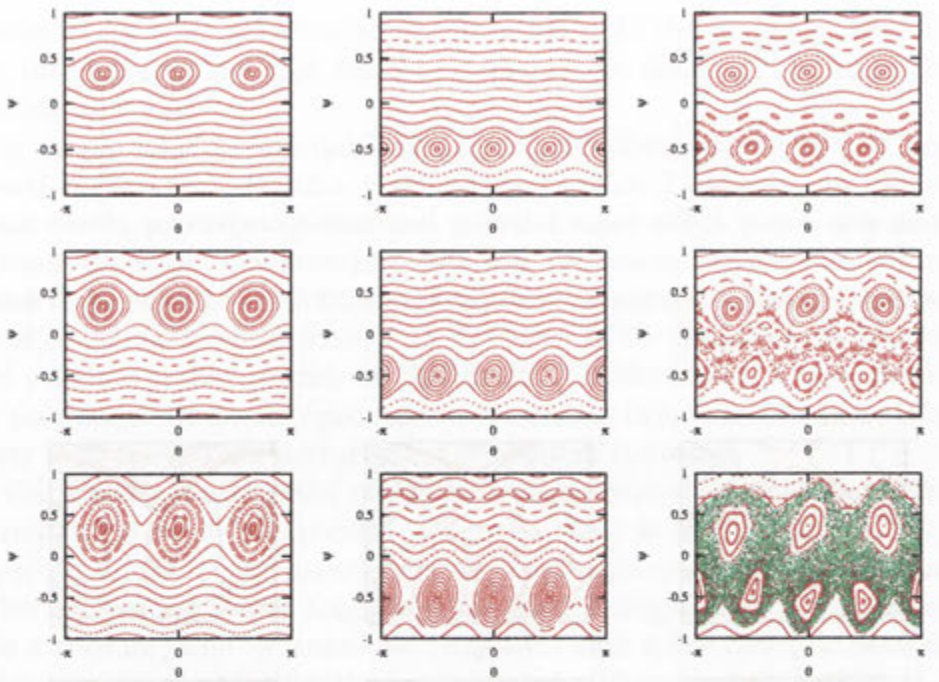

Figure 2.4: A twist map with two different harmonic perturbations showing how stochasticity develops when islands overlap. The left and center plots show the impact of the resonant perturbations individually while the right plots show the interaction

present. When the islands overlap, a single field line (shown by the green points in the bottom right plot of Fig. 2.4) covers the entire stochastic region, allowing fast plasma transport across this region. It is possible for many islands to overlap in this way decreasing plasma confinement drastically. Rational surfaces of high mode occur densely throughout the plasma so it would be possible for islands at these surfaces to destroy confinement even at small individual island widths. For confinement to be possible it is necessary that the island size decrease with poloidal mode number very quickly so that, over most of the plasma, the island size is smaller than the distance between rational surfaces.

Another interesting topology occurs where two harmonics of a resonant perturbations are present at the same rational surface (Fig. 2.5). An example of this, with first and second harmonics of the $\iota = 0$ rational surface is modelled by the mapping:

$$\theta_n = \theta_{n-1} + A\psi_{n-1} \tag{2.9}$$

$$\psi_n = \psi_{n-1} + C\sin(\theta_n) + D\sin(2\theta_n) \tag{2.10}$$

The field-line topology depends both on the relative strengths of the two perturbations and on their phases. With $D = 0$ and $C > 0$ the first harmonic gives a single island with an O-point at $\theta = 0$ and an X-point at $\theta = \pm\pi$. With $C = 0, D > 0$

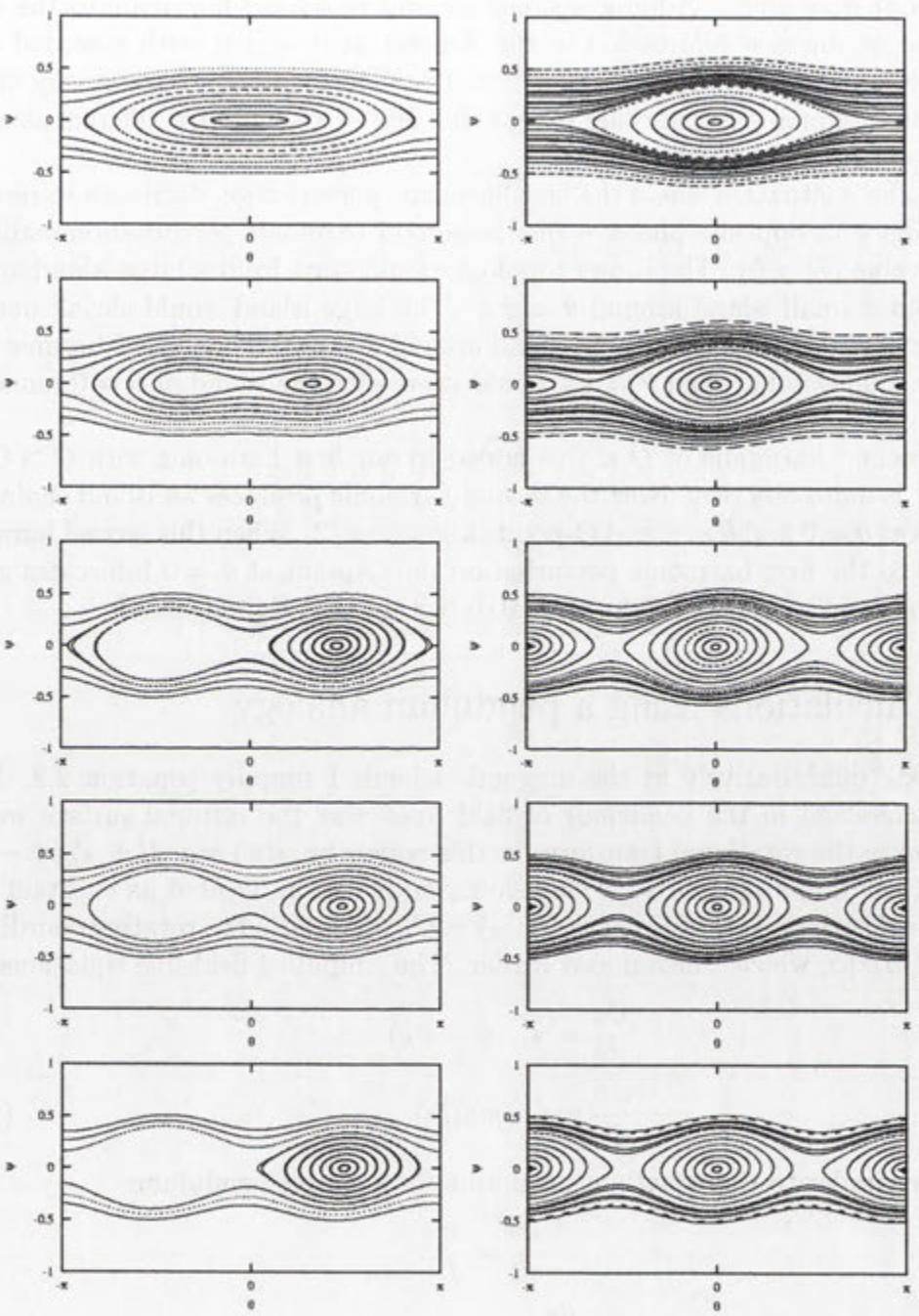

Figure 2.5: Twist maps with a second harmonic in addition to the main harmonic perturbation. The size of the second harmonic increases from the top plots to the middle plots and the size of the first harmonic decreases from the middle plots to bottom plots. The phase of the second harmonic is reversed for the right plots compared to those on the left.

the second harmonic gives two islands with O-points at $\theta = 0$ and $\theta = \pi$ and X-points at $\theta = \pm\pi/2$. Adding a small amount of second harmonic to the single harmonic produces a bifurcation of the X-point at $\theta = \pm\pi$, with a second small island developing with its O-point at $\theta = \pm\pi$. The island topology is very similar to a second harmonic island chain except that the two islands are different sizes and the X-points are not evenly spaced.

Consider a situation where the first harmonic perturbation decreases to zero and then grows with opposite phase, while the second harmonic perturbation maintains a small value ($D > 0$). The island topology would start from a large island around $\theta = 0$ and a small island around $\theta = \pm\pi$. The large island would shrink until, at $C = 0$, it was the same size as the island around $\theta = \pm\pi$. Then, as C became more negative, the island around $\theta = \pm\pi$ would grow with the island at $\theta = 0$ remaining small.

If a second harmonic of $D < 0$ is added to our first harmonic with $C > 0$, the topology is quite different. Now the second harmonic produces an island chain with X-points at $\theta = 0$ and $\theta = \pi$ and O-points at $\theta = \pm\pi/2$. When this second harmonic is added to the first harmonic perturbation the O-point at $\theta = 0$ bifurcates giving two islands and a figure of eight separatrix within the original island.

2.3 Calculations using a pendulum analogy

To look quantitatively at the magnetic islands I simplify equation 2.2. Since we are interested in the behaviour of field lines near the rational surface we can approximate the rotational transform in this region by $\iota(\psi) = m/l + \iota'_R(\psi - \psi_R)$. The perturbation strength is varying slowly so it can be treated as constant near the rational surface so that $C(\psi) = C(\psi_R) = C_R$. I also use the rotating coordinate, $a = \theta - (m/l)\phi$, which I introduced earlier. The simplified field-line equations are:

$$\begin{aligned} \frac{da}{d\phi} &= \iota'_R(\psi - \psi_R) \\ \frac{d\psi}{d\phi} &= C_R \sin(la) \ , \end{aligned} \tag{2.11}$$

which are similar to the equations of motion for a simple pendulum:

$$\begin{aligned} \frac{d\theta}{dt} &= \frac{v}{L}, \\ \frac{dv}{dt} &= g \sin\theta \ . \end{aligned}$$

The island region of the magnetic field is equivalent to oscillatory motion of the pendulum while the topologically unchanged region of the magnetic field is equivalent to circular motion of the pendulum.

To find the width of the island, I need an invariant for the field lines similar to total energy for a pendulum: $E = \frac{1}{2}mv^2 - mgR\cos\theta$. I choose :

$$\chi = \frac{1}{2}(\psi - \psi_R)^2 + \frac{C_R}{l\,\iota'_R}\cos(la) \tag{2.12}$$

and show that it must be conserved along a field line:

$$\begin{aligned}\frac{d\chi}{d\phi} &= (\psi-\psi_R)\frac{d\psi}{d\phi} - \frac{C_R}{l\,\iota'_R}\,l\,\sin(la)\frac{da}{d\phi} \\ &= (\psi-\psi_R)\,C_R\,\sin(la) - \frac{C_R}{\iota'_R}\,\sin(la)\,\iota'_R\,(\psi-\psi_R) = 0\ .\end{aligned}$$

The maximum of χ with $\psi = \psi_R$ (i.e. the maximum for an island surface which must pass through $\psi = \psi_R$) is $\chi_{\max} = |C/l\,\iota'_R|$ occurring at $a = \pi/l$ if $C\,\iota'_R > 0$. The largest deviation allowed in ψ for a field line with this χ occurs at $a = 0$:

$$\frac{1}{2}\delta\psi^2_{\max} + \frac{C}{l\,\iota'_R} = -\frac{C}{l\,\iota'_R}\ ,$$

giving

$$\delta\psi_{\max} = 2\sqrt{|C/(l\,\iota'_R)|}\ .$$

This result confirms our previous observation from the twist map that island size decreases with increasing magnetic shear and with poloidal mode number while increasing with perturbation strength.

The perturbation strength and magnetic shear only enter the flux surface invariant χ as the ratio $C/\,\iota'_R$, so changing magnetic shear and perturbation strength while keeping this ratio the same will not change the shape of flux surfaces. However it will change the motion of field lines within these flux surfaces. For the mappings we looked at earlier this is not true. There is some difference between the constant χ surface of the differential equations and the points in a discrete mapping. This difference disappears as $\iota'_R \to 0$, equivalent to reducing the step size of the discretisation. The two important topological differences arising from discretisation errors are an asymmetry and slant of the island surfaces and the creation of islands at other rotational transforms from aliasing effects.

Measurements of other characteristics of simple islands are also possible by analogy with the pendulum. For example, the frequency of rotation of field lines within an island, around the O-point, is related to the oscillation frequency of a pendulum. Consequently the island rotation frequency will approach a constant value near the centre of the island but tend to zero at the separatrix. The island rotation frequency near the centre of the island is calculated using the same method normally employed for the pendulum. Near the centre of the island $\psi \to \psi_R$, $a \to 0$ and $\sin(la) \to la$, reducing the field-line equations to a simple harmonic oscillator:

$$\frac{da}{d\phi} = \iota'_R x,$$

$$\frac{dx}{d\phi} = C_R n a$$

with angular frequency $w = \sqrt{|\,\iota'_R C_R l|}$ and period (in radians) of $\tau = 2\pi/\sqrt{|\,\iota'_R C_R l|}$. If $\iota'_R C_R > 0$ the island would be centred around $a = \pi, \psi = \psi_R$ with the magnitude

of the period unchanged. Substituting the expression for island width calculated earlier into this equation gives the period $\tau = 4\pi/(l\delta\psi_{\max}\, \iota'_R)$.

Low magnetic shear will increase the rotation period of the island. This can improve transport properties since a particle travelling along the field line may collide well before it completes a circuit of the island (Van Milligen *et al.* (1993)). However this large rotation period for islands will mean that HINT will have some difficulties in modelling MHD equilibrium islands in low shear stellarators. This will be discussed in more detail in Chapt. 4.

The island period can be used as a measure of island size. Rearranging the last equation gives:

$$\delta\psi_{\max} = \frac{4\pi}{l\tau\, \iota'_R}$$

This measure can be more precise, and less time consuming to calculate, than direct measurement of island width but is disturbed by the presence of odd topologies not considered in this simplified calculation. In particular, the addition of a second harmonic bifurcates the O-point and leads to an X-point at the island centre. For this topology the rotation period near the island centre becomes infinite.

Near the centre of the island the rotation period approaches the constant τ_0. However near the separatrix the period becomes infinite, as with a pendulum. For the simple pendulum, the variation in period across θ can be calculated from the series (Sears *et al.* (1987)):

$$\tau = 2\pi\sqrt{\frac{L}{g}}(1 + \frac{1^2}{2^2}\sin^2\frac{\theta}{2} + \frac{1^2 3^2}{2^2 4^2}\sin^4\frac{\theta}{2} + ...)$$

The corresponding expression for the island period is

$$\tau = \frac{2\pi}{\sqrt{l\, \iota'_R C_R}}(1 + \frac{1^2}{2^2}\sin^2\frac{la}{2} + \frac{1^2 3^2}{2^2 4^2}\sin^4\frac{la}{2} + ...)$$

2.4 Island widths for more general perturbations

The most general field perturbation introduced in the first section of this chapter is not necessarily divergence free, and so will not preserve the Hamiltonian nature of the field-line dynamics. The divergence of the field perturbation used in Sect. 1 is:

$$\nabla \cdot \mathbf{B_1} = \frac{\partial C(\psi)}{\partial \psi}\sin(l\theta - m\phi)/\mathcal{J} \tag{2.13}$$

Clearly $\mathbf{B_1}$ is not divergence free except when $C(\psi)$ is a constant. If we want to include more general perturbations properly we have to balance the variation in the radial perturbation with perturbation components in other directions in order to achieve zero divergence. To guarantee this we can write both the original field and the perturbation in terms of their vector potentials.

Any magnetic field can be derived from a vector potential $\mathbf{A}$:

$$\begin{aligned}\mathbf{A} &= A_\theta \nabla\theta + A_\phi \nabla\phi \\ \mathbf{B} &= \nabla \times \mathbf{A} \\ &= \frac{\partial A_\theta}{\partial\psi}\nabla\psi\times\nabla\theta + \frac{\partial A_\phi}{\partial\psi}\nabla\psi\times\nabla\phi + (\frac{\partial A_\phi}{\partial\theta} - \frac{\partial A_\theta}{\partial\phi})\nabla\theta\times\nabla\phi\end{aligned}$$

The ψ component of the vector potential can be set to zero without losing any freedom in the magnetic field.

For the unperturbed field ($\mathbf{B_0}$) of the previous section, ψ is a flux surface coordinate. This gives $B_0^\psi = 0$, which sets the condition on the unperturbed vector potential $\mathbf{A_0}$:

$$\frac{\partial A_{0\,\phi}}{\partial\theta} - \frac{\partial A_{0\,\theta}}{\partial\phi} = 0 \tag{2.14}$$

The choice of particular straight field-line coordinates for the unperturbed field fixes $\partial A_\theta/\partial\psi = 1$ and $\partial A_\phi/\partial\psi = -\iota(\psi)$.

For the perturbing vector potential ($\mathbf{A_1}$) any functions $A_{1\,\theta}(\psi,\theta,\phi)$ and $A_{1\,\phi}(\psi,\theta,\phi)$ are possible. It is convenient to write the perturbing vector potential in terms of the rotating coordinates for the particular rational surface we are interested in, $a = \theta - (m/l)\phi$ and $\zeta = \phi$ and to decompose it into Fourier harmonics in ϕ and θ:

$$\mathbf{A_1} = \sum_{l,m}[A_{a\,l,m}(\psi)\nabla(\theta - \frac{m_R}{l_R}\phi) + A_{\zeta\,l,m}(\psi)\nabla\phi]e^{(il\theta - im\phi)} \tag{2.15}$$

For the most general perturbation we expect all harmonics in m and l to be present. The field-line invariant close to the resonant rational surface ψ_R is given by Cary & Kotschenreuther (1985) as:

$$\begin{aligned}\chi &= \frac{1}{2}\iota'_R(\psi-\psi_R)^2 \\ &\quad - \sum_{k=-\infty}^{\infty} A_{\zeta\,kl_R,km_R}(\psi)e^{(ikl_R\theta - ikm_R\phi)} \\ &\quad - \iota'_R(\psi-\psi_R)\sum_{k=-\infty}^{\infty} A_{a\,kl_R,km_R}(\psi)e^{(ikl_R\theta - ikm_R\phi)} \\ &\quad - \iota'_R(\psi-\psi_R)\sum_{l,m}{}' \frac{A_{\zeta\,l,m} + (m_R/l_R - m/l)}{m_R/l_R - m/l}e^{(il\theta - im\phi)}\end{aligned} \tag{2.16}$$

The resonant components of A_ζ dominate the effect of the perturbation on the shape of the perturbed flux surface. (This component of $\mathbf{A_1}$ gives the radial field perturbation). Close to the rational surface the $\iota'_R(\psi-\psi_R)$ factor reduces the effect of resonant A_a and nonresonant components of the perturbation. Far from ψ_R the nonperturbed part $\frac{1}{2}\iota'_R(\psi-\psi_R)^2$ dominates. The other terms make only a small contribution to χ for any value of ψ. Calculation of this invariant assumes that near ψ_R the rotational transform can be linearised to $\iota(\psi) = m_R/l_R + \iota'_R(\psi-\psi_R)$

2.5 A linear theory of magnetic islands

The vacuum field of a stellarator can be optimised to minimise perturbations that resonate with low order rational surfaces present in the device. However, resonant perturbations can develop from currents within a finite pressure plasma equilibrium. At low pressure, the contribution of the current to the magnetic field is small and the plasma current is well approximated by a linear estimate using a given pressure profile with the vacuum magnetic field. Following the method used in Cary & Kotschenreuther (1985), we start from a vacuum field $\mathbf{B_0}$. We then add a small pressure perturbation p and calculate the linear variation of the current, $\mathbf{J}$. The vacuum field should have nested flux surfaces so that it can be written in straight field-line coordinates (ψ, θ, ϕ) as $\mathbf{B_0} = \nabla\psi \times \nabla\theta + \iota(\psi)\nabla\psi \times \nabla\phi$. The vacuum field can also be written in magnetic coordinates as $\mathbf{B_0} = (2\pi/I)\nabla\phi$.

The perturbed current is set to maintain pressure balance:

$$\mathbf{J} \times \mathbf{B_0} = \nabla p \tag{2.17}$$

This equation is solvable only if the introduced pressure is constant on flux surfaces of the vacuum field i.e. $p = p(\psi)$ giving a simple expression for the pressure gradient $\nabla p = p'(\psi)\,\nabla\psi$. The perpendicular part of Eqn. 2.17 is :

$$\mathbf{J}_\perp = \mathbf{B_0} \times \nabla p / B_0^2 \tag{2.18}$$

Writing this in magnetic coordinates and using $\mathcal{J} = (\nabla\psi \times \nabla\theta \cdot \nabla\phi)^{-1}$, we get:

$$\mathbf{J}_\perp = p'(\psi)\mathcal{J}(\psi, \theta, \phi)\nabla\phi \times \nabla\psi \tag{2.19}$$

The Jacobian, $\mathcal{J}$, is the inverse of the square of the magnetic field strength. Where field strength is low more current is needed for $\mathbf{J}\times\mathbf{B}$ to balance the pressure gradient.

Plasma currents parallel to the magnetic field have no effect on the force balance equation and are, instead, constrained by the fact that current must be divergence free ie. $\nabla \cdot \mathbf{J}_\parallel = -\nabla \cdot \mathbf{J}_\perp$. This parallel current is called the Pfirsch-Schlüter current and can be written:

$$\mathbf{J}_\parallel = Q\mathbf{B} = Q(\psi, \theta, \phi)[\nabla\psi \times \nabla\theta + \iota(\psi)\nabla\phi \times \nabla\psi] \tag{2.20}$$

The plasma current and Jacobian can be separated into their Fourier harmonics in the magnetic coordinates θ and ϕ.

$$\begin{aligned} \mathcal{J}(\psi, \theta, \phi) &= \sum_{l,m} \mathcal{J}_{lm}(\psi) e^{i(l\theta - m\phi)} \\ \mathbf{J}(\psi, \theta, \phi) &= \sum_{l,m} (\mathbf{J}_{\perp lm} + \mathbf{J}_{\parallel lm}) e^{i(l\theta - m\phi)} \end{aligned}$$

where

$$\begin{aligned} \mathbf{J}_{\perp lm} &= p'(\psi)\mathcal{J}_{lm}(\psi)\nabla\phi \times \nabla\psi \\ \mathbf{J}_{\parallel lm} &= Q_{lm}(\psi)(\nabla\psi \times \nabla\theta + \iota(\psi)\nabla\phi \times \nabla\psi) \end{aligned}$$

The divergence free conditions, combined with currents being restricted to flowing along flux surfaces, ensures that the current component given by $(\mathbf{J}_{\perp lm} + \mathbf{J}_{\parallel lm})e^{i(l\theta - m\phi)}$ must flow in the direction it does not vary, ie. $\mathbf{J}_{lm} = J_{lm}\nabla\psi \times \nabla(\theta - m\phi/l)$. This gives the Fourier components Q_{lm}:

$$[l\,\iota(\psi) - m]Q_{lm}(\psi) = -lp'(\psi)\mathcal{J}_{lm}. \tag{2.21}$$

As the rotational transform approaches m/l the m, l current component is nearly parallel to the field lines. Therefore a very large current near a rational surface is produced to counter a resonant variation in field strength. Ideal MHD equilibria allow arbitrary parallel currents. To maintain current conservation the arbitrary currents must either be constant over a magnetic surface, or constant over a closed field line on a rational surface. This is reflected in Eqn. 2.21 leaving the $Q_{00}(\psi)$ component of the parallel current undetermined and also allowing an arbitrary delta current $Q_{ml}(\psi_R)$ on the rational surface with $\iota(\psi_R) = m/l$. In reality, if they are not driven, these currents will be damped out by small resistivity. For stellarator equilibrium the assumption that there is no net longitudinal current on a magnetic surface determines the constant term in the parallel current. In this case we should set $Q_{00}(\psi) = 0$ and avoid singular currents at rational surfaces. However, because of the condition of frozen flux, in an ideal MHD equilibrium the topology will not change and singular (delta) currents at rational surfaces will be driven to prevent the formation of islands. Any amount of added resistivity allows a change of topology and prevents these currents from remaining at equilibrium. (But they may occur as transients to resist the drift of plasma across flux surfaces.)

In later sections, delta currents at rational surfaces have been used to approximate the net effect of local-island currents on the perturbed magnetic field.

The total linearised current is (Cary & Kotschenreuther (1985))

$$\begin{aligned}\mathbf{J}_1 \;=\; & \sum_{l,m\neq(0,0)} \{\hat{Q}_{lm}\delta(\psi - \psi_{lm}) - \frac{p'(\psi)\mathcal{J}_{lm}(\psi)}{\iota(\psi) - m/l}\}e^{il\theta - im\phi}\nabla\psi \times \nabla(\theta - m\phi/l) \\ & + p'(\psi)\mathcal{J}_{00}(\psi)\nabla\theta \times \nabla\psi \end{aligned} \tag{2.22}$$

This linear treatment can be made more accurate if a better approximation to the equilibrium field than the vacuum field is known (Hegna & Bhattacharjee (1989), Reiman & Boozer (1984)). The above calculation relies on the magnetic field having nested flux surfaces so that the flux coordinate treatment can be used. In general, the equilibrium field, and possibly the vacuum field, will contain islands at rational surfaces. A nearby field without islands can be used to generate a good approximation to currents away from the island from Eqn. 2.22, but local currents near the island will need to be treated separately.

2.6 Magnetic field from plasma currents

The plasma currents calculated in the previous section will alter the equilibrium magnetic field. In order to determine the island growth due to the plasma currents,

the contribution of these currents to the harmonics of the vector potential, $\mathbf{A_1} = \sum_{l,m}[A_{a\,l,m}(\psi)\nabla(\theta - \iota_R\phi) + A_{\zeta\,l,m}(\psi)\nabla\phi]e^{(il\theta - im\phi)}$, need to be calculated. The vector potential is related to the plasma currents by Ampére's law, $\nabla \times (\nabla \times \mathbf{A_1}) = \mathbf{J_1}$. The plasma current can be divided into its harmonic components (as was done in the previous section) to give:

$$\mathbf{J_1} = J_{00}(\psi)\,\nabla\phi \times \nabla\psi + \sum_{l,m\neq 0,0} Q_{lm}\nabla\psi \times \nabla(\theta - m\phi/l)e^{(il\theta - im\phi)} \tag{2.23}$$

Even though $\nabla \times (\nabla \times \mathbf{A_1})$ is a linear operator, because of the nature of the coordinate system, and the need to change from covariant to contravariant representation, a single harmonic of $\mathbf{J_1}$ can contribute to every harmonic of $\mathbf{A_1}$. However, if the flux surfaces are nearly circular and the aspect ratio is small, an approximation using cylindrical coordinates can be used for the operator $\nabla \times (\nabla \times \mathbf{A})$. This separates the harmonic equations so that Q_{lm} contributes only to $\mathbf{A}_{1lm}$. Using cylindrical coordinates, with $R_0\phi \to z$, $\theta \to \theta$ and $\psi \to r^2B/2$, Ampére's law for each harmonic component reduces to (Cary & Kotschenreuther (1985)):

$$\frac{\partial A_{a\,l,m}}{\partial r} = \frac{mr^2/lR_0}{1 + (mr/lR_0)^2}\frac{\partial A_{\zeta\,l,m}}{\partial r} \tag{2.24}$$

$$\frac{\partial}{\partial r}\frac{r/R_0}{1 + (mr/lR_0)^2}\frac{\partial A_{\zeta\,l,m}}{\partial r} - \frac{l^2}{rR_0}A_{\zeta\,l,m} = -Q_{l,m} \tag{2.25}$$

The Green's function for solving equation 2.25 for $A_{\zeta\,l,m}$ is:

$$G(r,r') = -\frac{m^2 r r'}{l^2 R_0}\, I_l'(\frac{mr_<}{R_0})\, K_l'(\frac{mr_>}{R_0}) \ . \tag{2.26}$$

Here I_l' and K_l' are the derivatives of the modified Bessel functions of order l, with $r_<$ the minimum of (r,r') and $r_>$ being the maximum of (r,r'). This Green's function gives $A_{\zeta\,l,m}$ at r from a unit sheet current of appropriate harmonic at r', $Q = \exp(il\theta - im\phi)\delta(r - r')$. (It also gives the contribution to $A_{\zeta\,l,m}$ at r' from a sheet current at r since it is symmetric to reversing the variables.)

The shape of the Green's function is shown in Fig. 2.6 for $l = 5$. It is peaked at $r = r'$ so the main contribution to $A_{\zeta\,l,m}$ (and thus the island width) comes from currents near the rational surface.

We can use the Green's function of Eqn. 2.26 to determine the resonant perturbations caused by the plasma currents given in Sect. 2.5. The resonant current predicted by the linear theory is of the form $Q_{l,m}(r) = (dp/d\psi\, \mathcal{J}_{l,m})/(\,\iota'(r - r_{l,m}))$ where we can linearise ι in the vicinity of the rational surface. The corresponding resonant component of the vector potential is:

$$A_{\zeta\,l,m}(r) = \int_0^\infty G(r,r')\frac{dp(r')}{d\psi}\frac{\mathcal{J}_{l,m}}{\iota'(r' - r_{l,m})}\,dr' \ . \tag{2.27}$$

Because the large currents near a rational surface run in opposite directions on either side of the surface, the effect of these currents on the field perturbation at the

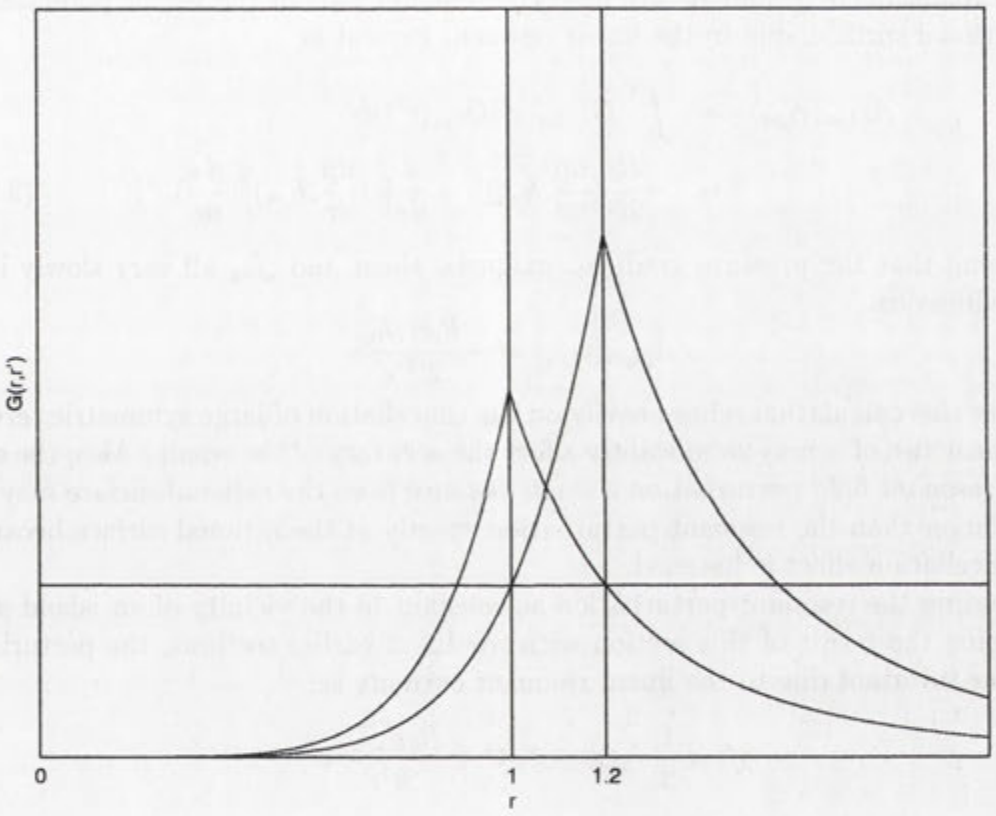

Figure 2.6: Green's functions for sheet currents at $r' = 1$ and $r' = 1.2$ demonstrating symmetry of the Green's function.

rational surface largely cancel each other. The Green's function is not exactly symmetric; it is higher for $r = r' + \epsilon$ than for $r = r' - \epsilon$. Therefore the contribution of the currents on the edge side of the rational surface out-compete the contribution from the currents on the magnetic-axis side of the rational surface. The Green's function becomes less symmetric further from r', which allows currents further away from the rational surface to make a much larger contribution to the field perturbation at the surface than one might have expected from the highly peaked nature of the current and Green's function. This gives the contribution of linear resonant currents to island size a global nature. According to Cary & Kotschenreuther (1985), if asymptotic expansions of I' and K' are used the resonant part of the vector potential at the rational surface, due to the linear resonant current is:

$$\begin{aligned} A_{\zeta\, l,m}(r_{l,m}) &= \int_0^\infty G(r_{lm}, r') Q_{l,m}(r')\, dr' \\ &= -\frac{R_0}{2l^2}\left(\frac{dp}{dr}\mathcal{J}_{l,m}\right)^{-1} \cdot \frac{d}{dr}\left[r\left(\frac{dp}{dr}\mathcal{J}_{l,m}\right)^2 \left(\frac{d\,\iota}{dr}\right)^{-1}\right] \end{aligned} \tag{2.28}$$

Assuming that the pressure gradient, magnetic shear and $\mathcal{J}_{lm}$ all vary slowly in r this reduces to:

$$A_{\zeta\, l,m}(r_{l,m}) = -\frac{R_0 p' \mathcal{J}_{lm}}{2l^2\, \iota'}$$

Because this calculation relies heavily on the cancellation of large symmetric terms, non-linearities of ι may significantly affect the accuracy of the result. Also, the size of the resonant field perturbation a small distance from the rational surface may be much larger than the resonant perturbation exactly at the rational surface because the cancellation effect is lessened.

Treating the resonant perturbation as constant in the vicinity of an island and combining the result of this section with results of earlier sections, the perturbed field-line invariant due to the linear resonant currents is:

$$\chi^* = \frac{1}{2}\,\iota'_R(\psi - \psi_R)^2 + \frac{R_0 p' \mathcal{J}_{lm}}{2l^2 \iota'} e^{il\alpha}$$

which gives islands, of width

$$\delta\iota = 2\sqrt{\frac{R_0 p' \mathcal{J}_{lm}}{2l^2}},$$

centred at places of large $\mathcal{J}_{lm}$, i.e. minimum magnetic field strength. The magnetic surfaces of the H-1NF Heliac that are studied in this thesis are bean shaped rather than circular. If the above analysis was carried out with the exact Green's function for these surfaces the resulting island caused by the linear resonant current would have a different width but essentially the same scaling with pressure gradient, magnetic shear, minor radius and the resonant component of the Jacobian. The main effect of non-circular flux surfaces would be to allow contributions to the island size from non-resonant currents. Even if the coupling between the non-resonant currents and the island is not strong, the contribution to the island width can be substantial compared to the resonant current contribution since the non-resonant

currents on either side of the island would be reinforcing each other rather than cancelling. Determination of the total contribution of the non-resonant currents to the island width would be very involved but I would still expect a linear scaling of the perturbation to the vector potential with pressure gradient.

2.7 Local currents around islands

The presence of an island changes the local pressure and currents. Disregarding pressure sources, because of small island size, the pressure within the island will be flat and therefore there will be no pressure-driven plasma current. Near the island the pressure will be constant along the new field-line invariant, χ, defined earlier.

The currents near the island can be determined from $\mathbf{J} \times \mathbf{B} = \nabla p$ using the new flux surfaces. The perpendicular current must be higher in regions where the field strength is low, as was true of the linear plasma currents. The resonant component of the perpendicular current around an island will be:

$$J_{\perp mn}(\chi) = \mathcal{J}^*_{mn} p'(\chi) \nabla\chi \approx \mathcal{J}^*_{mn} p'(\psi) \nabla\psi$$

where $\mathcal{J}^*_{mn}(\chi)$ is the resonant variation in the Jacobian (approximately equal to the inverse of the field strength) over the perturbed flux surface. The resonant perturbation produces a significant distortion in the shape of the flux surfaces near an island, but only a very small effect on the magnetic field at any one point. Thus the difference between $\mathcal{J}^*_{mn}(\chi)$ and the resonant component of the vacuum Jacobian, $\mathcal{J}_{mn}(\psi)$, is mostly due to the perturbation of the flux surface. Assuming that the main variation of the vacuum Jacobian across flux surface is due to the $\mathcal{J}'_{00}$ component, the new Jacobian is approximately given by:

$$\mathcal{J}^*_{mn}(\chi) \approx \mathcal{J}_{mn} + \mathcal{J}'_{00} \Delta\psi,$$

where $\Delta\psi$ is the variation in ψ of the new flux surface defined by constant χ. The resonant Pfirsch-Schlüter current needed to keep charge conservation is, similar to the linear resonant Pfirsch-Schlüter current, $Q_{mn} \approx \mathcal{J}^*_{mn}(\chi) p'(\psi) / (< \iota(\psi) > - m/n)$. Near the island separatrix the local rotational transform varies significantly on the new flux surface, depending on how close it is to an X-point. The appropriate value of $< \iota(\psi) >$ to use in the calculation of parallel current is one at a point far from the X-point, where ι is most different from the resonant value. The resonant plasma current has two parts. The first is $\mathcal{J}_{mn} p'(\psi) / (< \iota(\psi) > - m/n)$ which is approximately the linear resonant current but with the singularity removed by the presence of the island (since $< \iota(\psi) >$ is always a finite distance from the resonant rotational transform). As we saw in the previous section, removing the small singular section (so long as it is done symmetrically) will not significantly change the field perturbation at the rational surface caused by this current. The other part of the resonant plasma current near the island is due to $\mathcal{J}'_{00} \Delta\psi$. This is an antisymmetric variation in field strength and so produces a symmetric current. The symmetric current has a greater effect on the resonant field perturbation than

an antisymmetric current of the same size. This part of the parallel current decays away from the island only slightly more quickly than the linear current but, because it is symmetric, its effect is much more localised and the effect on the field can be determined from an equivalent delta current on the rational surface. Whether the island induced currents reinforce or act against the linear perturbation will depend on the sign of $\mathcal{J}'_{00}$, i.e. whether the magnetic field has a hill or well.

This local resonant current is determined more rigorously and accurately in Cary & Kotschenreuther (1985) and in Hegna & Bhattacharjee (1989). In Cary & Kotschenreuther (1985) the pressure gradient just outside the island is determined by the plasma flow needed to drive currents against resistivity. In the limit away from the island the pressure gradient matches to the pressure gradient without a resonant perturbation. Cary & Kotschenreuther (1985) found that the total local island current can be approximated by the delta current:

$$\hat{Q}_{lm} \approx -\frac{\mathcal{J}'_{00} p'}{4\, \iota'^2} \mathrm{sign}(\chi_c)\, \delta\iota$$

where the direction of the current depends on the phase of the resonant perturbation. If $\mathcal{J}'_{00} < 0$, indicating a magnetic well, then this current will produce a resonant perturbation that reduces the island size. In the presence of a magnetic hill the local currents will act to increase the size of the island. This current will produce a resonant perturbation at the rational surface which would in turn produce an island with width:

$$\delta\iota = \sqrt{\frac{R_0 \mathcal{J}'_{00} p'\, \delta\iota}{2l\, \iota'}}$$

This can be solved for $\delta\iota$ to get a self consistent island width (if the local current alone is responsible for the island width).

Hegna & Bhattacharjee (1989) use a near-equilibrium magnetic field rather than the vacuum field to extend the results to higher beta and found that the local resonant currents around an island are proportional to the resistive Mercier criterion, D_R, rather than just the magnetic well. They find that the total local island current can be approximated by the delta current:

$$\hat{Q}_{lm} = \frac{D_R B_0 r^2}{2R_0}\, \delta\iota$$

which is equivalent to the result of Cary & Kotschenreuther (1985) at low beta.

By combining the field perturbations produced by the local island current with the field perturbation given by the linear, global, resonant currents and the field perturbations from external currents we can determine the expected island width of the equilibrium field (Bhattacharjee *et al.* (1995)).

$$|\delta\iota| = G/2 + \sqrt{(G/2)^2 \pm (C + \delta\iota_v^2)} \tag{2.29}$$

with the + giving an island in phase with the vacuum island and the − giving a solution 180 degrees out of phase with the vacuum island. Here

$$G = \frac{D_R}{l} \left| r \frac{d\,\iota}{dr} \right|$$

is due to the local island current, and $\delta\iota_v$ is the vacuum island size due to external currents. C can be calculated using a circular flux surface assumption giving

$$C = -\frac{2}{B_0^2}\frac{dp}{dr}\frac{R_0^2}{rl^2}\left|\frac{\mathcal{J}_{lm}}{\mathcal{J}_{00}}\right| \quad .$$

Taking into account non-circular flux-surfaces, and including effects of non-resonant linear currents will give a different value of C but preserve its linear relationship with pressure gradient.

The characteristic growth patterns of islands predicted by this equation are shown in Fig. 2.7. When linear currents dominate ($G = 0$) the island will grow with increasing plasma pressure if the linear currents reinforce the vacuum island. If the linear currents oppose the vacuum perturbation the island will shrink to nothing and then an island of opposite phase will grow. Under this condition major islands can be eliminated from the magnetic field of a reactor at operating pressure by careful choice of perturbation currents that control the size and phase of the vacuum islands. The pressure range for which the island is significantly smaller than the vacuum island is narrow so dynamic control of the perturbation currents would be neccessary.

If the non-linear currents are stabilising ($G < 0$) the islands grow less rapidly as pressure increases than they would with $G = 0$. The critical pressure at which the island switches phase is not altered. For sufficiently negative G, these stabilising non-linear currents dominate and the islands shrink as plasma pressure increases. This makes the control of islands in a reactor much less dependent on operating pressure.

For $G > 0$ non-linear currents destabilise the island and will increase the size of any island compared with the $G = 0$ case.

There are two situations where the non-linear currents will dominate. The first is near the critical pressure where the vacuum perturbation and the perturbation from the linear currents almost cancel (ie. $C \approx -\delta\iota_v^2$)). The second is at high pressures where the non-linear currents dominate over the vacuum perturbation and linear currents. This allows a stable equilibrium with an island of opposite phase to that predicted by the linear currents and somewhat smaller. This equilibrium will not be found by smooth pressure increase from vacuum. It may be accessible physically by rapid pressure transitions or by varying the external currents. Which equilibrium solution is found for this region by a computer simulation will depend on initial conditions and the relaxation method.

For sufficiently large D_R the two regions where G dominates may overlap (eg the lower right graph in Fig. 2.7). In this case there is always a stable equilibrium solution with the vacuum island phase so it is not neccessary for the island to change phase as the pressure increases. A smooth increase in pressure will cause the vacuum island to grow but never to swap phase, even though the opposite phase island would be larger. The alternative solution may be accessible with a different path to equilibrium.

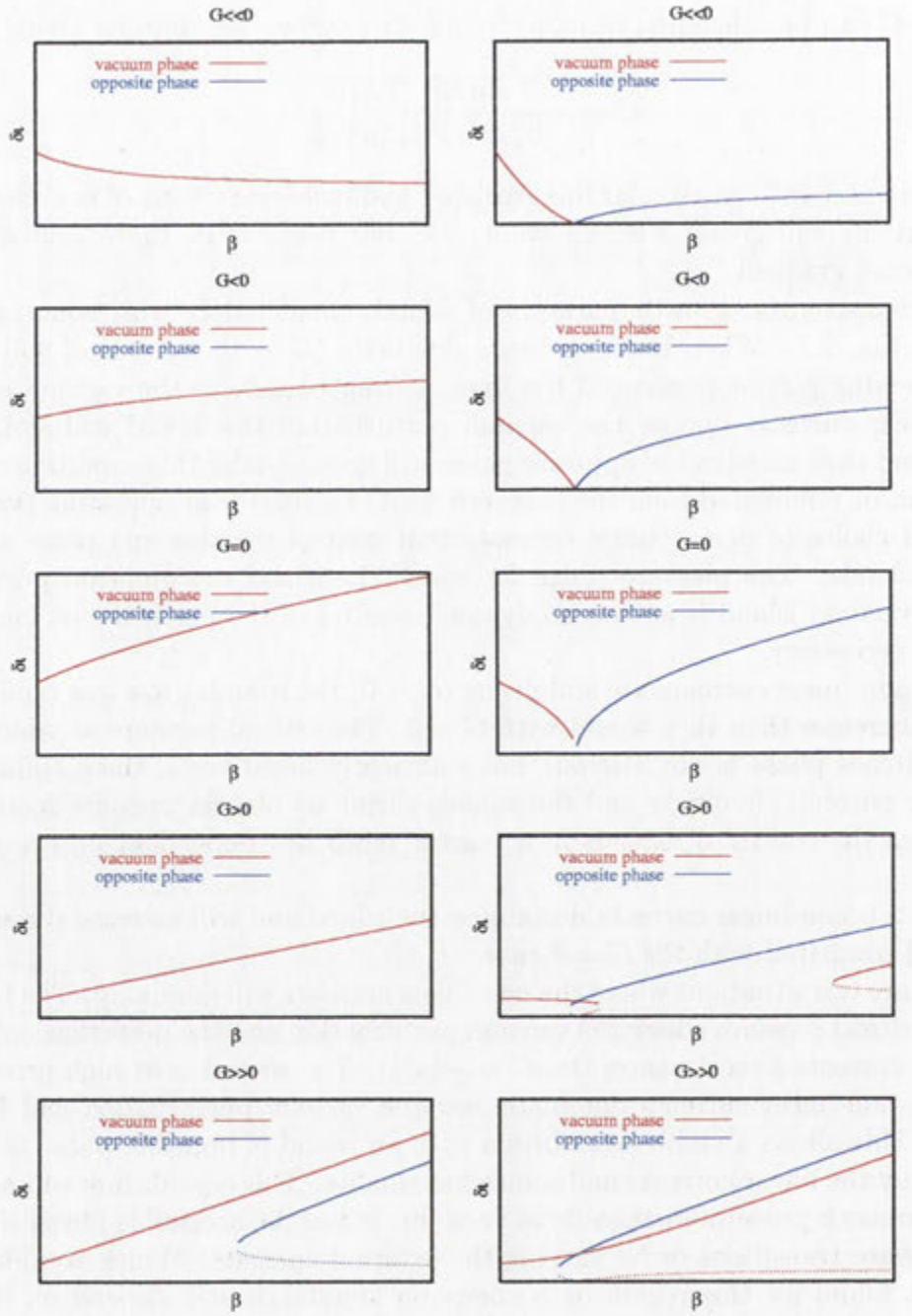

Figure 2.7: Growth patterns for islands depend on whether the vacuum island is reinforced (plots to the left) or counteracted (plots to the right) by the linear currents and on how stabilising or destabilising the non-linear currents are. It is assumed that G and C of Eqn. 2.29 are directly proportional to the plasma pressure. Red lines indicate an island of the same phase as the vacuum island while blue lines indicate islands of opposite phase. Dotted lines show unstable solutions.

CHAPTER 3

Computing MHD equilibrium fields of stellarators

In order to optimise the stability and transport properties of stellarator plasmas, the equilibrium field and pressure distribution is needed. The equilibrium equations of magneto-static equilibrium can be derived from a simple fluid model of the plasma (MHD). MHD also gives information about possible routes to equilibrium, and constraints on the equilibrium to select the appropriate solution to the magneto-static equations for a given machine's vacuum field and plasma sources. Analytic solution of the equilibrium is generally not possible for real 3D stellarators so a number of computer codes have been developed. While these all solve the magneto-static equations they differ both in the techniques to relax toward equilibrium, the types of coordinate grid used, and in the types of constraints they impose to select an appropriate equilibrium. I will give a summary of the approach of some of these codes and a detailed description of one, HINT, which I have used to find equilibrium fields of the H-1NF heliac. HINT is one of the few codes capable of including the field topology changes needed to model magnetic islands.

3.1 MHD equilibrium equations

Single fluid ideal magneto-hydrodynamics (MHD) treats the plasma as an infinitely conducting, inviscid, neutral fluid. It can be derived from moments of the kinetic equations of a plasma in the limit of high magnetisation, low collisionality and with an assumption of local thermal equilibrium (Hazeltine & Waelbroeck (1998)). The equations describing the MHD fluid are:

$$\frac{\partial \rho}{\partial t} + \mathbf{v} \cdot \nabla \rho + \rho \nabla \cdot \mathbf{v} = 0 \tag{3.1}$$

$$\rho \frac{\partial \mathbf{v}}{\partial t} + \rho \mathbf{v} \cdot \nabla \mathbf{v} + \nabla p - \mathbf{J} \times \mathbf{B} = 0 \tag{3.2}$$

$$\frac{\partial p}{\partial t} + \mathbf{v} \cdot \nabla p + \gamma p \nabla \cdot \mathbf{v} = 0 \tag{3.3}$$

$$\mathbf{E} + \mathbf{v} \times \mathbf{B} = \mathbf{0} \tag{3.4}$$

$$\nabla \times \mathbf{B} = \mu_0 \mathbf{J} \tag{3.5}$$

$$\nabla \times \mathbf{E} + \frac{\partial \mathbf{B}}{\partial t} = 0 \tag{3.6}$$

Equation 3.1 provides mass conservation for the fluid and may have a source term added. Equation 3.2 describes plasma mass flow resulting from a competition between the pressure gradient and the $\mathbf{J} \times \mathbf{B}$ force. Equation 3.3 allows for expansion or compression of the fluid. The value of γ used in it depends on assumptions about the equation of state ($p\rho^{\gamma}$ = constant). The assumption of local thermal equilibrium, which implies no heat flow, gives adiabatic expansion with $\gamma = 5/3$. Equation 3.4 is a consequence of infinite conductivity and requires the electric field in the frame moving with the fluid to be zero. Equations 3.5 and 3.6 are the relevant Maxwell equations for relatively slow time scales (ignoring displacement current). The charge conservation restriction on current flow is implicitly satisfied by defining it as the curl of the magnetic field.

An important consequence of Eqn. 3.4 is 'frozen flux'. There can be no change in the magnetic flux crossing any surface which flows with the plasma. Flux tubes are, therefore, locked to the plasma they initially contained. This flux conservation prevents the magnetic field from changing topology within the plasma. The development of magnetic islands is not possible within an ideal MHD plasma, neither can the rotational transform change. If the initial state of the magnetic field within the plasma consists entirely of nested flux surfaces then the subsequent evolution of the magnetic field cannot produce islands or stochastic field regions. Even if the initial field contains a small island, the island cannot grow significantly without a corresponding decrease in the plasma density inside the island, which could not be sustained.

Another consequence of 'frozen flux' is the Alfvén wave speed. Shear Alfén waves are the transverse vibrations of a flux tube along with its attached plasma. The magnetic field has an associated tension $T = B^2/2\mu_0$ (Hazeltine & Waelbroeck (1998)) while the attached plasma gives it an effective mass density, ρ. Thus a flux tube can vibrate like a string with the Alfvén wave speed $v_A = \sqrt{B^2/(\mu_0 \rho)}$.

Flux conservation is maintained in ideal MHD by the growth of currents parallel to the magnetic field. As the plasma is pushed across the magnetic field a current develops to oppose this motion. Since there is no resistivity to oppose the current, the current grows instantly to be sufficient to prevent any plasma crossing the magnetic field. These parallel currents make no contribution to force balance and satisfy charge conservation so long as they are constant along a field line. Any surface can maintain an arbitrary constant parallel current which prevents changes to the rotational transform. At rational surfaces the field lines form closed loops, each of which can have an arbitrary parallel current. The development of magnetic islands is prevented by the formation of singular currents, parallel to the magnetic field, at rational surfaces.

There is no equilibrium, driving-force for these parallel currents. Over long time-scales we would expect even minute resistivity to damp the parallel currents and allow the field topology to change. In this case it is worthwhile introducing some resistance to current flow, which changes Eqn. 3.4 to $\mathbf{E} + \mathbf{v} \times \mathbf{B} = \eta \mathbf{J}$. The resisivity, η, adds an energy dissipating term to the energy conserving system of ideal

MHD equations. Energy is provided to drive the currents against the resistivity by a flow of plasma across flux surfaces, in the direction of the pressure gradient. This gives a diffusive loss of pressure and density. Consequently in a long time scale situation, or to have a non-trivial steady state, a pressure and density source is usually included with resistive MHD. Resistivity arises out of collisions which were ignored in the derivation of MHD. Other effects are of similar order but are ignored because their consequences are less severe.

This thesis looks at equilibrium solutions to the MHD equations. The transient form will be important only for the restrictions it gives on the final equilibrium, assuming particular paths to equilibrium.

The ideal MHD equations at steady state reduce to:

$$\mathbf{v} \cdot \nabla \rho + \rho \nabla \cdot \mathbf{v} = 0 \tag{3.7}$$

$$\rho \mathbf{v} \cdot \nabla \mathbf{v} + \nabla p - \mathbf{J} \times \mathbf{B} = 0 \tag{3.8}$$

$$\mathbf{v} \cdot \nabla p + \gamma p \nabla \cdot \mathbf{v} = 0 \tag{3.9}$$

$$\nabla \times \mathbf{B} = \mu_0 \mathbf{J} \tag{3.10}$$

$$\nabla \times (\mathbf{v} \times \mathbf{B}) = 0 \tag{3.11}$$

However, as discussed above, a plasma evolved under ideal MHD in a closed system will not approach steady state because there is no energy dissipation. The type of energy dissipation that is assumed in reaching steady state will effect the equilibrium conditions.

A viscosity, μ, can be added to the ideal MHD equations to dissipate energy without losing the 'frozen flux' characteristic of ideal MHD. To include viscosity, Eqn. 3.2 becomes $\rho \partial \mathbf{v}/\partial t + \rho \mathbf{v} \cdot \nabla \mathbf{v} + \nabla p - \mathbf{J} \times \mathbf{B} - \mu \nabla^2 \mathbf{v} = 0$. With this modification to the MHD equation set the plasma will evolve to a steady state that has $\mathbf{v} = 0$ everywhere (Kruskal & Kulsrud (1958)). This static steady state will satisfy the magneto-static equations:

$$\nabla p - \mathbf{J} \times \mathbf{B} = 0 \tag{3.12}$$

$$\mu_0 \mathbf{J} = \nabla \times \mathbf{B} \tag{3.13}$$

$$\nabla \cdot \mathbf{B} = 0 \tag{3.14}$$

The mass conservation and 'frozen flux' conditions of ideal MHD will still apply to a plasma evolving with viscosity. If the initial magnetic field has nested toroidal flux surfaces labelled by toroidal flux ψ with rotational transform of $\iota(\psi)$ and contained mass of $M(\psi) = \int_{<\psi} d\tau p^{1/\gamma}$ then the equilibrium field achieved by relaxing the plasma will conserve $\iota(\psi)$ and $M(\psi)$ and satisfy the magneto-static equations. These constraints, with a boundary condition to set the contribution of external currents, are sufficient to specify a unique equilibrium solution (Kruskal & Kulsrud (1958)). The magnetic field topology of the initial and final states will match exactly under this relaxation scheme, islands can neither develop nor grow and the rotational transform is also fixed. Note that γ, which controls the plasma compressibility, effects only which equilibrium solutions match to which initial mass distributions, not whether a given field and pressure distribution are at equilibrium. It is often

more convenient to specify the final pressure function, $p(\psi)$, explicitly, which is equivalent to setting $\gamma = 0$.

As mentioned earlier, adding resistivity also removes energy from the ideal MHD equations enabling them to relax to equilibrium, but one with a different set of constraints. Equilbrium MHD equations including resistivity require a plasma source term to balance the diffusive losses which drive the currents necessary for pressure balance. Resistive MHD has the advantage of preventing singular currents and allowing changes to flux surface topology and rotational transform profile so it gives a more realistic plasma equilibrium. Resistivity can reduce kinetic energy contained in plasma velocity as well as electric currents. The steady state of this system will be nearly static and, to zeroth approximation in the diffusion velocity, satisfies the magneto-static equations, but with the minimum longitudinal current necessary to satisfy charge conservation. This condition has been expressed as a restriction on the net toroidal current: $\int_{<\psi} d\tau\, J \cdot \nabla\phi = 0$ (Kruskal & Kulsrud (1958)), and as zero field-line-averaged parallel current for any closed field line $<\eta \mathbf{J} \cdot \mathbf{B}>= 0$ (Park *et al.* (1986)). The constraint on longitudinal current replaces rotational transform conservation. The equilibrium pressure function is specified by the choice of source term and resistivity. It is also possible to set the pressure function explicitly and assume an appropriate source term. This specification of pressure profile replaces the constraint of mass conservation within flux surfaces. The velocity of the resistive equilibrium is not zero despite the magnetic field satisfying magneto-static equilibrium. Plasma velocity perpendicular to the magnetic field is determined by the need to drive plasma currents against resistivity, and is directly proportional to resistivity. Parallel plasma velocity has an arbitrary component not effected by resistivity or effecting the equilibrium field.

All the MHD equilibrium codes I describe here find magnetic fields tending to solutions of Eqn. 3.12. They differ in the process of relaxation, the coordinate system used, and in the types of constraints on pressure and longitudinal current that are imposed on that equilibrium.

3.2 Energy minimisation and variational principles

The magneto-static equations can be reached by minimising the potential energy:

$$W = \int d^3x \, (B^2/2 + p/(\gamma - 1)) \tag{3.15}$$

To match an equilibrium reached by viscous damping of ideal MHD, minimisation is subject to constraints on mass conservation and magnetic flux conservation (Kruskal & Kulsrud (1958)). An equilibrium that minimises W must have $\mathbf{F} = (\nabla \times \mathbf{B}) \times \mathbf{B} - \nabla p = 0$. This local plasma force can be used to work out a displacement, $\xi = a\mathbf{F}\delta t$, that reduces the combined potential energy of the plasma and magnetic field. The displacement of the plasma drags the field and density with it because of the mass conservation and 'frozen flux' constraints, $\delta\rho = -\nabla \cdot (\rho\xi)$ and $\delta\mathbf{B} = \nabla \times (\xi \times \mathbf{B})$ (Chodura & Schlüter (1981)).

While a displacement of this form will converge to the desired solution, modifying the dependence of the displacement on $\mathbf{F}$ can improve convergence. The conjugate gradient method proceeds by discrete steps with step sizes modified for optimal performance and with $\mathbf{F}$ at previous steps also influencing the displacement at this step.

$$\xi_{n+1} = \xi_n + \mathbf{v}_n(t_{n+1} - t_n)$$

where

$$\mathbf{v}_n = \mathbf{F}_n + b(<F_n^2> / <F_{n-1}^2>)\mathbf{v}_{n-1}.$$

Chodura and Schülter developed a 3D MHD equilibrium code using this method evaluated in a cylindrical coordinate system over a toroidal domain with fixed rectangular cross-section. The simulation space is bounded by a conducting wall which keeps the normal component of the magnetic field boundary constant as the simulation proceeds. The plasma extends to the wall with no vacuum region and, in the low density limit, becomes force-free rather than vacuum (Chodura & Schlüter (1981)). The coordinate system used does not require nested flux surfaces in the initial equilibrium but, since flux is conserved, the magnetic surface topology can not change during relaxation.

NEAR (Hender *et al.* (1985)) uses very similar methods to Chodura and Schülter's code but with a Eulerian coordinate system defined by the vacuum magnetic flux surfaces. This is a more efficient coordinate system but restricts the range of vacuum magnetic fields that can be studied. The coordinate system does allow islands to develop if flux conservation is replaced by longitudinal current restrictions. A conducting boundary at the last closed vacuum flux surface prevents this surface from changing shape.

BETA (Bauer *et al.* (1978)) uses the evolving flux surfaces as a Lagrangian grid with a free boundary condition allowing the last flux surface to change shape. In a Lagrangian coordinate system the potential energy is minimised over changes to the coordinate grid with the pressure and toroidal and poloidal fluxes on the grid trivially defined. Flux conservation and the flux coordinate system each prevent the use of this code to study islands.

VMEC (Hirshman *et al.* (1986))also uses a Lagrangian formulation of potential energy minimisation with the evolving magnetic flux surfaces defining the coordinate system. Because, in VMEC, each flux surface is specified by poloidal and toroidal harmonics, fast spectral methods can be used to choose coordinates which minimise W. Modifications to VMEC have allowed flux and mass conservation to be replaced by explicit specifications of toroidal current or pressure on each flux surface. The vacuum field can be specified either by fixing the shape of the last flux surface or with a free boundary condition.

3.3 Picard iteration

An alternative route to equilibrium is iterative solution of the magneto-static equations. This had not been much used in numerical simulations before the development of PIES (Reiman & Greenside (1986)), but it is similar to the approach

CODE NAME	Convergence procedure	ι and pressure constraints	Coordinate grid	Boundary conditions
BETA (Bauer *et al.* (1978))	Energy minimisation by steepest decent	Initial mass and flux distributions are conserved	Lagrangian grid using evolving flux surfaces	Free boundary
VMEC (Hirshman *et al.* (1986))	Energy minimisation with spectral methods	Either specification of $\iota(\psi)$ or with a no net toroidal current condition, direct specification of $p(\psi)$	Lagrangian coordinates based on evolving flux coordinate system	Fixed shape of outer flux surface, or free boundary
Chodura and Schulter (Chodura & Schlüter (1981))	Energy minimisation with conjugate gradient method	Initial mass and flux distributions are conserved, longitudinal currents evolve to preserve rotational transform profile	Eulerian grid using a rectangular cross-sectioned ring of cylindrical coordinates	Conducting wall connected to plasma boundary by flat pressure region
NEAR (Hender:1985)	Energy minimisation with conjugate gradient method	Initial mass and flux distributions are conserved	Eulerian grid of vacuum flux coordinates	Conducting boundary at the outer flux surface fixing the shape of this surface
PIES (Reiman & Greenside (1986))	Picard iteration	Direct specification of $p(\psi)$ and net toroidal current (usually set to zero)	Lagrangian grid of flux coordinates with interpolation between good surfaces to allow for islands	Fixed shape of outer flux surface
HINT (Harafuji *et al.* (1989))	Ohmic relaxation alternated with parallel pressure relaxation	Zero net longitudinal current given implicitly by resistive relaxation, initial pressure profile specified but may evolve	Helically rotating Cartesian grid	Conducting wall connected to plasma boundary by flat pressure region

Table 3.1: 3D MHD equilibrium codes discussed in this chapter

used for the analytic theory of island growth introduced in the last chapter. First $\mathbf{J_n} \times \mathbf{B_{n-1}} = \nabla p_{n-1}(\psi)$ is solved for an estimate of the plasma current, $\mathbf{J_n}$. Then the field caused by this plasma current is found, by solving $\mathbf{J_n} = \nabla \times \mathbf{B_n}$ for the field, $\mathbf{B_n}$, subject to the condition $\nabla \cdot \mathbf{B} = \mathbf{0}$. The equilibrium is constrained by explicitly setting the pressure function, $p(\psi)$, and the net toroidal current (which would be zero for stellarator equilibria).

Finding the perpendicular part of the plasma current is straightforward with

$$\mathbf{J}_\perp = (\mathbf{B} \times \nabla p)/\mathbf{B^2}.$$

The parallel current is less straightforward to determine unless a magnetic coordinate system and Fourier components are used, in which case the total plasma current is given (as shown in the previous chapter) by

$$\mathbf{J}_1 = p'(\psi) \left[\sum_{l,m \neq (0,0)} \{ -\frac{\mathcal{J}_{lm}(\psi)}{\iota(\psi) - m/l} \} e^{il\theta - im\phi} \nabla\psi \times \nabla(\theta - m\phi/l) + \mathcal{J}_{00}(\psi) \nabla\theta \times \nabla\psi \right]$$

The restriction to good magnetic surfaces excludes the consideration of islands in the equilibrium field, which this integration scheme would otherwise be very suitable for modelling. PIES gets round this by using a quasi-magnetic coordinate system which matches to magnetic surfaces where these surfaces exist and interpolates between them for islands. Islands are detected by measuring the deviation of field lines from the quasi-magnetic surface and the current and pressure are set to zero within these islands. The coordinate system must be recalculated for each iteration of the magnetic field but this computation time is made up for by the simplification of the current calculations.

Solving the equilibrium field caused by the plasma currents is more difficult. It is made easier by dividing it into two parts. First a field, $\mathbf{h}$, is found that satisfies $\nabla \times \mathbf{h} = \mathbf{J}$ but is not divergence free.

$$\mathbf{h} = \int_\psi^{\psi_e} \mathcal{J}_{00}\, p'(\psi^*)\, d\psi^*\, \nabla\phi + p'(\psi) \sum_{nm} \sin(n\phi - m\theta) \frac{\mathcal{J}_{nm}}{(n - \iota m)} \nabla\psi$$

Next a correction, ∇u, to make the field divergence free is calculated by solving $\nabla^2 u = -\nabla \cdot \mathbf{h}$. This correction incorporates the boundary conditions which determine the field from external currents. The boundary conditions are set by specifying the shape of the last closed flux surface.

3.4 Resistive MHD

Adding resistive and viscous terms to ideal MHD allows energy to be dissipated so that following the equations for sufficient time will bring them to steady state. Source terms for pressure and density are needed for this steady state to be non-trivial and to contain a pressure gradient. The MHD equations with added

resistivity η, viscosity μ, thermal conductivity κ density source S_ρ, and pressure source S_p are:

$$\rho\frac{\partial \mathbf{v}}{\partial t} = -\rho\mathbf{v}\cdot\nabla\mathbf{v} - \nabla p + \mathbf{J}\times\mathbf{B} + \mu\nabla^2\mathbf{v} \tag{3.16}$$

$$\frac{\partial \mathbf{B}}{\partial t} = \nabla\times(\mathbf{v}\times\mathbf{B} - \eta\mathbf{J}) \tag{3.17}$$

$$\frac{\partial \rho}{\partial t} = -\nabla\cdot(\rho\mathbf{v}) + S_\rho \tag{3.18}$$

$$\frac{\partial p}{\partial t} = -\mathbf{v}\cdot\nabla p + \gamma p\nabla\cdot\mathbf{v} + \rho\nabla\cdot[\kappa\cdot\nabla(\tfrac{p}{\rho})] + S_p \tag{3.19}$$

$$\nabla\times\mathbf{B} = \mu_0\mathbf{J} \tag{3.20}$$

These will converge to a steady field that nearly satisfies the magneto-static equations with a zero net longitudinal current condition, $<\mathbf{J}\cdot\mathbf{B}>=0$. The current and field of the steady state can be made arbitrarily close to a magneto-static equilibrium by reducing η and μ.

These equations form the starting point for a method of calculating equilibrium MHD solutions. Since we are only interested in reaching the final state with minimum computation, rather than an exact modelling of the transient stages produced by resistive MHD, there are adjustments that can be made to speed up convergence.

The equations can be simplified by setting $\rho = 1$, and eliminating Eqns. 3.18 and 3.19 by providing a separate mechanism to relax pressure along field lines and achieve $\mathbf{B}\cdot\nabla p = 0$. This pressure relaxation step is alternated with a field relaxation step with Equation 3.16 simplified to :

$$\frac{\partial \mathbf{v}}{\partial t} = \nabla p + \mathbf{J}\times\mathbf{B} + \mu\nabla^2\mathbf{v}, \tag{3.21}$$

and combined with Eqns. 3.17and 3.20 which are evolved at constant pressure. This equation set has a steady state that tends towards exact solution of the magneto-static equilibrium as the product $(\eta\mu)$ tends to zero (Park *et al.* (1986)). Relaxation speed can be improved, without reducing accuracy, by using high resistivity with very low viscosity.

This approach is used in the HINT code (Harafuji *et al.* (1989)) and also in HIBS using "reduced heliac equations" (Park *et al.* (1986)).

3.5 Outline of the HINT code

HINT uses the method described in the previous section to find MHD equilibria satisfying the magnetostatic equations. The equations are solved on a Eulerian grid that gives an efficient coverage of a stellarator field without restricting the treatment of unusual or changing magnetic topology. This coordinate grid is described in Sect. 3.6. The use of resistivity to dissipate the energy of the initial conditions gives an implicit condition for zero net longitudinal current and allows the field topology to change during relaxation.

The desired pressure profile shape, $p(\psi)$, is set as an initial condition using the vacuum field flux surfaces. The pressure is evolved in a fashion that minimises the change in pressure profile shape during the relaxation to equilibrium. If the pressure

profile drifts significantly during the relaxation it can be reset for the flux surfaces of the equilibrium field.

The boundary condition is equivalent to a conducting wall some distance from the last closed flux surface. The pressure and plasma velocity at the wall are set to zero. The magnetic field component perpendicular to the wall is held constant. There is no special treatment of the region between the last closed flux surface and the simulation boundary except that the pressure is set to zero. It acts as a force-free plasma rather than strictly as a vacuum.

The calculation of an equilibrium magnetic field using HINT follows the following steps:

1. The vacuum field is calculated for each point on the simulation grid. This method of determining the vacuum field at each grid point will vary depending on the particular stellarator configuration. Where the magnetic field is based on known coil currents which are well approximated by circles or closed polygons, the field can be calculated by using expansions of elliptic integrals and Biot-Savart's law.

2. An arbitrary initial pressure profile is defined and then relaxed so that the pressure is constant over a magnetic flux surface. The contours of the relaxed pressure profile are than used to determine the toroidal flux of the surface. The toroidal flux values are interpolated back onto the simulation grid using the relaxed pressure profile.

3. The initial pressure profile is set, at very small peak pressure, using the flux calculated at step 2. The pressure profile is a flux function of the form $p(\psi) = p_0(1 - (\psi/\psi_E)^\alpha)^\beta$, where ψ_E is the toroidal flux of the outer flux surface.

4. The pressure is gradually increased between alternate relaxations of field and pressure distribution. Increasing the pressure gradually maintains the shape of the pressure profile and reduces other possible convergence problems by ensuring that the plasma never gets too far from equilibrium. The following three steps are iterated until the desired peak pressure is increased:

    - The pressure is relaxed along field lines to achieve $\mathbf{B} \cdot \nabla p = 0$. The magnetic field is constant during this step. There are two different methods of pressure relaxation described in Sect. 3.8. The methods conserve average pressure over a flux surface which helps to maintain the pressure profile.
    - The pressure at each grid point is increased by multiplying by a scaling factor. The scaling factor is generally reduced as the pressure increases
    - The field is relaxed, with the pressure fixed, using the reduced resistive MHD equations introduced in the previous section. This step is described in more detail in Sect. 3.7.

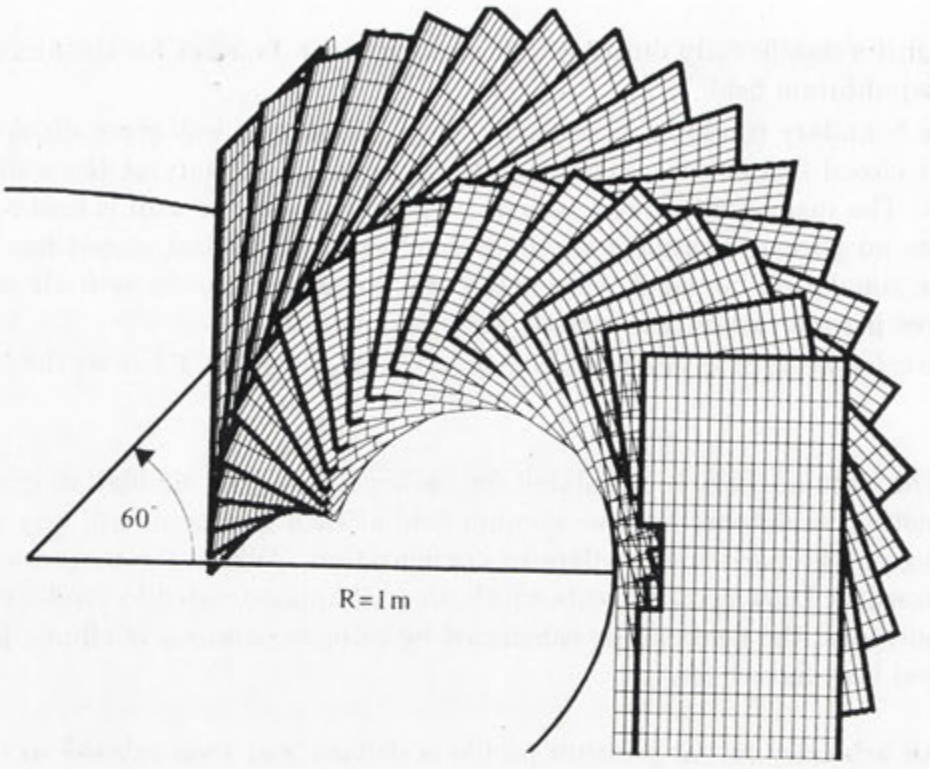

Figure 3.1: The HINT coordinate system for a helical axis stellarator

5. The field and pressure are relaxed further keeping the peak pressure constant. The iteration of field and pressure relaxation is repeated until the equilibrium is satisfactorily converged.

3.6 Coordinate system

The HINT coordinate system consists of a set of rectangular Cartesian grids on constant ϕ planes which rotate around the major axis of a toroidal configuration (see Fig. 3.6). The simulation boundary can be offset from the toroidal axis at R_0, allowing helical axis stellarators to be handled efficiently.

Conversion from the HINT coordinates (x, y, f) to cylindrical coordinates R, Z, ϕ is given by:

$$\begin{aligned} R &= R_0 + (x+\delta)\cos(hf) + y\sin(hf) \\ Z &= y\cos(hf) - (x+\delta)\sin(hf) \\ \phi &= -f \end{aligned}$$

where R_0 is the major radius of the torus, δ should be set approximately to the amplitude of the helical deviation of the magnetic axis and h is the helical pitch of the magnetic axis and coordinate system. Stellarator symmetry is used to give

reflection boundary conditions on the toroidal boundaries so that the simulation grid only needs to cover half a field period.

This coordinate system is not orthogonal and it will be necessary to convert between contravariant and covariant representations for making the necessary vector computations. The covariant components of the metric tensor used to do this are given by

$$\begin{aligned} g_{11} = g_{22} &= 1 \\ g_{12} = g_{21} &= 0 \\ g_{13} = g_{31} &= hy \\ g_{23} = g_{32} &= -h(x+\delta) \\ g_{33} &= R^2 + h^2\left((x+\delta)^2 + y^2\right) \end{aligned}$$

The Jacobian of the transformation is $\mathcal{J} = \sqrt{g} = R$. There are several factors to consider in the placement of the computational boundary:

- The boundary should be far enough from plasma (and from where plasma will migrate to as pressure increases) to act as a "free boundary" rather than as a fixed conducting boundary.
- The simulation region should exclude all singular currents, and be a sufficient distance from them to avoid numerical instabilities from high fields.
- The simulation area should be as small as possible to reduce computational costs.
- The boundary shape should be as simple as possible.

A rectangular boundary is simplest to deal with for the rotating Cartesian grid used by HINT. However for H-1 with a helical current near the axis of rotation, any rectangular boundary either brought the boundary too close to the helical current so that the field relaxation was numerically unstable in this region, or brought the boundary too close to the plasma at the bean tips which reduced the plasma region significantly below that expected in the experiment. A rectangular bite taken out of the simulation area, nearest to the central conductor (see fig 3.1). It involved an implementation of the boundary conditions for a convex rather than concave corner. Many of the initial computations carried out during this project were made using this boundary.

In 2002, Hayashi [Hayashi, private communication] developed a modification to the field relaxation algorithm which reduced the effective Alfven speed around the helical currents and so removed the associated numerical instabilities. This allowed a simple rectangular boundary to be used with the helical current. All results in Chapters 6 and 7 of this thesis use this modified field relaxation and a simple rectangular boundary.

3.7 Field Relaxation

In the field-relaxation step, the magnetic field, current and plasma velocity evolve according to:

$$\mathbf{J} = \nabla \times \mathbf{B} \tag{3.22}$$

$$\frac{\partial \mathbf{v}}{\partial t} = \mathbf{J} \times \mathbf{B} - \nabla p - \mu \nabla^2 \mathbf{v} \tag{3.23}$$

$$\frac{\partial \mathbf{B}}{\partial t} = \nabla \times (\mathbf{v} \times \mathbf{B} - \eta \mathbf{J}) \tag{3.24}$$

The resistivity, η, and viscosity, μ, are arbitrary. HINT uses high resistivity but minimal viscosity to improve convergence without sacrifycing the accuracy of the final state. (In fact the small viscosity was found to have minimal effect and is set to zero to reduce computation time.) With zero viscosity, the steady-state magnetic field of Eqns. 3.22-3.24 satisfies the magneto-static equations exactly but the parallel plasma viscosity is arbitrary. However, discretisation errors will result in some effective numerical viscosity.

During this step the pressure is fixed while the flux surfaces move. This introduces some pressure gradients along the field lines which cannot be balanced by the $\mathbf{J} \times \mathbf{B}$ force, so the equations cannot relax completely to steady state unless they are alternated with a pressure relaxation step.

In order to calculate $\partial \mathbf{B}/\partial t$ and $\partial \mathbf{v}/\partial t$ from the field values stored on the grid, spatial derivatives are estimated by four-point finite differences. This gives covariant components of the gradients. For example, the covariant component of the pressure gradient in the x direction is given by:

$$\nabla p_x = \frac{\partial p(i,j,k)}{\partial x} = \frac{p(i-2,j,k) - 8p(i-1,j,k) + 8p(i+1,j,k) - p(i+2,j,k}{12\Delta x}$$

For Eqn. 3.22, the contravariant components of the current are determined from the partial derivatives of the covariant components of the magnetic field (calculated from finite differences as for the pressure gradient).

$$J^x = (\frac{\partial B_y}{\partial f} - \frac{\partial B_f}{\partial y})/\mathcal{J}$$

The calculation of the spatial derivatives have some errors which can have a substantial impact on the current calculation, especially near the singular currents creating the vacuum field, where the field gradients are changing rapidly. To minimise these errors, a current calculation is made on the vacuum field (for which the current should be zero) and this vacuum current is subtracted from the equilibrium current calculation.

To get the covariant components of $\partial \mathbf{v}/\partial t$, the contravariant components of $\mathbf{B}$ and $\mathbf{J}$ combine to get the covariant components of $\mathbf{J} \times \mathbf{B}$:

$$(J \times B)_x = (J^y B^f - J^f B^y)\mathcal{J}$$

These are combined with the covariant components of the pressure gradient to give covariant components of the velocity change.

$$\frac{\partial v_x}{\partial t} = (J \times B)_x + \nabla p_x$$

The contravariant velocity and magnetic field components, and the covariant components of the current are needed to get the contravariant components of $\partial \mathbf{B}/\partial t$:

$$\begin{aligned} E_x &= (v^y B^f + v^f B^y)\mathcal{J} - \eta J_x \\ \frac{\partial \mathbf{B^x}}{\partial t} &= (\frac{\partial E_y}{\partial f} - \frac{\partial E_f}{\partial y})/\mathcal{J} \end{aligned} \tag{3.25}$$

Where necessary covariant components are transformed into contravariant components using the metric of the previous section. The magnetic field, current and fluid velocity are each stored as their contravariant components but are also used in their covariant form.

Using the above calculations for the contravariant components of $\partial \mathbf{B}/\partial t$ and $\partial \mathbf{v}/\partial t$, the relaxation equations are progressed according to the Runge-Kutta method:

$$\mathbf{B}_{i+1/4} = \mathbf{B}_i + \frac{1}{2}\frac{\partial \mathbf{B_i}}{\partial t}\Delta t \tag{3.26}$$

$$\mathbf{B}_{i+2/4} = \mathbf{B}_{i+1/4} + \left(1 - \sqrt{1/2}\right)\left(\frac{\partial \mathbf{B_{i+1/4}}}{\partial t} - \frac{\partial \mathbf{B_i}}{\partial t}\right)\Delta t \tag{3.27}$$

$$\begin{aligned} \mathbf{B}_{i+3/4} = \mathbf{B}_{i+2/4} &+ \left(1 + \sqrt{1/2}\right)\left(\frac{\partial \mathbf{B_{i+2/4}}}{\partial t} - \right. \\ &\left. \left[2\left(1 - \sqrt{1/2}\right)\frac{\partial \mathbf{B_{i+1/4}}}{\partial t} - \left(1 - 3\left(1 - \sqrt{1/2}\right)\right)\frac{\partial \mathbf{B_i}}{\partial t}\right]\right)\Delta t \end{aligned} \tag{3.28}$$

$$\begin{aligned} \mathbf{B}_{i+1} = \mathbf{B}_{i+3/4} &+ \frac{1}{6}\left(\frac{\partial \mathbf{B_{i+3/4}}}{\partial t} - \right. \\ &2\left\{2\left(1 + \sqrt{1/2}\right)\frac{\partial \mathbf{B_{i+2/4}}}{\partial t} - \left(1 - 3\left(1 + \sqrt{1/2}\right)\right) \times \right. \\ &\left.\left.\left[2\left(1 - \sqrt{1/2}\right)\frac{\partial \mathbf{B_{i+1/4}}}{\partial t} - \left(1 - 3\left(1 - \sqrt{1/2}\right)\right)\frac{\partial \mathbf{B_i}}{\partial t}\right]\right\}\right)\Delta t \end{aligned} \tag{3.29}$$

This method is numerically unstable on the HINT equation set without some spatial smoothing of $\partial \mathbf{B}/\partial t$ and $d\mathbf{v}/dt$. The spatial smoothing introduced in HINT averages over the surrounding grid points using

$$\frac{\partial \mathbf{B}}{\partial t}_s(i) = \left(-\frac{\partial \mathbf{B}}{\partial t}(i-2) + 4\frac{\partial \mathbf{B}}{\partial t}(i-1) + 10\frac{\partial \mathbf{B}}{\partial t}(i) + 4\frac{\partial \mathbf{B}}{\partial t}(i+1) - \frac{\partial \mathbf{B}}{\partial t}(i+2)\right)/16$$

applied in each of the three dimensions.

Making the numerical solution of Eqns. 3.22 to 3.24 stable also requires a restriction on the time step for a given grid spacing. For a wave equation of the form:

$$\frac{\partial^2 A}{\partial t^2} = c\frac{\partial^2 A}{\partial x^2}$$

stability requires that the time step is smaller than the rate the wave travels from one grid point to the next $\Delta t < c\Delta x$. (This restriction may be altered a little in higher order schemes but the essential restriction is fundamental.) The relevant wave speed for HINT stability is the Alfvén wave speed $c = v_A = \sqrt{B^2/(\mu_0 \rho)}$. The high magnetic fields near vacuum field coils can cause numerical instability at time steps where the bulk of the plasma is stable. Careful placement of the simulation boundary can reduce this problem, but jagged boundaries can cause other numerical problems. A modification to the field relaxation has been introduced to remove this problem (Hayashi *et al.* (2000))

Solving a dispersive equation numerically introduces a time step restriction that scales differently. For a standard equation

$$\frac{\partial A}{\partial t} = c\frac{\partial^2 A}{\partial x^2}$$

the restriction on the time step is $c\Delta t < \Delta x^2$ The field relaxation equations have the dissipative term introduced by resistivity in order to get the plasma energy to decay to equilibrium. I have found the maximum field relaxation time step to be limited by both wave and dispersive stability requirements $\Delta t < \Delta x^2/\eta$ and $\Delta t < v_A \Delta x$. This limits the extent to which increasing the resistivity can increase the convergence rate of the field relaxation.

3.8 Pressure relaxation

There are two quite dissimilar methods used to relax pressure with the standard versions of HINT. The first is based on a system of artificial sound equations which satisfy $B \cdot \nabla p = 0$ at equilibrium. A second method was added to improve the accuracy of the new pressure if islands are present. In this method, the relaxed pressure at a grid point is the average pressure along the field line passing through that grid point. I will introduce a third pressure relaxation, to improve the efficiency of pressure relaxation for low shear fields containing magnetic islands, in the next chapter.

3.8.1 Method of artificial sound wave (PR1)

The pressure can be relaxed by modelling damped sound waves flowing along the field lines driven by the pressure gradient (Park *et al.* (1986)). A system of equations describing the evolution of sound waves parallel to the magnetic field is: $\partial p/\partial t = \mathbf{B} \cdot \nabla v_a$ and $\partial v_a/\partial t = \mathbf{B} \cdot \nabla p$. Clearly the stationary state of this system must be a solution to the desired relaxed pressure condition $\mathbf{B} \cdot \nabla p = 0$, however evolution of this system will not tend to a steady state since there is no mechanism for energy dissipation. "Kinetic-energy quenching" is introduced to provide this energy dissipation and bring this system efficiently to its steady state without changing the equilibrium solution. To do this, the total, volume averaged, kinetic energy of the system is monitored. When this reaches a maximum and begins to diminish the velocity is reset to zero.

Subsequent peaks in kinetic energy are smaller, with quenching repeated at each maximum. The system is seen to converge for a typical case, with both total kinetic energy and the volume averaged error measure $\mathbf{B} \cdot \nabla p = 0$ tending to zero (Harafuji *et al.* (1989)).

The method of progressing these two equations is very similar to that used in field relaxation. Spatial derivatives are calculated by the same four-point centered-differences used in the field relaxation step. The equations are progressed in time by a four-step Runge-Kutta method with spatial smoothing of the time derivatives (also identical to that used in the field relaxation step).

The system has a stability condition

$$\Delta t \leq \frac{\Delta x}{c}$$

.

3.8.2 Method of field line following (PR2)

The condition $\mathbf{B} \cdot \nabla p = 0$ is equivalent to no pressure variation along field lines. This can be achieved by assigning a new pressure at each grid point based on an average of the pressure taken along a field line passing through the grid point.

Field lines are traced from each grid point according to the equations:

$$\frac{dx}{df} = B^x / B^f$$
$$\frac{dy}{df} = B^y / B^f$$

which are advanced with an eight step Runge-Kutta method. The time step, Δf, was chosen to be a twentieth of a half-field period.

Values of the magnetic field between grid points are found using a three dimensional polynomial interpolation from the nearest 2 grid points in each direction. The interpolation in one dimension is based on fitting a cubic polynomial to the magnetic field at the four closest grid points. To extend the interpolation to three dimension this interpolation is applied to each dimension in turn. First the magnetic field is interpolated in the x direction to a set of 16 points on a plane with the same x coordinate as the field-line position but with the same y and f coordinates as the grid. Then these 16 points are used to find the pressure at a set of four points along a line including the field-line position which can be used to find the magnetic field at that point.

At each step the pressure at the field-line position is calculated from a linear interpolation from the surrounding 8 grid points. This interpolation does not need to be as accurate as the interpolation of the field since the errors from the pressure interpolation are reduced by averaging, while errors in field carry through to later steps in the field-line tracing.

The pressure is added to the pressure sum along the field line with a flux weighting to ensure the volume averaged pressure within a flux surface is not altered by

the pressure relaxation. At any one time only the current field-line position and the pressure sum need to be stored.

CHAPTER 4

Improvements to the HINT algorithm for Pressure relaxation

In this chapter I present a new algorithm I developed to increase the speed of HINT's pressure relaxation for low shear stellarators with islands.

Achieving a flat pressure profile within islands is vital to modelling the non-linear factors involved in island growth. The time taken to relax pressure within islands using HINT's standard pressure relaxation method is particularly slow for low shear stellarators and can take more than 90% of the computation time for a simulation. The length of this calculation effects the feasibility of calculating island sizes for a wide range of plasma pressure values and vacuum fields, or for doing long relaxation time convergence studies of HINT.

In Section 4.1, I will explain why HINT's pressure relaxation is comparatively slow for islands in low shear stellarator fields and how the standard methods are inefficient. Section 4.2 details the new algorithm and justifies the choice of interpolation method. Section 4.3 tests the ability of the new pressure relaxation to flatten the pressure within islands. Section 4.4 shows the success and failure of the new algorithm depending on the measure used for residual error and discusses why it should do better on one measure than the other. It presents a refinement to the new algorithm to fix its degradation of one error measure, and shows that the final algorithm produces better results on all measures of residual error. The new algorithm produces identical results to the old in a significantly reduced time for well converged pressure profiles.

4.1 Pressure relaxation time for low-shear stellarators

A standard method of pressure relaxation in HINT (method PR2 described in Sect. 3.8.2) follows a field line from each grid point and uses the average pressure along the field line to give the relaxed pressure at that grid point. To make the pressure constant over a flux surface the field line must be followed long enough to give a representative sampling of the pressure on the flux surface. For example, the outermost field line trace in Fig. 4.1 is within a region of nested flux surfaces and is evenly covered by 50 field periods of field line tracing. By contrast, the inner field line is within a magnetic island and does not give a representative sampling of the

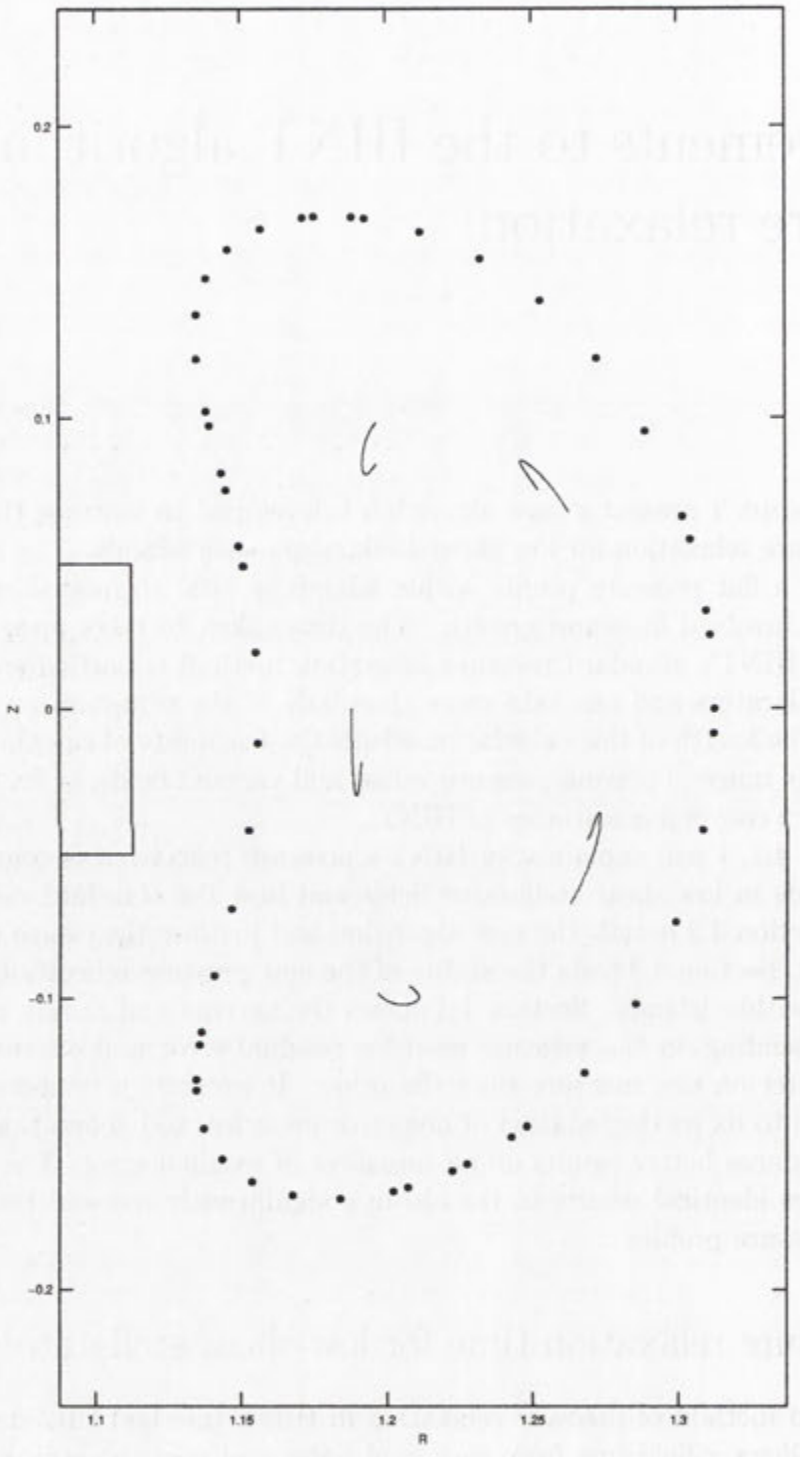

Figure 4.1: Intersections of two field lines with the $\phi = 0$ plane. The outer field line was followed for fifty periods. The inner is within a magnetic island and was followed for 750 periods.

magnetic surface even though it has been traced for 750 field periods. If the island has formed or moved since the previous pressure relaxation step, longer tracing of the field line may sample a region with substantially different pressure. A field line within a magnetic island needs to be traced for at least one island rotation period in order to give pressure flattening over the island.

In Section 3 of Chapter 2, I showed that the island rotation period at the centre of the island was:

$$\tau = \frac{2}{l\,\delta r\,d\iota/dr},$$

where δr is half the island width measured in average minor radius. This shows that longer field line tracing will be needed for small islands and in low shear fields. Since the bean of a helical axis stellarator is itself a magnetic island its shear is small. The magnetic shear within islands was shown to approach zero at the island's centre, in Chapter 2 Section 3 and, in agreement with this analysis, the shear of the H-1NF heliac was found to approach zero at the magnetic axis in Chapter 5 Section 1. For the lowest shear H-1NF configuration I examined, an island having a width equal to the HINT grid spacing has a rotation period of 800. Thus, to properly relax the pressure at a grid point within the island, one needs a field line to be traced for 800 periods on the full torus. In the PR2 pressure relaxation method, field lines are traced from each grid point, in a three dimensional grid. In an H1-NF case this might require about 200,000 field lines ($73 \times 73 \times 36$) to be traced for 800 periods each in order to achieve pressure flattening within all islands, wider than a grid spacing. To achieve pressure flattening in islands smaller than a grid spacing would require longer field line tracing, but the effect of the pressure flattening of an island this small on pressure gradient and other equilibrium quantities would be impossible to resolve.

Another standard method of pressure relaxation in HINT (PR1 described in Sect. 3.8.1) models damped sound waves travelling along magnetic field lines. The convergence time of this method is also dependent on the length of field line tracing needed to cover a flux surface. The sound wave simulation must be relaxed for long enough for sound waves to travel from high pressure areas of the magnetic flux surface to low pressure areas. It is even slower than PR2 for low shear fields with islands and potentially accumulates significant numerical diffusion errors if run for this long.

Even with the 50 (or so) periods of field line tracing needed in regions of nested flux surfaces, well away from rational surfaces, there is a lot of information contained in the field line trace that is not being used by the PR2 method. In PR2 the average pressure along the field line is used to calculate the pressure at the initial grid point. The relaxed pressure should be the same all along the field line, so from this single field line we know the relaxed pressure not just for the initial point but also for very many other points spread over the magnetic surface. We should be able to use this information to help find the pressure at grid points near the magnetic surface and to make a more efficient pressure relaxation process.

4.2 New Algorithm

In my new pressure relaxation algorithm (which I will refer to as PR3) a set of field lines are followed, and the average pressure along them is calculated, using the same process as is used for the field line tracing in PR2. However, in PR3, I save the position of the field line at each step of the field line tracing. I also reduce the ϕ step of the field line integration to match the HINT grid spacing so that the field line position is saved at each ϕ grid plane. The average pressure along the field line is taken as the relaxed pressure for all the points along the field line. For H1-NF, I chose 365 field lines, giving 5 per grid spacing in the x direction, with initial points bisecting the $\phi = 0$ plane. (The intersections of these field lines with the $\phi = 0$ plane, over 750 field periods of field-line tracing are shown in Fig. 4.2.) This gives a large number of points at which the relaxed pressure is known. These points can be considered as sample points of the new relaxed pressure from which we can interpolate the relaxed pressure at the grid points. Having all the sample points on the ϕ grid planes reduces the interpolation problem to two dimensions.

There are special cases that need to be considered where the interpolation points lie close to magnetic islands or to the plasma boundary. The sample points are evenly spread over most of the plasma volume. In these regions (as shown in Fig. 4.3a) there will be many sample points close to any given grid point. This should give plenty of information for determining the relaxed pressure at the grid point. Figure 4.3b shows that the sample points near a magnetic island are not so evenly distributed. Also, the pressure in this region will have an abrupt change in slope at the island boundary because of pressure flattening within the island. The sample points in this region do contain enough information to determine the relaxed pressure at all the grid points but a simple interpolation method may give inaccurate results. The choice of interpolation method is discussed in Section 4.2.1, below.

If there is an island in the magnetic field that has an X-point coinciding with the line of initial points for the field lines, then none of the field lines will go within the island and the situation will be even worse than that shown in Fig. 4.3b. A grid point within this island may have no sample points near it. Grid points need to be tested for this problem, and more field lines traced near grid points where this is found to be the case.

Grid points outside the last closed flux surface are also likely to have no points of known relaxed pressure near them because field lines in this region quickly intersect with the simulation boundary. The pressure at these grid points should be set to zero. We need to distinguish between the grid points that have no sample points near them because they are outside the plasma boundary and those that are within the plasma but have no sample points near them because they are within a magnetic island. Otherwise new field lines will be traced, for the full 750 periods, from all the grid points outside the plasma boundary, which will make the PR3 method needlessly slow.

One method for distinguishing which HINT grid points are outside the plasma region, is to start with a few periods of field-line tracing from every grid point. Most

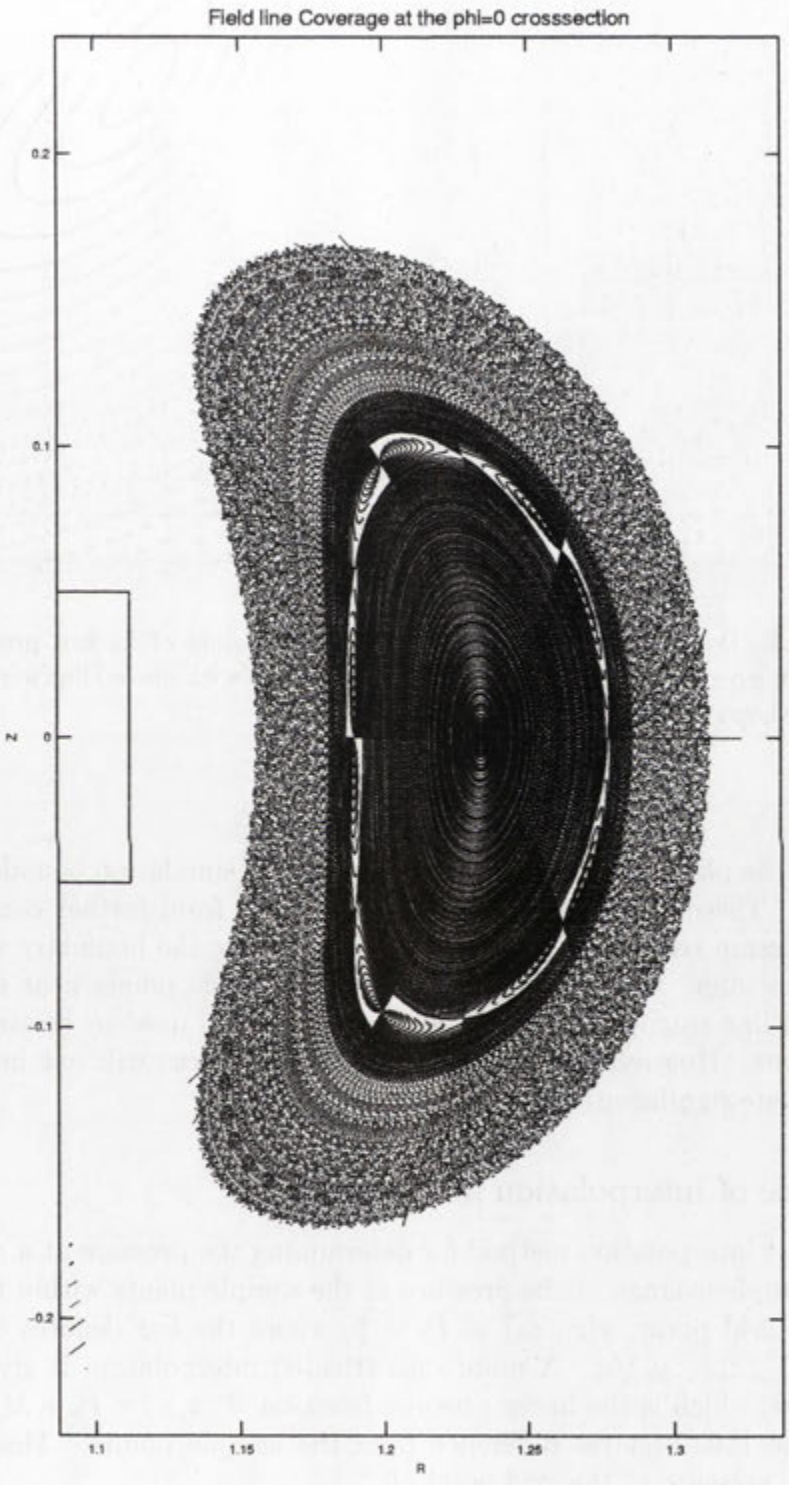

Figure 4.2: Poincaré section at $\phi = 0$ with 365 field lines followed for 750 field periods each. This gives a dense covering of points for most of the plasma region

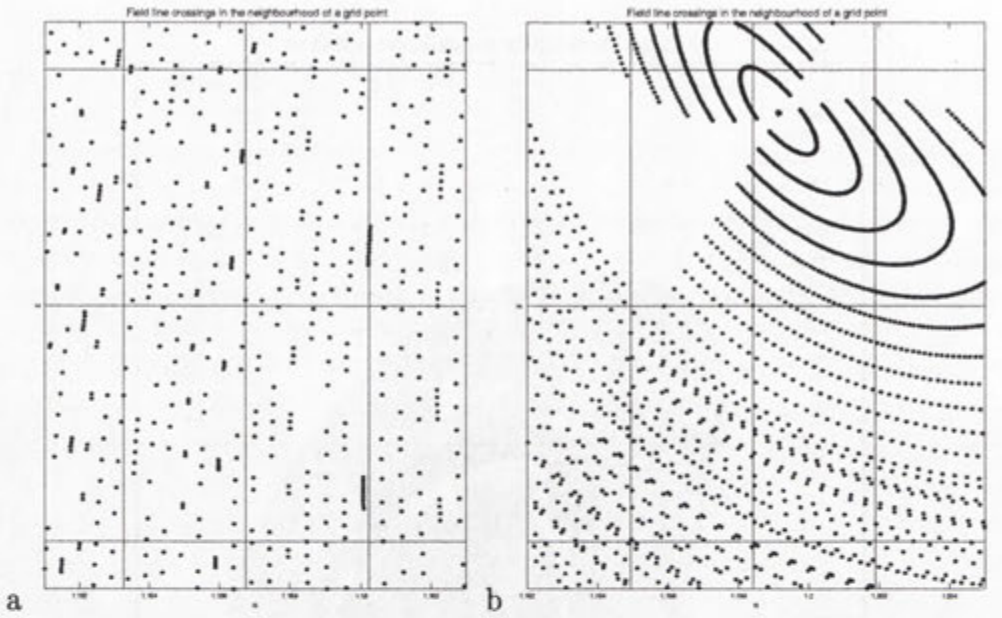

Figure 4.3: Detail of previous Fig. 4.2 showing points of known pressure surrounding a grid point. a) shows a region of plasma with nested flux surfaces while b) shows a region near an island

points outside the plasma boundary will connect to the simulation boundary within a few periods. These can be set to zero and removed from further consideration during this pressure relaxation step. Some points outside the boundary will not be detected at this step. They are likely to have no sample points near them after the initial field-line tracing and extra field-line traces will need to be started from these grid points. However these few extra field-line traces will not increase the computation time significantly.

4.2.1 Choice of interpolation method

The simplest interpolation method for determining the pressure at a grid point, (x_0, y_0), is a simple average of the pressure at the sample points within half a grid spacing of the grid point, $p(x_0, y_0) \approx P_1 = \overline{p}$, where the bar denotes the simple average, $\overline{a} = \sum_n a(x_n, y_n)/n$. A more sophisticated interpolation is given by the plane of best fit, which is the linear pressure function, $P(x, y) = P_0 + M_x x + M_y y$, which gives the least squares difference from the sample points. This gives an estimate of the pressure at the grid point of:

$$p(x_0, y_0) \approx P_2 = \overline{p} - \frac{(\overline{x} - x_0)M_x + (\overline{y} - y_0)M_y}{(\overline{y^2} - \overline{y}^2)(\overline{x^2} - \overline{x}^2) - (\overline{xy} - \overline{x}\,\overline{y})^2} \tag{4.1}$$

with $M_x = (\overline{xp} - \overline{x}\,\overline{p})(\overline{y^2} - \overline{y}^2) - (\overline{yp} - \overline{y}\,\overline{p})(\overline{xy} - \overline{x}\,\overline{y})$ and $M_y = (\overline{yp} - \overline{y}\,\overline{p})(\overline{x^2} - \overline{x}^2) - (\overline{xp} - \overline{x}\,\overline{p})(\overline{xy} - \overline{x}\,\overline{y})$. The average pressure, P_1, gives the same estimate for

the pressure at the grid point as the plane of best fit, P_2, if the sample points are symmetrically spaced on either side of the grid point so that $\overline{x} = x_0$ and $\overline{y} = y_0$.

The distribution of sample points is not generally symmetric on either side of a grid point. Flux surfaces near the center of the plasma have smaller areas than flux surfaces near the plasma boundary. The flux surface area grows in proportion to its average distance from the magnetic axis, r. A field line traced on a flux surface with small surface area will give more densely-spaced sample points than a field line traced over a large-surface-area flux surface for the same number of periods. Thus, if field lines are spaced evenly across the plasma radius, the distribution of sample points will be denser near the magnetic axis than at the plasma edge, falling off as $1/r$. This sample point distribution will make the pressure estimate at the grid points produced by P_1 consistently higher than the pressure estimate given by P_2 over the same sample points.

The uneven distribution of points can be partly compensated for by spacing field lines evenly in ψ rather than r, since ψ is closely related to the enclosed volume. Spacing evenly in ψ gives an even distribution of field lines per volume and a more even distribution of sample points. However, there is a minimum separation in r so that every grid point has at least two field-lines passing through its local region. To space the initial points as evenly as possible in ψ, taking into account the minimum spacing in r, I use a spacing for the initial points of the field line of: $\Delta x_{\text{field line}} = 1/(A(x - x_{\text{axis}}) + 2/\delta x_{\text{grid}})$, with A chosen to fit the desired number of field lines across the plasma. The sample points given by these field-lines are evenly distributed in regions of nested flux surfaces well away from the magnetic axis. In this region the average pressure and plane of best fit give similar, and accurate, estimates of the relaxed pressure at the grid points. A comparison of these two methods applied to the grid point in the centre of Fig. 4.3a is shown in Fig. 4.4.

The field-line spacing I have chosen does not give as even a distribution of sample points near the magnetic axis as it does away from the axis because of the restriction on a minimum spacing in r. Magnetic islands will also cause sample points to be unevenly distributed (as was seen in Fig. 4.3b). In these regions the average pressure will be less accurate than the plane of best fit.

Near a magnetic island, the pressure distribution is also far from linear. In this case a simple plane of best fit will not give a good approximation to the pressure at the grid point. A better estimate of the pressure at the grid points is achieved by weighting the sample points according to their distance from the grid point. I used the weighted average defined by:

$$\overline{a} = \frac{\sum_n a(x_n, y_n)/(\,((x - x_0)/\Delta x)^2 + ((y - y_0)/\Delta y)^2 + \varepsilon)}{\sum_n 1/(\,((x - x_0)/\Delta x)^2 + ((y - y_0)/\Delta y)^2 + \varepsilon)} \tag{4.2}$$

to replace the averages in the calculation of the plane of best fit (Eqn. 4.1) to give a better pressure estimate, P_3. The addition of the small quantity $\varepsilon \ll 1$ limits the weighting to a maximum value of $1/\varepsilon$ for a sample point exactly on the grid point. This is necessary to prevent overflow errors in the code when a field line is started exactly on the grid point. Using weighted averages effectively reduces the area over which sample points contribute to the pressure estimate at a grid point

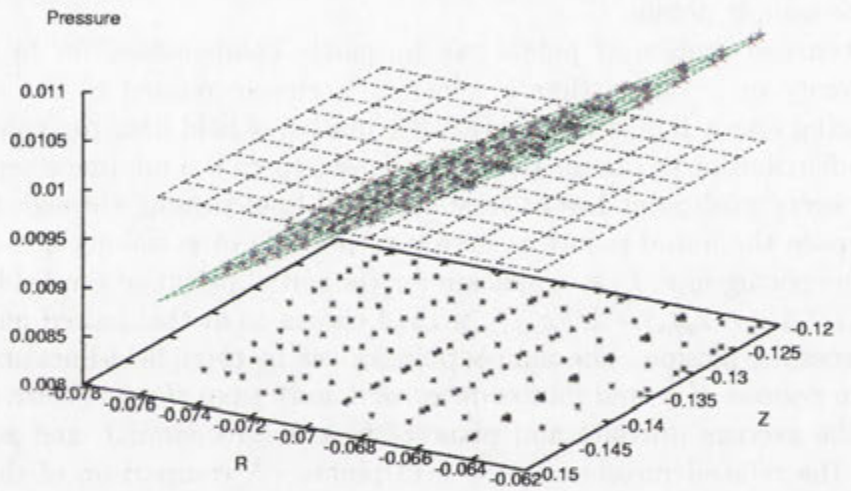

Figure 4.4: Because the sample points are evenly spaced around the grid point the average pressure (grey lines) and the plane of best fit (green lines) intersect to give nearly identical estimates of the relaxed pressure at the grid point. In this region the pressure given by the plane of best fit at the sample points (red crosses) matches to the relaxed pressure at the sample points (blue crosses) very well. The pressure in this region is nearly linear over a grid spacing.

and this reduces the error from ignoring the nonlinearity of the pressure profile. to non-linear terms in the pressure profile.

I use P_3 for my pressure estimate for most of the HINT grid points inside the plasma boundary. However there are a number of special cases that make the weighted plane of best fit unusable or inaccurate. These cases need to be detected and then dealt with by some other interpolation method. The special cases and their treatments follow:

- If a single field-line contributes all the sample points within an area any interpolation method will give the relaxed pressure for this field line as an estimate of the pressure at the grid point. Unless the field line passes though the grid point it would be more accurate to include points from a second field line so that the pressure gradient can be taken into account. This is tested for after the initial set of field lines is traced and an additional field line is started from the grid point to increase the accuracy of the interpolation for this grid point.

- If one sample point very close to the grid point dominates the weighted averages the denominator of the plane of best fit may become very large making the calculation inaccurate. In this case the weighted average of the pressure is a better approximation and is used instead.

- Two closely spaced field lines at the edge of the island (one within island and one outside) can have quite different average pressures. If these two field lines dominate the sample points then the resulting plane of best fit can be very steep. In this case, if both field lines are the same side of the grid point, the plane of best fit result is inaccurate. A weighted average of pressure is more reliable for locally steep pressure gradients.

- Grid points just outside the plasma region are not always detected during the initial testing for the outside grid points described earlier this section. The sample points for these grid points will all be on the plasma side of the grid point and the interpolated pressure may be negative. Any grid point that gets a negative pressure estimate from the plane of best fit has its pressure reset to zero.

To some extent, the computation time savings of the new method are offset by increases in memory requirements. Saving the positions of all the sample points can increase the memory needed by HINT substantially. This memory requirement can be reduced by running the field lines in batches. It is not necessary to save the positions of all the sample points after a batch of field lines have been completed. All that is needed for this interpolation method is to save the contribution of the sample points to the eight weighted averages used to calculate the plane of best fit.

4.2.2 Procedure for the new algorithm

The new algorithm for relaxing pressure is as follows:

1. Determine whether HINT grid points are inside or outside the last closed flux surface. I do this by tracing a field line from each point for a small number of periods. Most outside points will connect to the simulation boundary within this field line length.

2. Determine a set of initial points for field lines. By default these are spread along the $y = 0$ line bisecting the $\phi = 0$ cross-section. The x-range is from one edge of the plasma boundary to the other (using the boundary found in Step 1). The field line spacing is chosen to get as even a spread of sample points as possible.

3. The field lines are followed, and average pressure along them calculated, using the same method as is used in PR2 (detailed in Sect. 3.8.2) but with a step length equal to the HINT ϕ grid spacing. The field lines are traced for enough periods to get a representative covering of each magnetic surface, including those within islands. I have generally used 250 toroidal periods of field-line tracing. The position of the field lines is saved at each step.

4. For each saved field-line position the average pressure for the field line is used to calculate its contribution to the nearest grid point of the weighted sums, $\overline{(x-x_0)P}$, $\overline{(y-y_0)P}$, $\overline{(y-y_0)^2}$, $\overline{(x-x_0)^2}$, $\overline{(x-x_0)}$, $\overline{(y-y_0)}$, $\overline{P}$ and $\overline{(x-x_0)(y-y_0)}$. The contribution of the sample points to the total weight is also saved.

5. Grid points are tested for sufficient information content. If either the total weight of sample points near them is too small, or if all the points come from a single field line, a new field line is traced from this point. When a batch (365) of new field line starting positions have been found, steps three and four are repeated. Grid points are again tested for their ability to get a good pressure estimate and the process is repeated until all grid points satisfy this condition.

6. Weighted sums are converted to weighted averages and then used to form a plane of best fit estimate of the pressure over the HINT grid. Special cases, where the plane of best fit does not provide a good estimate, are detected and the appropriate alternatives are applied.

4.3 Test for ability to flatten pressure profile within islands

I compared the ability of the PR3 and PR2 methods to flatten pressure within an island of an H1-NF equilibrium field. The PR2 algorithm was introduced to increase the ability of HINT to flatten pressure in islands as compared to the PR1 method. I used a test magnetic field with an island several grid spacings wide and an

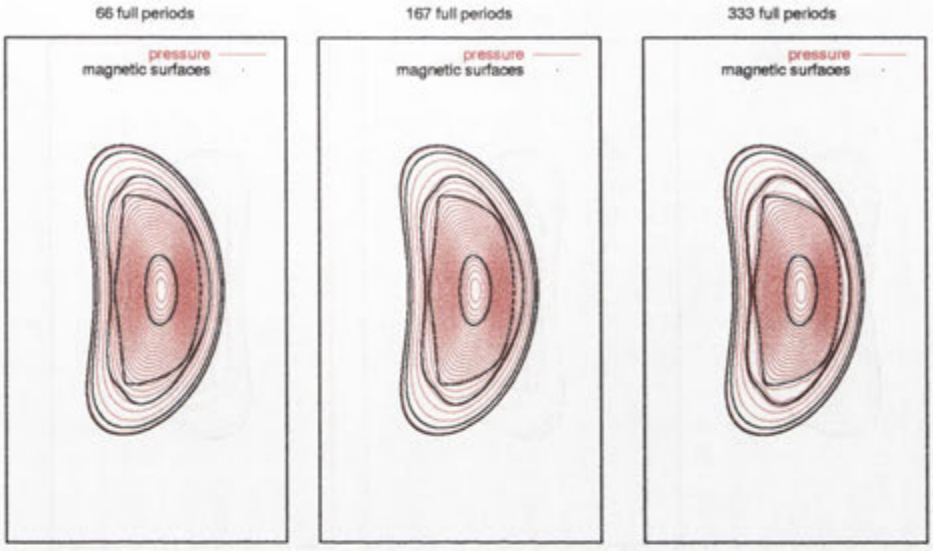

Figure 4.5: Pressure flattening within island develops as full field-line pressure relaxation, PR2, is extended to 300 periods. The island width is about two grid spacings which is the smallest that can be expected to be resolvable.

arbitrary initial pressure displaced from the flux surfaces of this test field. The two pressure relaxation methods were trialed using various lengths of field-line tracing.

For the full field-line tracing method, PR2, no flattening of pressure within the island is visible until after 300 periods of field-line tracing (Fig. 4.5). The full field-line tracing for 300 periods of the full torus, took 8 hours of computation time on the Fujitsu VPP300. For the new method, PR3, pressure flattening within the island starts to be visible at 250 periods, and extends to the island edge by 1000 periods (Fig. 4.6). The length of field-line tracing is confirmed as the dominant factor in achieving pressure profile flattening within an island. In contrast with the PR2, 1000 periods of field-line tracing with PR3 took only 11 minutes because many fewer field-lines were traced. Thus the speed of pressure relaxation has been increased by a factor of 40. The PR3 method gives (to the eye) good, smooth pressure contours matching the flux surfaces. It gives a very similar pressure profile to PR2 if long enough field-line tracing is used (See Fig. 4.7). Away from magnetic islands the two pressure profiles match exactly. Within magnetic islands PR3 gives a slightly flatter profile. The consequences of any differences between the relaxed pressure profiles, for the overall convergence of the HINT simulations will be described below.

4.4 Pressure convergence in regions of good flux surfaces

Having established that the new method is much faster at flattening the pressure profile within islands, it is necessary to check that its performance at pressure relaxation away from magnetic islands.

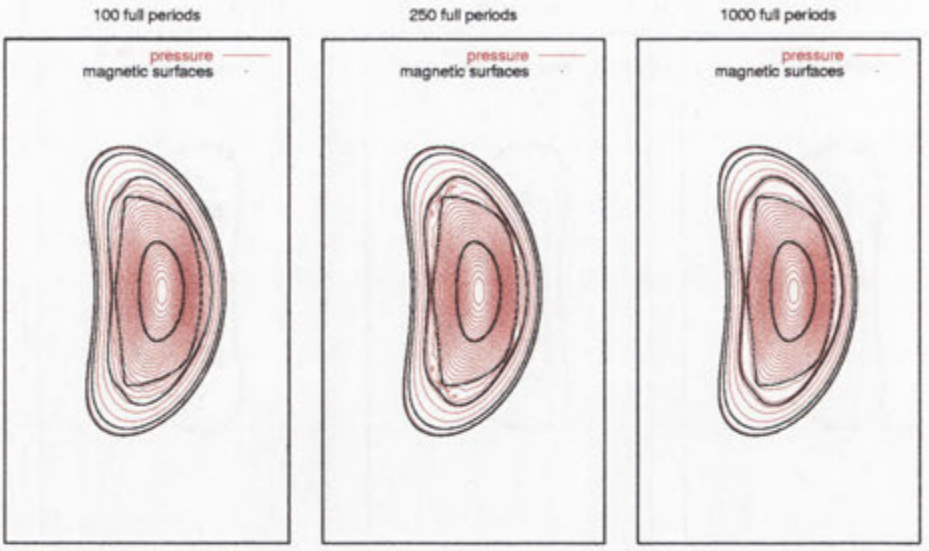

Figure 4.6: Pressure flattening within island using my new method of pressure relaxation. The island width is about two grid spacings which is the smallest that can be expected to be resolvable.

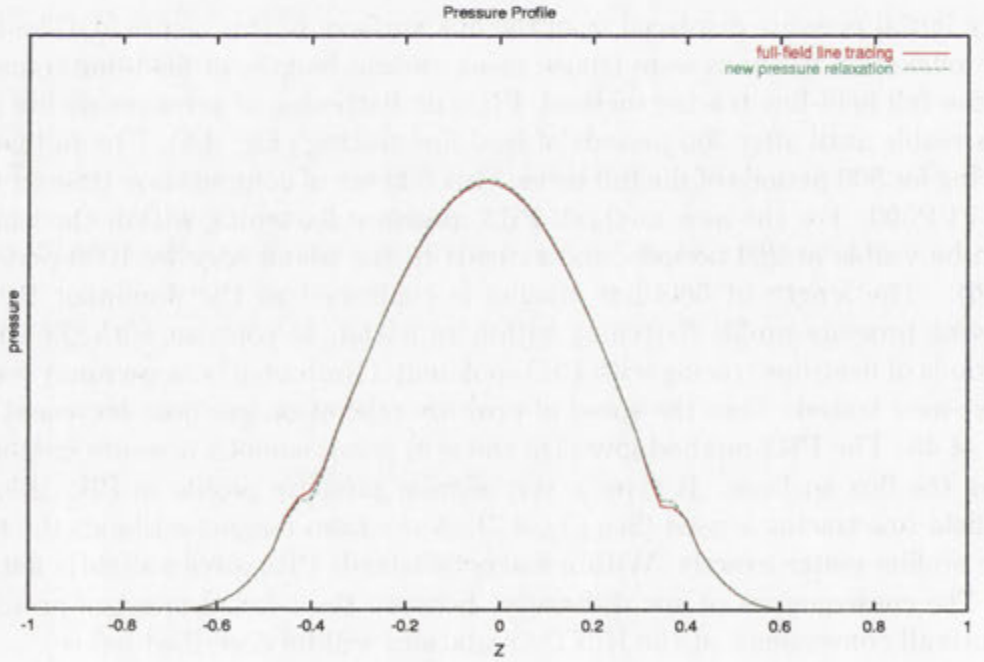

Figure 4.7: Pressure profile along a cross section at $x = 0$, $\phi = 0$ line. PR3 with 750 half-field periods of field line tracing has a nearly identical profile to PR2 with 333 half-field periods of field-line tracing. Small differences can be seen near the island.

There are three main sources of error that PR2 and PR3 share.

- Errors will accumulate in the position of the field line due to round off in the ODE integrator. These would obviously lead to errors in the average pressure along the field line. Examination of Poincaré sections shows that the field line traces form well preserved surfaces even after a thousand periods of field line tracing. This indicates that the error from this source will not be significant (but these errors may increase with longer field-line tracing).

- There will be an error in interpolating the pressure from the HINT grid to the field line. As long as the error is not systematic, its impact on the average pressure of the field line will be reduced by cancellation. The effect of 'random' interpolation errors will decrease as the field line tracing length increases, introducing more points into the pressure average. A systematic error in interpolation may change the shape of the pressure profile but it will not lead to a pressure variation over a flux surface.

- There is an error component from the field line not covering a representative sample of the flux surfaces. This is the error that leads to most of the pressure gradient within flux surfaces inside an island and is reduced by longer field-line tracing.

My pressure relaxation method, PR3, introduces a new error source from the interpolation from sample points back to the HINT grid. For PR3 to be a useful method the interpolation errors should be less than the errors accumulating from the other sources at the desired field line tracing length.

PR1 has a different set of errors associated with it. There is an error due to incomplete relaxation of the sound-wave, similar to the error from too short field-line tracing, which is decreased by increasing the relaxation time. There are also discretisation errors. The steady state for the sound-waves has $\mathbf{B} \cdot \nabla p = 0$ with the pressure gradient determined by finite differences. The discretisation errors in the pressure gradient mean that the steady state of PR1 has some pressure variation over flux surfaces. However, minimising of $|B \cdot \nabla p|$ may make the relaxed pressure fit better as input to the HINT field relaxation step, which uses the same method for calculating the pressure gradient. There are also numerical diffusion errors associated with PR1 which change the pressure profile and which increase with relaxation time.

I use the pressure variation along a sample set of n field lines, ξ_1, as a measure of long scale errors remaining in the relaxed pressure.

$$\xi_1 = \frac{\sum_n \sqrt{(\overline{p^2})_n - (\overline{p})_n^2}}{\sum_n (\overline{p})_n}$$

The field-line tracings used in this error calculation should be longer than any trace used in the pressure relaxation method. This will detect a failure of the pressure relaxation method to achieve pressure flattening within islands, and will also give a general measure of the convergence of the relaxation method. The interpolation of

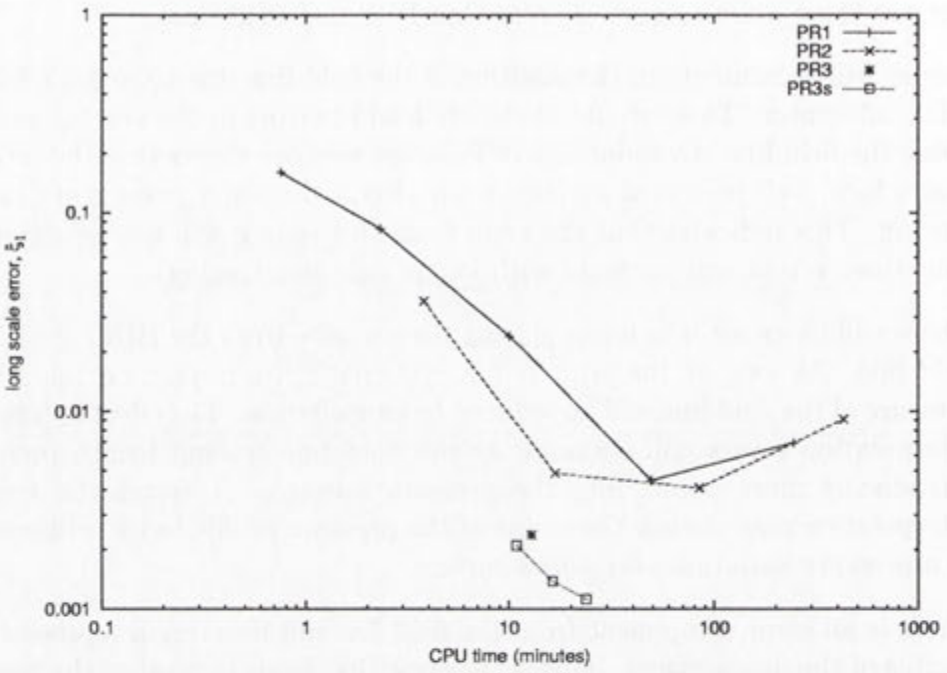

Figure 4.8: Convergence comparison for the different pressure relaxation methods using the long scale error measure ξ_1.

pressure onto field line needs to be more accurate for the calculation of this pressure variation than was necessary for the calculation of average pressure, since errors in interpolation will show up as extra variation and give an unnecessarily high error measure. Interpolation errors during the error calculation are a particular problem near island boundaries. The cubic polynomial interpolation method described in Sect. 3.8.1 is used to find both the magnetic field and the pressure at the field line for this error calculation

Comparisons of the convergence of the three pressure relaxation methods, using this measure, are shown in Fig. 4.8. My new pressure relaxation method was significantly faster at reducing pressure relaxation along a field lines.

A short scale error measure is the local pressure variation in the field direction:

$$\xi_2 = < \frac{|\mathbf{B} \cdot \nabla p|}{|\mathbf{B}|\,|\nabla p| + \epsilon} >$$

taken as a volume weighted average over all HINT grid points within the plasma. This detects local errors in the pressure relaxation but does not give any indication of the larger scale errors involved in pressure gradients across an island. The pressure gradient is approximated by finite differences from surrounding grid points. I expect some error in this measure to remain even in the long convergence limit of both field-line tracing methods, from discretisation in the calculation of ∇p. The sound wave modelling method uses this error measure directly in its relaxation, so it could achieve lower errors by this measure without actually being more relaxed. For this

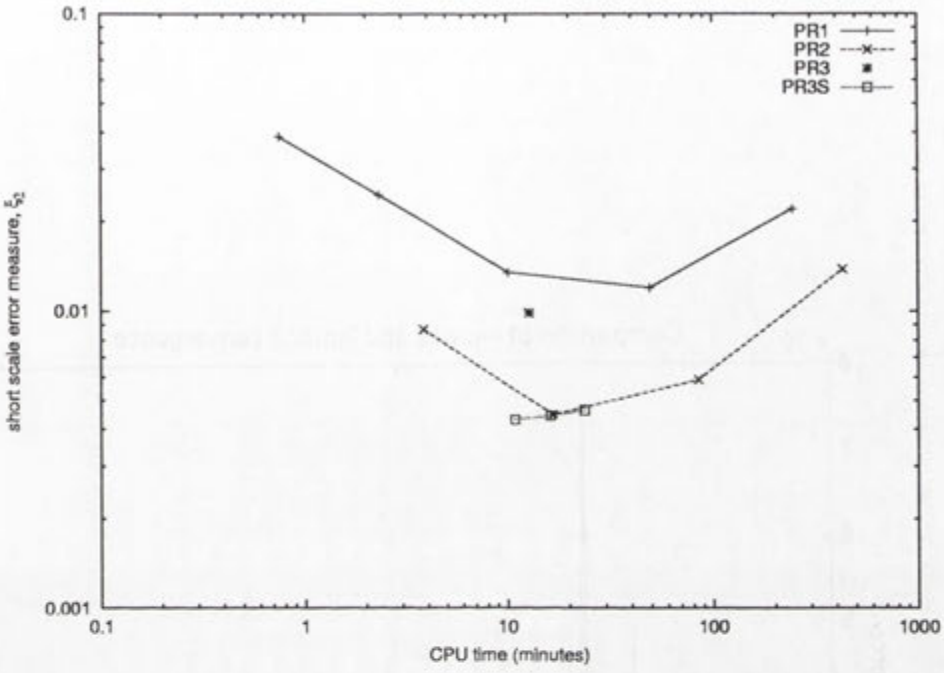

Figure 4.9: Convergence comparison for the different pressure relaxation methods using the short scale error measure ξ_2.

measure of error my new pressure relaxation algorithm was less accurate than PR3 (See Fig. 4.9). Surprisingly PR1 did not do any better by this error measure.

This error measure is related to the parallel component of the residual force in the field relaxation, $\nabla p - \mathbf{J} \times \mathbf{B}$, and will impact on the ability of the field relaxation to converge. The worse ξ_2 error for PR3 is reflected in the worse overall convergence of HINT using PR3 compared to PR2 (as shown in Fig. 4.10). The local error, ξ_2, in the pressure gradient produced by PR3 has a large impact on the convergence of a full HINT simulation and needs to be removed.

The worse outcome of PR3 on the measure ξ_2 is due to errors introduced during the interpolation process. Errors from insufficient field-line tracing are systematic and slowly varying. These large-scale errors vary little from grid point to grid point along the field-line. They do not show up in ξ_2 and they do not cause large errors in the pressure gradient or add significantly to the residual force in the field relaxation. Errors in PR3 caused by interpolation from sample points to grid points are small but random. Even though the total range in pressure over a field-line is smaller for PR3 than for PR2, all of this variation is experienced between one grid point and the next. This makes the effect on the pressure gradient and gives a large ξ_2 error.

I introduced a refinement to the new method to smooth this error away. Both of HINT's standard pressure relaxation methods are good at removing short scale pressure variation. A short version of either applied to the relaxed pressure from PR3 will reduce the local error in the pressure gradient. I used PR2 for this, because

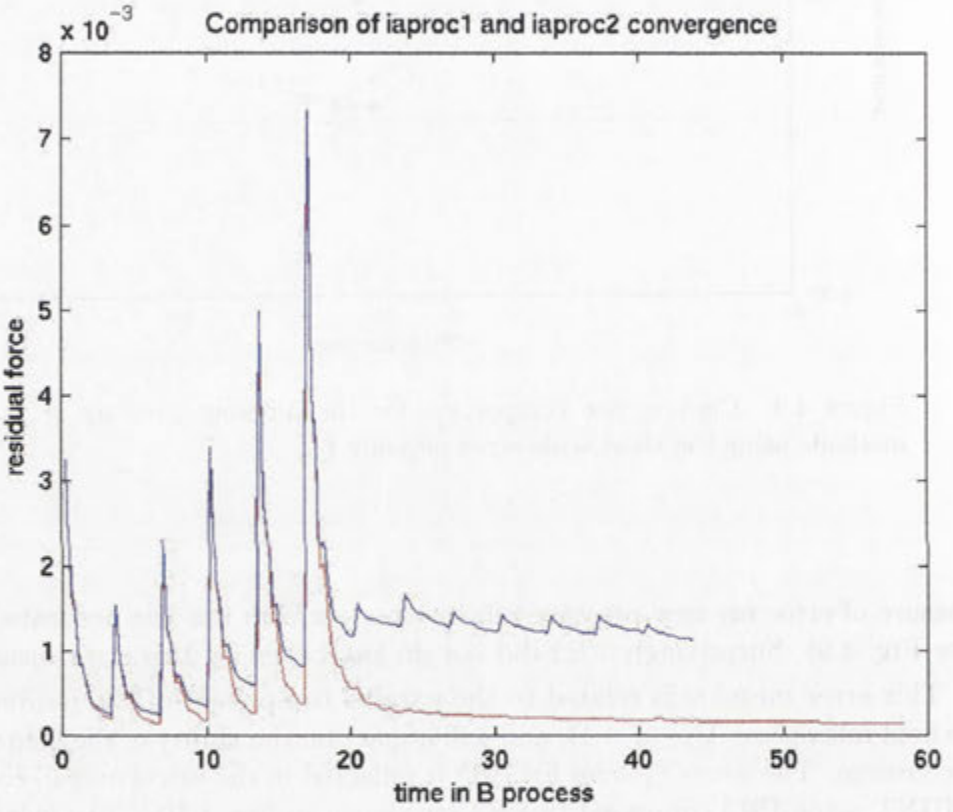

Figure 4.10: Comparison of the convergence of residual force during a HINT run, using PR2 (in red) or PR3 (in blue) for the pressure relaxation step. Large spikes in the residual force occur where the pressure relaxation is run, followed by an increase in the total pressure. Smaller peaks occur where the pressure is relaxed but the total pressure is unchanged.

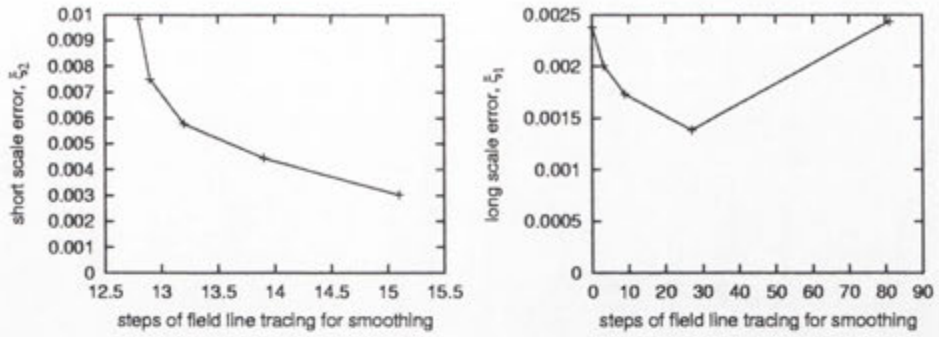

Figure 4.11: Effect on residual errors of PR3 of applying PR2 (with only a few steps of field line tracing) as a smoothing device

it is less likely than PR1 to perturb the large-scale constancy of pressure over a flux surface that PR3 has achieved. In Fig. 4.11a, I show the improvement in the ξ_2 error when PR2 is applied to the results of PR3 using only a few steps of field-line tracing. Only about 27 steps of field-line tracing are needed for PR2 to reduce ξ_2 significantly, so this adds only about 10% to the computation time of PR3. Smoothing over 27 steps does not degrade the large scale pressure relaxation measured by ξ_1, in fact removing the short scale variation improves this measure (Fig. 4.11b).

This hybrid pressure relaxation method, PR3s, converges faster in both the global, (ξ_1) and local (ξ_2) measures of pressure relaxation (Fig. 4.8 and 4.9 respectively). The convergence of residual force in a HINT simulation, using PR3s for pressure relaxation is as good as that using PR2, but uses less computation time.

The ξ_1 and ξ_2 error measures are not particularly effective for determining when the pressure contours around the magnetic island fit the field line comparison. I have found visual comparison to be the most reliable way of testing for pressure relaxation within islands. With parameters for field line tracing length adjusted for the simulation grid size and magnetic shear, the PR3s pressure relaxation method gives a good fit between pressure contours and flux surface topology for island widths down to two grid spacings. I have chosen this relaxation method for all the following simulations.

CHAPTER 5

HINT Results - Simulation Conditions and Methodology

In this chapter I describe the set up and method of the simulations I conducted using the HINT code. I include a description of the H-1NF stellarator and discuss the different configurations of H-1NF which I chose to study. I also specify the parameters of HINT used for these simulations and other particulars of the way the simulations were run. Section 5 describes the method used to calculate resistive stability criteria for the HINT simulations.

5.1 The H-1NF Heliac

The H-1NF Heliac is a three field period, medium sized, helical axis stellarator. It was built at the Australian National University in 1980s and commenced operation in 1990. H-1NF has a major radius of 1m and an average plasma minor radius of 21cm with a total plasma volume of $0.91m^2$ (Hamberger *et al.* (1990)). In its 'standard' configuration H-1 is designed to have a 1 Tesla magnetic field which can be sustained for a 1s pulse. This is sufficient time for the plasma to reach an effective steady state.

The vacuum magnetic field of H-1NF is generated from a set of fat circular coils, each made from windings of 29.2mm or 17.5mm square-section copper. These coils are relatively simple to construct and generate a field which is well approximated by circular current filaments, which can be calculated easily. The coil set (shown in figure 5.1) consists of:

- A central ring with 1m radius, carrying a current of 500kA, which generates the main part of the poloidal field.
- 36 toroidal field coils, radius 0.383m, with their centres located on a toroidal helix which rotates three times around the central ring with a helical displacement of 0.22m. Each of these coils carries a 139kA current and generate the toroidal part of the magnetic field.
- A set of four vertical field coils, parallel to the central ring, which are used to adjust the shape and position of the magnetic surfaces. The inner vertical

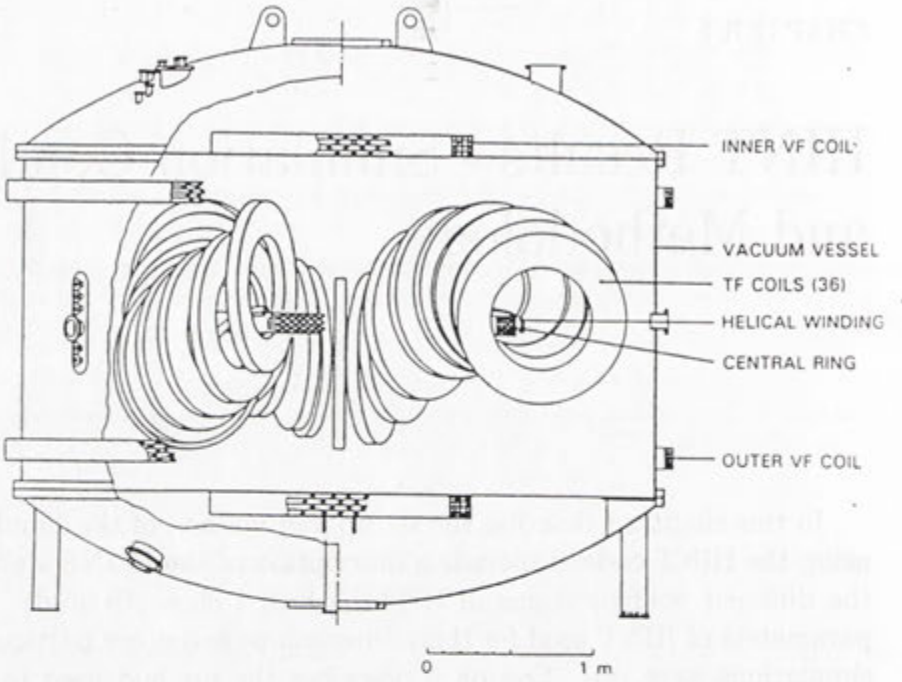

Figure 5.1: Diagram of the coil set and vacuum vessel of H-1NF, taken from Hamberger *et al.* (1990).

field coils have a radius of 0.72m and are placed 1.07m above and below the central ring. The outer vertical field coils have a radius of 2.0m and are placed 1.07m above and below the central ring.

- A helical winding (the only non-planar current component) winds around the central ring (helical displacement 9.5cm) in phase with the toroidal field coils. Current in this helical winding is used to alter the rotational transform of the magnetic fieldHarris *et al.* (1985).

These coils are placed inside a vacuum chamber 4m in diameter. This is cheaper and simper to construct than designing a vacuum chamber shaped to fit between the plasma and the coils.

The vacuum flux surfaces of this field are bean-shaped with a magnetic axis approximately coinciding with the helix on which the centres of the the toroidal field coils lie (flux surfaces for a standard vacuum field are shown in Fig. 5.2). The flux surface shape can be characterised by their ellipticity (the ratio of height to width) and their indentation, (full width – width at center)/(full width). These measures vary across the plasma with outer surfaces being more indented and fatter than surfaces near the magnetic axis, which are not indented at all (see Fig. 5.3). Ellipticity also varies around the torus. Cross-sections of flux surfaces tend to be thinner for when the bean is inward from the ring conductor.

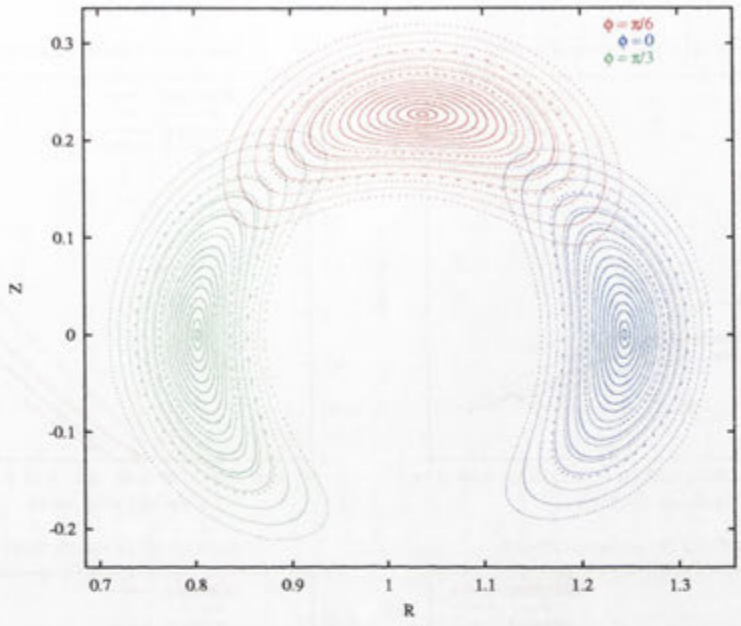

Figure 5.2: Flux-surfaces of the Standard configuration vacuum field at three cross-sections in ϕ.

These bean-shaped flux surfaces can be thought of as a large $l = 1$, $m = 3$ island of the field whose flux surfaces are centred on the ring conductor. The island perturbation is caused by the helical displacement of the toroidal field coils and the relative strengths of the toroidal and poloidal fields need to be chosen so that the rational surface of the 'main' field, which resonates with this perturbation, occurs at about the centre of the toroidal field coils.

Treating the bean-shaped flux surfaces as a magnetic island we can predict the rotational transform profile, using the theory of Sect. 2.3 for a single harmonic perturbation. The rotational transform profile, in the frame rotating with the island, is given by:

$$\iota_i = \frac{d\iota_m}{d\psi} C_R \left(1 - \frac{1}{4}\sin^2(\frac{\delta\theta}{2}) + \cdots\right), \tag{5.1}$$

where $\delta\theta$ is half the width in θ of the magnetic surface within the island, C_R is the strength of the radial field perturbation and ι_m is the rotational transform of the 'main' field in its unperturbed form. The coordinates θ and ψ also refer to the unperturbed field. The magnetic shear for this rotational transform is very low, tending to zero at the island's axis.

Since the perturbation strength also determines the ellipticity of island surfaces the rotational transform can be defined in terms of ellipticity near the island's axis. From the field-line invariant defined in Sect. 2.3 (Eqn. 2.12), we obtain an expression

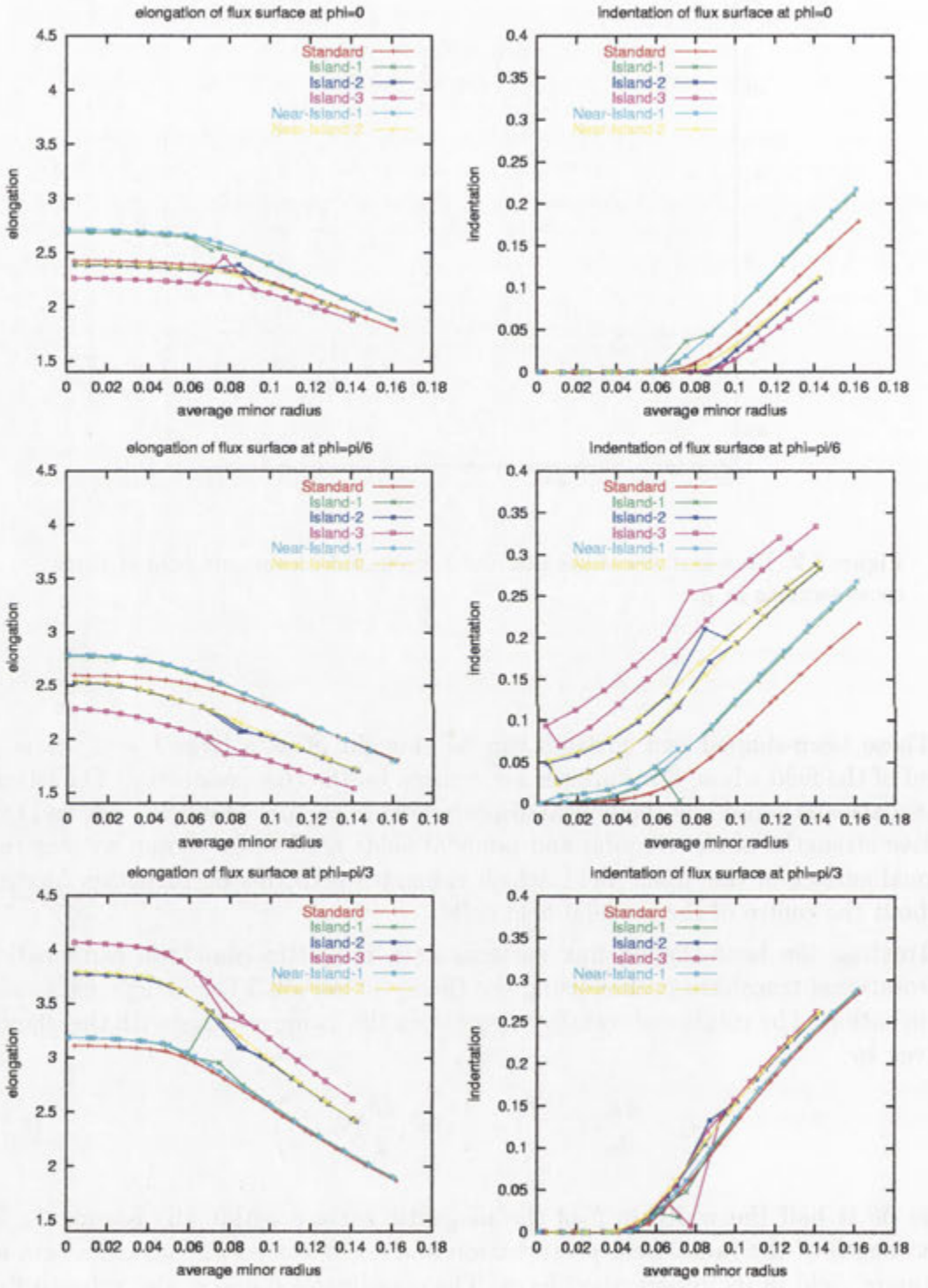

Figure 5.3: Elongation and indentation of flux surfaces of the different vacuum fields at three cross-sections in ϕ.

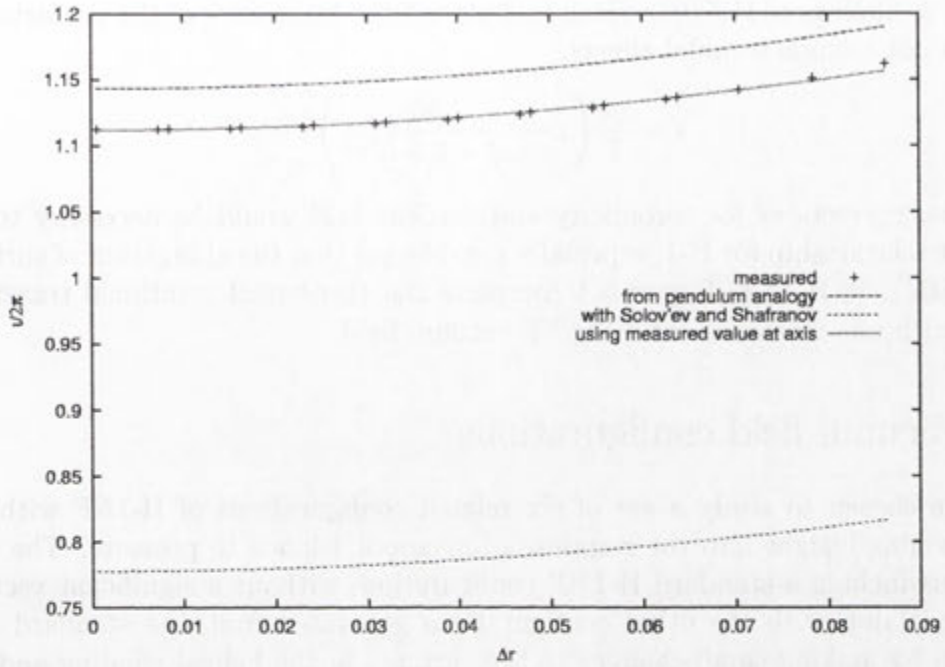

Figure 5.4: A comparison of predicted and measured rotational transform

for the island surface width (Gandy *et al.* (1993)):

$$\delta\psi = \sqrt{\frac{2C_R}{l\, d\iota_m/d\psi}(1-\cos(l\delta\theta))} \tag{5.2}$$

Using Eqn. 5.2 and Eqn. 5.1 the ellipticity of surfaces within an island is given by:

$$\begin{aligned}\varepsilon_l &= \frac{r\delta\theta}{\delta\psi(dr/d\psi)} \\ &= \frac{r\Delta\theta}{\iota_{\mathrm{i\,axis}}\sqrt{2(1-\cos(l\Delta\theta))}dr/d\iota_{mR}}\ .\end{aligned} \tag{5.3}$$

The magnetic shear of the main field is $d\,\iota_m/dr = -\,\iota_m/r$. Substituting this into Eqn. 5.3 and taking the limit near the island's axis we get an expression for the island rotational transform in terms of the ellipticity of surfaces near the centre of the island:

$$\iota_i = -\frac{m}{l\varepsilon_l}\left(1-\frac{1}{4}\sin^2(\frac{\delta\theta}{2})+\cdots\right), \tag{5.4}$$

This rotational transform is measured in a frame rotating with the island but it is more normal to measure it in a stationary frame giving $\iota = m/l + \iota_i$.

This is very similar (in the small island width limit) to the expression derived considering the field due to a helical solenoid surrounding a straight conductor

(Solovev & Shafranov (1970)), which includes all the harmonics of the perturbation but does not include toroidal effects:

$$\iota = \frac{m}{l}\left(1 - \frac{2\varepsilon_l}{\varepsilon_l^2 + 1 + h^2 r^2}\right).$$

Additional corrections for toroidicity and vertical field would be necessary to get the exact relationship for H-1, especially considering that the elongation of surfaces varies with ϕ in H-1NF. Figure 5.1 compares the theoretical rotational transform profiles with one measured for a H-1NF vacuum field.

5.2 Vacuum field configurations

I have chosen to study a set of six related configurations of H-1NF with the aim of gaining insight into the response of magnetic islands to pressure. The configurations include a standard H-1NF configuration, without a significant vacuum magnetic island, with the other configurations generated from the standard configuration by making small changes to the currents in the helical winding and the vertical field coils. I contrast the standard case with several configurations containing $\iota = 1.2$ rational surfaces with the corresponding 6/5 islands. The 6/5 island is convenient to study because the rotational transform is easily within the range available by altering the helical current and because these configurations have substantial vacuum islands. This island has been studied before, and configurations are known with opposite vacuum island phase (Hudson & Dewar (1997)). However, the island is not accessible to experimental studies and comparisons because there is a 5/4 error island that interferes with it.

In order to separate the contributions to island growth of external perturbations, local resonant currents, global resonant currents and global nonresonant currents I have varied the vacuum island phase and size and the magnetic well depth as well as examining similar configurations not containing any islands.

The six vacuum field configurations are summarised in Table 5.2 with their important features described below.

- Standard: A fairly standard configuration for H-1NF with good plasma confinement properties. Shear is moderate but avoids the lowest order rationals. The surfaces of the inner bean (at $\phi = \pi/3$) are slightly more elongated than the surfaces at the outer bean (at $\phi = 0$). The vacuum flux surfaces are shown in Fig. 5.2 The presence of a magnetic well improves stability to interchange modes.

- Island-1: A current through the helical winding, in the same direction as the main coil current, was added in order to bring $\iota = 1.2$ within the rotational transform range so that the corresponding 6/5 island could be studied. Otherwise the coil currents are identical to the Standard configuration. The added helical current increases the average elongation of the magnetic surfaces (see Fig. 5.5. This is consistent with the relationship between rotational transform

	Standard	Island-1	Island-2	Island-3	Near-Island-1	Near-Island-3
helical winding	0kA	15.4kA	16kA	16kA	16.6kA	17.2kA
inner vertical field coils	83kA	83kA	194kA	180kA	83kA	194kA
outer vertical field coils	22kA	22kA	121kA	140kA	22kA	121kA
rotational transform at axis	1.11	1.195	1.195	1.195	1.203	1.203
rotational transform at edge	1.16	1.225	1.212	1.212	1.233	1.22
lowest order rational	9/8	6/5	6/5	6/5	27/22	27/22
average island width	< 1mm	~7mm	~8mm	~8mm	<1mm	<1mm
R of magnetic axis at $\phi = 0$	1.244m	1.254m	1.237m	1.229m	1.254m	1.237m
R of magnetic axis at $\phi = \pi/3$	0.802m	0.797m	0.782m	0.788m	0.797m	0.788m
elongation near axis at $\phi = 0$	2.4	2.7	2.4	2.3	2.7	2.4
elongation near axis at $\phi = \pi/3$	3.1	3.2	3.8	4.1	3.2	3.8
magnetic well depth	.4%	.7%	-1.3%	-1.5%	.7%	-1.3%

Table 5.1: A comparison of the major varying features of the vacuum magnetic field configurations studied

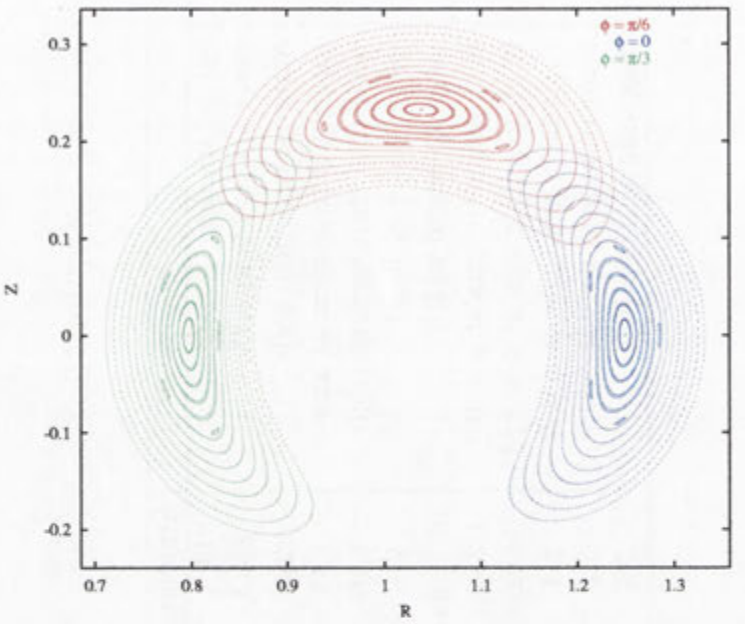

Figure 5.5: Flux-surfaces of the Island-1 configuration vacuum field at three cross-sections in ϕ.

and ellipticity shown in the previous section and implies that the helical current is partially counteracting the perturbation of the toroidal field coils. The helical current produces a mainly poloidal field increasing the poloidal field of the main current so the magnetic axis of the bean outward from the main coil (i.e. increasing its helical displacement).

- Island-2: The current in the vertical field coils is altered to change the phase of the island from that in Island-1. This configuration using the vertical field currents to alter the island was found by Hudson & Dewar (1997). Altering the vertical field distribution also changes the elongation of the surfaces and the rotational transform. The helical coil current was adjusted slightly so that the rational surface remained at the same point within the plasma as for Island-1. However the shear for this configuration is lower and the difference in elongation between the skinny surfaces at $\phi = \pi/3$ and the fatter surfaces at $\phi = 0$ is accentuated (See Fig. 5.6). Altering the vertical fields has also changed the magnetic well to a hill so the stability of this configuration to interchange modes is much reduced. The average major radius of the magnetic axis has decreased.

- Island-3: Starting from Island-2, the current in the inner vertical field coil is changed to 180kA and the current in the outer vertical field coil is increased to 140kA. This configuration extends the change from the Island-1 to Island-2 configuration. This 6/5 island is of the same phase as for the Island-2

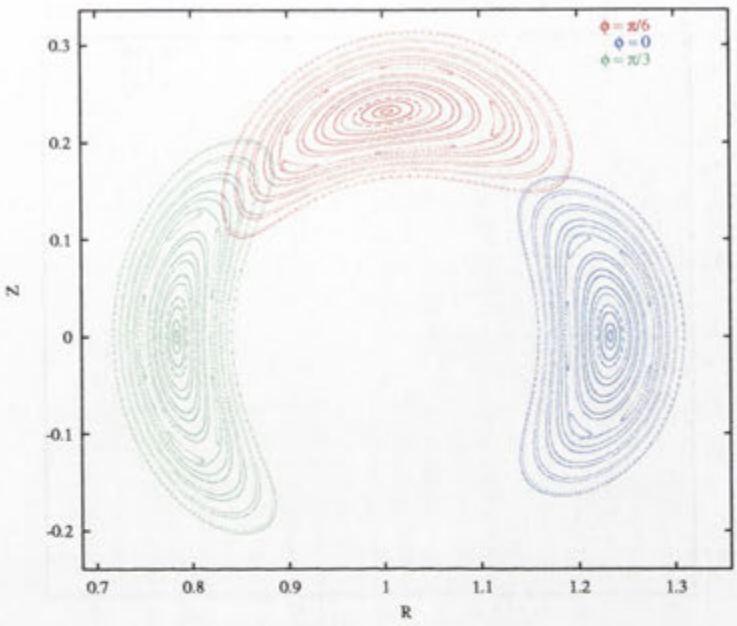

Figure 5.6: Flux-surfaces of the Island-2 configuration vacuum field at three cross-sections in ϕ.

configuration but larger. The magnetic hill is also higher and the difference in elongation between $\phi = 0$ and $\phi = \pi/3$ cross sections further accentuated. Vacuum flux surfaces of this configuration are shown in Fig. 5.7

- Near-Island-1: Starting from the first island configuration the helical current is adjusted to -16.6kA so that the rotational transform is always above $\iota = 1.2$ and no island is present. This small change to the helical current is just enough to remove the rational surface from the plasma region but has minimal effect on the magnetic shear or any of the other configuration parameters. Differences between the equilibrium found for this configuration and that of the first island configuration will allow me to determine the effect of the island on other equilibrium features and to separate different influences on island size. The vacuum flux surfaces of this configuration (shown in Fig. 5.8) are very similar to those of the Island-1 configuration except for the small rise in average ellipticity associated with the rise in rotational transform.

- Near-Island-2: This configuration is identical to Island-2 except for a change in helical current to -17.2kA which removes the $\iota = 1.2$ rational surface from the plasma. The comparison of this configuration with the Island-2 configuration will allow me to confirm conclusions drawn from the comparison of Island-1 and Near-Island-1 results. Vacuum flux surfaces of this configuration are shown in Fig. 5.9

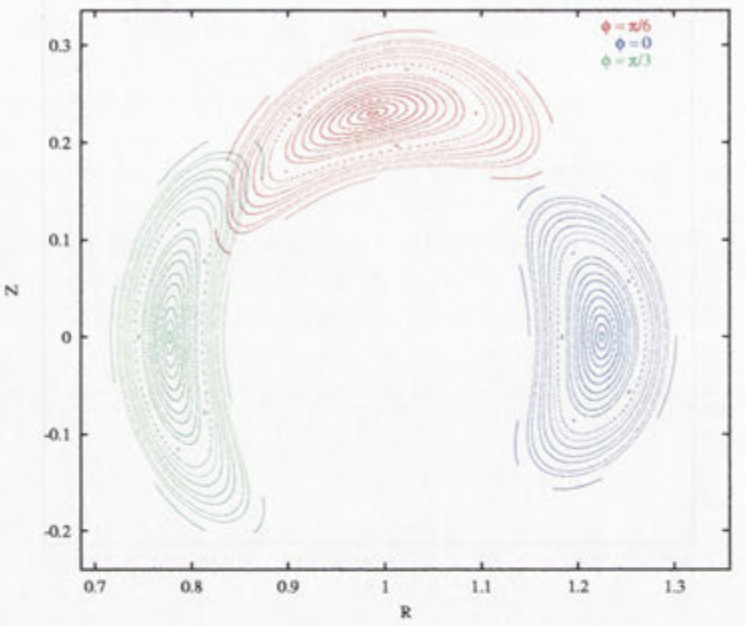

Figure 5.7: Flux-surfaces of the Island-3 configuration vacuum field at three cross-sections in ϕ.

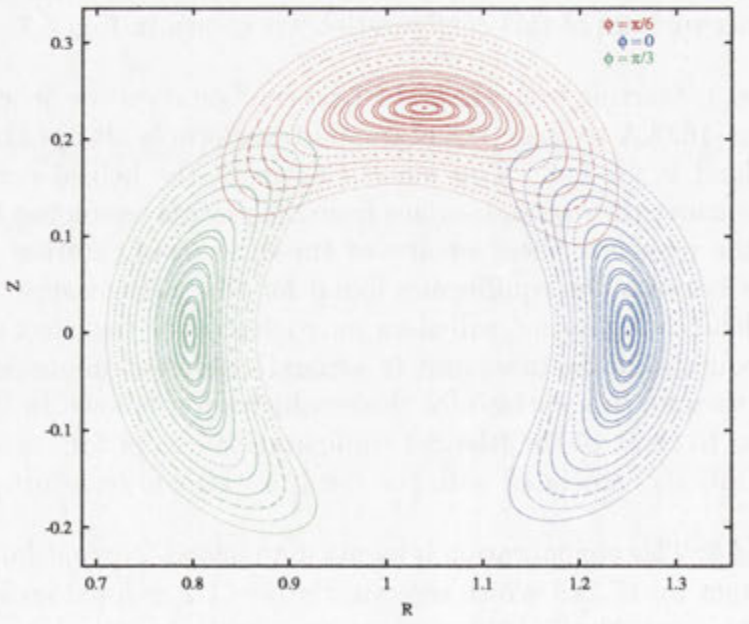

Figure 5.8: Flux-surfaces of the Near-Island-1 configuration vacuum field at three cross-sections in ϕ.

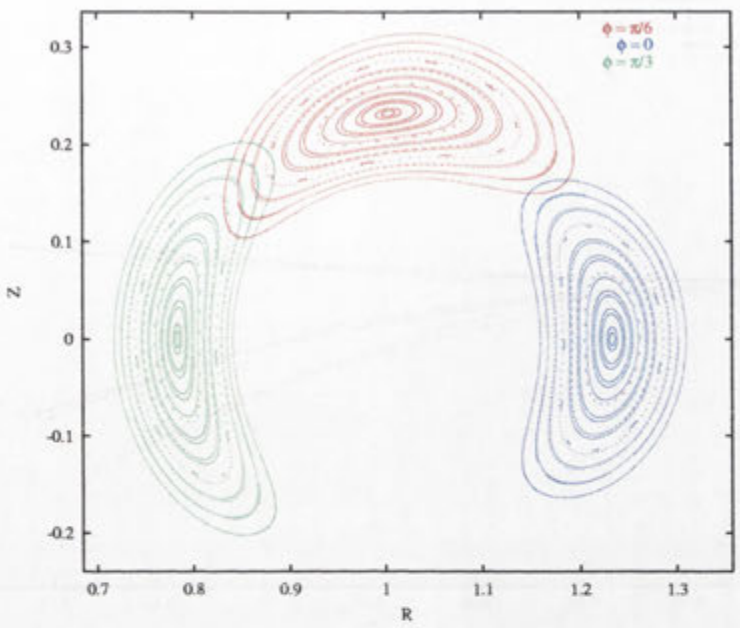

Figure 5.9: Flux-surfaces of the Near-Island-2 configuration vacuum field at three cross-sections in ϕ.

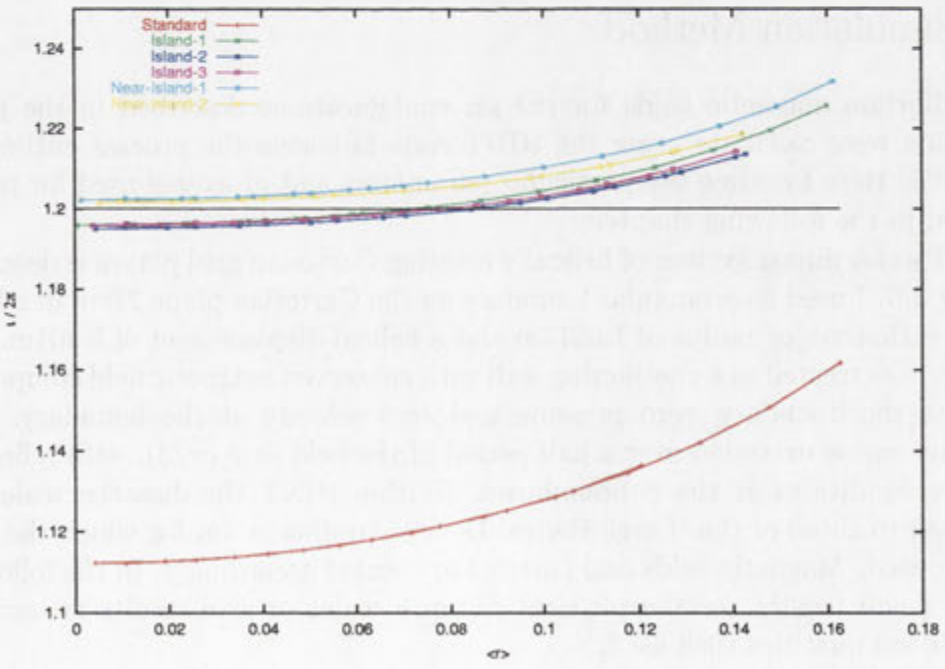

Figure 5.10: Comparison of the vacuum rotational transform profiles for the different configurations

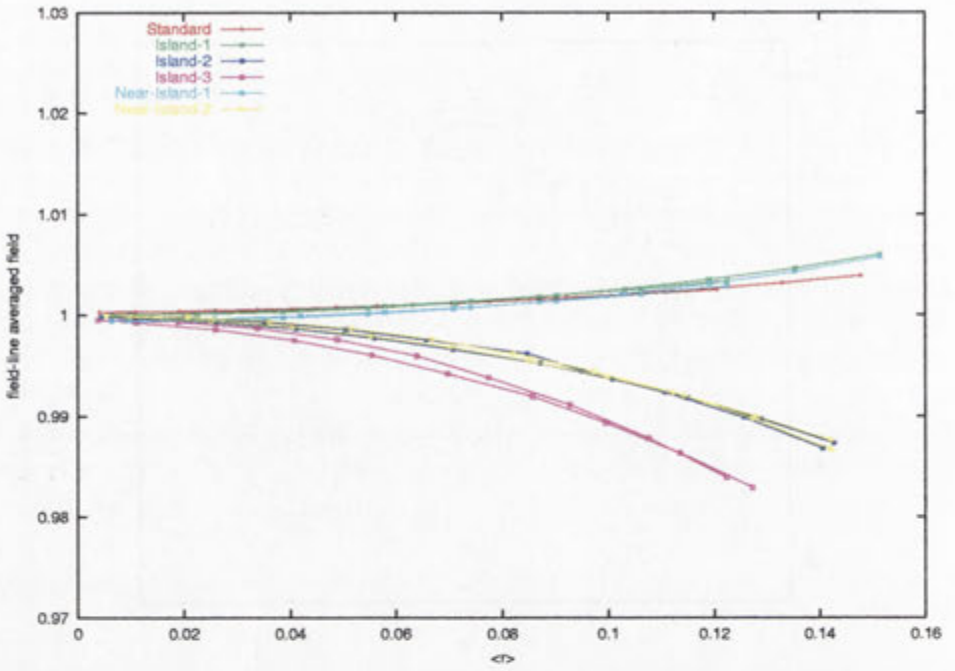

Figure 5.11: Comparison of magnetic wells for the different configurations

5.3 Simulation Method

Equilibrium magnetic fields for the six configurations described in the previous section were calculate using the HINT code following the process outlined in Chapt. 3.5. Here I outline the particular parameters and processes used for results presented in the following chapters.

HINT's coordinate system of helically rotating Cartesian grid planes is described in Chapt 3.6. I used a rectangular boundary on the Cartesian plane 27cm in x by 48 cm in y with a major radius of 1.0213m and a helical displacement of 0.201m. The boundary was treated as a conducting wall with conserved magnetic field component normal to the boundary, zero pressure and zero velocity at the boundary. The simulation region extended over a half period of the field in ϕ ($\pi/3$), with reflection boundary conditions at the ϕ boundaries. Within HINT the distance scales are normalised to those of the 'Large Helical Device' (radius $\approx$ 4m for which the code was optimised. Magnetic fields and currents are scaled accordingly. In the following chapters I will mostly use the physical distance scales or give results in terms of dimensionless quatities such as β.

This boundary was very close to the helical current and had problems with stability using the original field relaxation which were solved by using a modified field relaxation (Hayashi *et al.* (2000)) to deal with the high Alfvén speeds in this region. Previous calculations of H1-NF equilibria with HINT (Hayashi *et al.* (1995), Lloyd *et al.* (1997)) used an inset boundary to avoid the helical current winding.

The simulation region was covered by a $(73 \times 73 \times 37)$ grid with grid spacings of $\Delta y = 6.67mm$, $\Delta x = 3.75mm$, $\Delta\phi = \pi/108$.

A vacuum field is calculated on the grid from the H-1NF coil currents using exact equations for field at (z, r) from loop radius a carrying a current I:

$$B_r = \frac{\mu I z k}{4\pi a r}(\frac{a}{r})^{1/2}(-K(k) + \frac{2-k^2}{2-2k^2}E(k))$$
$$B_z = \frac{\mu I k}{4\pi a}(\frac{a}{r})^{1/2}(-K(k) + \frac{k^2(a+r)-2r}{2(1-k^2)r}E(k))$$

where $k^2 = 4ar/((a+r)^2+z^2)$ and the elliptic integrals $K(k) = \int_0^{\pi/2}(1-k^2\sin^2\theta)^{-1/2}d\theta$ and $E(k) = \int_0^{\pi/2}(1-k^2\sin^2\theta)^{+1/2}d\theta$ are approximated by up to 24 terms of their series expansions depending on the value of k. The helical winding is treated as a closed polygon and its contribution to the vacuum field is calculated from Biot-Savart's law.

The initial pressure profile is specified as a function of vacuum flux as $p(\psi) = p_0(1-(\psi/\psi_E))^2$, with $<\beta> \approx 0.015\%$. Pressure is initially increased by a factor of 7 over 5 steps in alternation with the field and pressure relaxation steps, followed by five relaxation steps without pressure increase. After this pressure is increased more gradually, by a factor of 2 over each 5 steps followed by five relaxation steps without pressure increase. For $<\beta> > 1\%$ even smaller increases in pressure were used. Most of the results presented in the following chapters have had at least 20 steps of alternate field and pressure relaxation steps at the final peak pressure.

My new method, PR3s, was used for the pressure relaxation step using an initial set of 365 field lines traced for 750 half-field-periods and 27 steps of field-line tracing with PR2 for smoothing.

A resistivity of $\eta = .01$ and time step of $\Delta = .00375$ were used within the field relaxation step described in Chapt. 3.7. Each iteration of the field relaxation involved 1000 time steps.

5.4 Measuring D_R and $\mathcal{J}_{mn}/\mathcal{J}_{00}$

To measure the resistive Mercier criteria, D_R, and the resonant harmonics of the Jacobian, $\mathcal{J}$, I calculated equilibria with VMEC (Hirshman *et al.* (1986)) that matched the HINT equilibria in vacuum field, pressure profile and average beta. I then calculated the resistive Mercier stability criteria of the VMEC equilibria using the JMC code (Nührenberg & Zille (1984)). D_R was scaled to match that used by Glasser *et al.* (1975). This scaling applied to the ideal Mercier criteria gives a shear term scaled to 1/4.

VMEC calculates the vacuum magnetic field from the shape of the last closed flux surface. The harmonics of this surface were obtained from a field-line trace in HINT translated into harmonic components by the DESCUR code (Hirshman & Meier (1985)). This vacuum field calculation is not perfect, with a small discrepancy in the near-axis rotational transform for the vacuum field. The VMEC version was fixed boundary (last closed flux surface is not allowed to change shape) while HINT

is closer to a free boundary condition. To match the VMEC equilibria to the HINT equilibria, a calculation of the last flux surface from the HINT equilibria at a given β was used for the VMEC run at that β. The last closed flux surface in VMEC was taken from the last non-zero pressure surface of the HINT equilibrium. Both simulation codes take the pressure profile as an input parameter but HINT may have drifted slightly (especially near the plasma boundary).

In JMC, D_R can be calculated by two methods: Direct and Indirect (Ichiguchi *et al.* (1996)). The Indirect is effected by the singular resonant currents at rational surfaces and gives peaks of unstable D_R at the rational surface. The Direct method does not show these effects (Ichiguchi *et al.* (1996)). The resonant components of the Pfirsch-Schlüter currents are not included in the calculation of D_R used in the analytic island calculations so the Direct method gives a value of D_R more suitable for calculating the interchange terms for the island equation. I use the Direct method calculation of D_R, except at very low β where errors due to the minute size of the currents involved seem to make it much less accurate than the Indirect method.

CHAPTER 6

HINT Results - General Equilibrium Characteristics

In this chapter I present some of the characteristics of the equilibria calculated with HINT for the six configurations of the H-1NF Heliac described in the previous chapter. The response of some of these characteristics to increases in pressure can be predicted by simple analytic models. Many of the characteristics presented here had the same response to pressure increases in each configuration, in which case the results of only one configuration are shown.

Section 6.1 calculates the helical and toroidal magnetic axis drifts and derives a rough β limit from these. Section 6.2 describes the changes to the flux surface shape in terms of ellipticity and indentation measures. Section 6.3 shows that the deepening of the magnetic well depth as pressure increases can be attributed to plasma diamagnetism. Section 6.4 discusses the rise of rotational transform at the magnetic axis in response to pressure increase. Section 6.5 describes the perpendicular currents needed for force balance and their associated parallel currents. Section 6.6 shows the shape of the plasma velocity distribution. Results involving magnetic island growth will be discussed in the next chapter.

6.1 Magnetic Axis Drift

The magnetic axis rotates approximately helically around the main coil. The average major radius and helical deviation of the magnetic axis depend on the particular configuration of the vacuum field. The helical deviation and the major radius of the magnetic axis increased when plasma pressure was increased. For $<\beta> < 1\%$ the magnetic axis drifts were nearly linear with pressure and consistent across the different configurations despite different vacuum positions (see the top two plots of Fig. 6.1). The increase in major radius (the toroidal drift) was about 1–1.2cm for every 1% increase in $<\beta>$ while the helical deviation (the helical drift) increased at about .4cm for every 1% increase in $<\beta>$.

At the $\phi = 0$ plane the plasma is outside the main coil and the helical and toroidal drifts add together, giving an overall outward drift of the magnetic axis position, at a rate of about 1.6cm for every 1% increase in $<\beta>$. At the $\phi = \pi/3$ plane, with the plasma inside the main coil, the helical and toroidal drifts push the

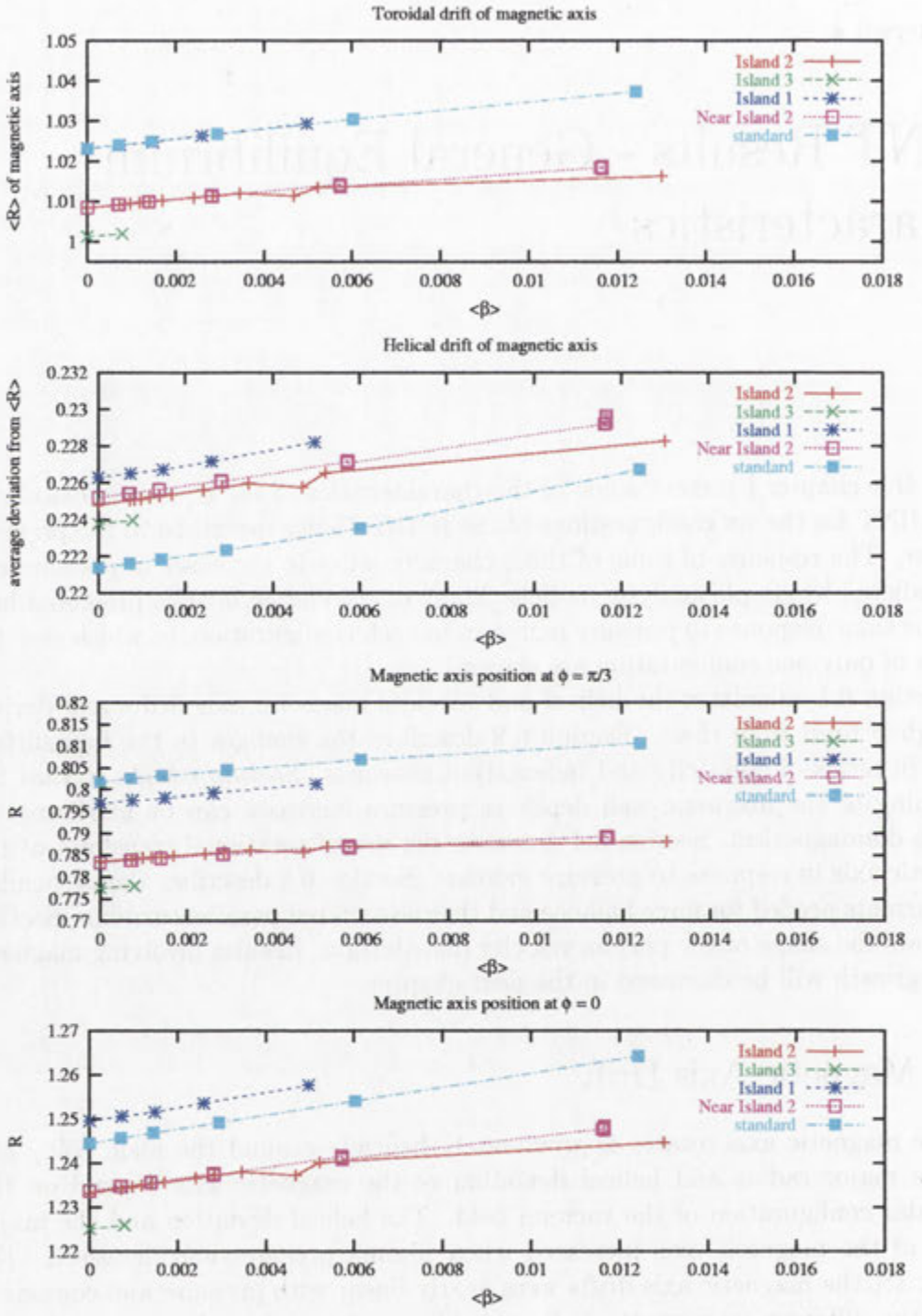

Figure 6.1: Magnetic axis position drifts outward toroidally and helically with increasing β at a similar rate for all configurations tested. On the inner side of the main coil the helical drift partially counteracts the outer drift to give only a small movement (of increasing the major radius) of the magnetic axis. On the outer side of the main coil the helical and toroidal drifts add giving a larger outward movement in major radius

magnetic axis in opposite directions so the magnetic axis drift is much smaller on this plane. The toroidal drift is larger than the helical drift, and the magnetic axis on this plane drifts towards the main coil at 0.5–0.9cm for each 1% increase in $<\beta>$.

Magnetic axis drift gives one limit to the maximum $<\beta>$ that can be confined by a stellarator. As the magnetic axis moves towards the walls of the vacuum chamber (or any other obstacle inside the chamber), the outer flux surfaces come into contact with the wall and they can no longer confine any plasma. This maximum $<\beta>$ limit is generally calculated from the β required to move the axis half way to the boundary. For the magnetic axis drift of the $\phi = 0$ plane (and taking the boundary as the simulation boundary) the maximum $<\beta>$ limit is about 3.5%. The magnetic axis drift at the $\phi = \pi/3$ plane is smaller and it does not impose as severe a restriction on the maximum $<\beta>$.

Moving the magnetic axis outwards changes the effective vacuum field seen by these surfaces. This will affect the magnetic well depth and may also affect the elongation and indentation of the magnetic surfaces and the rotational transform profile.

6.2 Flux surface elongation and indentation

The elongations of the vacuum flux surfaces of the six H1-NF configurations (shown in Fig.5.3) differed significantly, although all showed greater elongation near the magnetic axis than at the boundary and more elongation on the $\phi = \pi/3$ cross-section than on the $\phi = 0$ cross-section. There was a consistent trend in changes to flux surface shape as β was increased, for all of the six configurations. As β increases, the elongation of the $\phi = 0$ cross-section decreases near the magnetic axis but the elongation of the $\phi = \pi/3$ cross-section at the magnetic axis increases. The contrast between the shape of the flux surfaces at $\phi = \pi/3$ and at $\phi = 0$ increases as β increases. The elongation of the outer flux surfaces is not significantly altered by changes in plasma pressure. This led to flux surfaces in at $\phi = 0$ having a peak in elongation midway between the axis and the outer surface. Changes in the elongation profile with β for the Standard configuration are shown in Fig. 6.2.

The elongation near the axis changed approximately linear with β and the rate of change was similar for the different configurations (see Fig. 6.3). The increase in elongation of magnetic surfaces in the $\phi = \pi/3$ cross-section was larger than the decrease in elongation of the surfaces in the $\phi = 0$ cross-section giving an increase in the average elongation of the flux surfaces near the magnetic axis. The increase in average elongation was associated with an increase in the rotational transform on axis (according to the equations discussed in Chapt. 5.1).

The indentation of flux surfaces at the $\phi = 0$ cross-section changed very little with increasing pressure (see Fig. 6.4). However, surfaces at the $\phi = \pi/3$ cross-section became more indented. This could be related to the increasing elongation of these surfaces with the same amount of indentation in x becoming a larger proportion of the flux surface range in x.

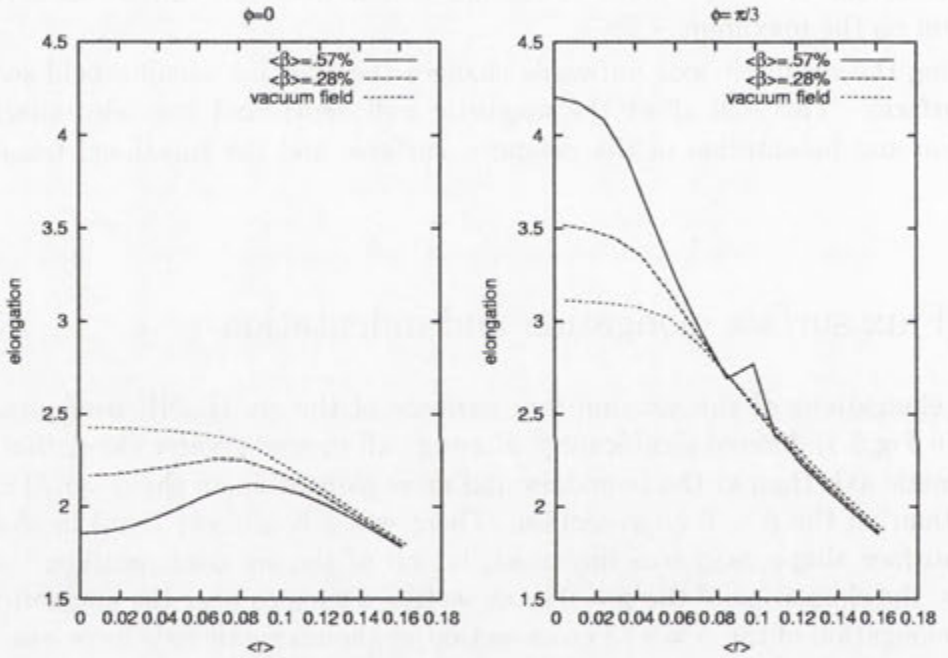

Figure 6.2: Radial profile of elongation for the Standard configuration at three different β. The kink in elongation at $< r >= 0.1$ for $<\beta> = 0.57\%$ is due to the measurement being taken inside a magnetic island, which has grown to a significant size by this $<\beta>$.

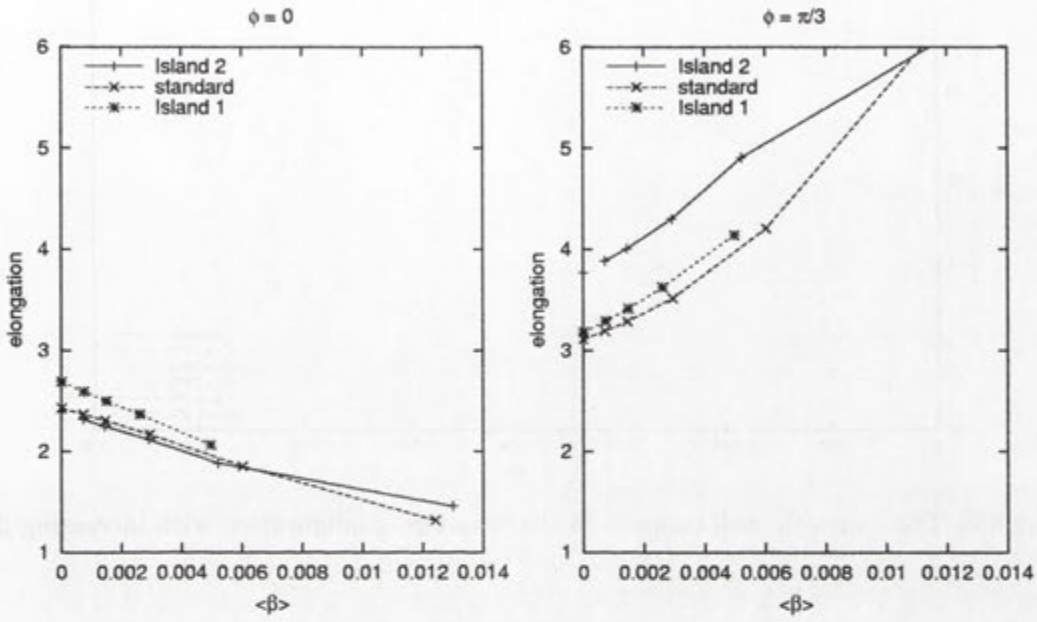

Figure 6.3: Changes in elongation of magnetic flux surfaces near the magnetic axis with increasing pressure.

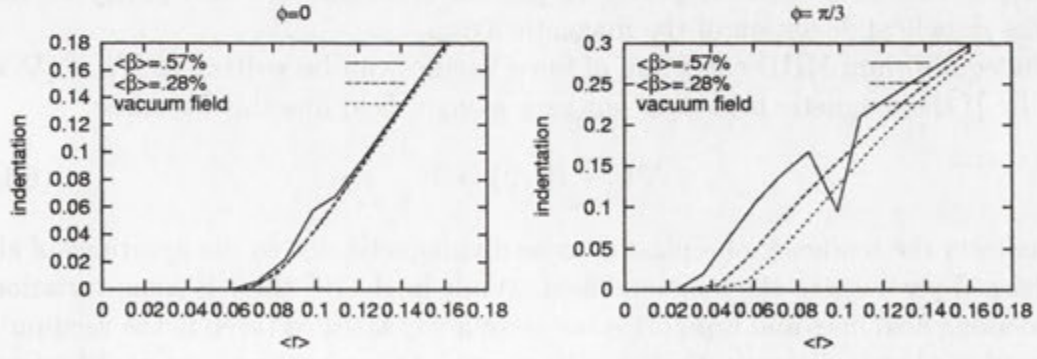

Figure 6.4: Radial profile of indentation for the Standard configuration at three different β. The kink in indentation at $< r >= 0.1$ for $<\beta> = 0.57\%$ is due to the measurement being taken on a field line inside an island.

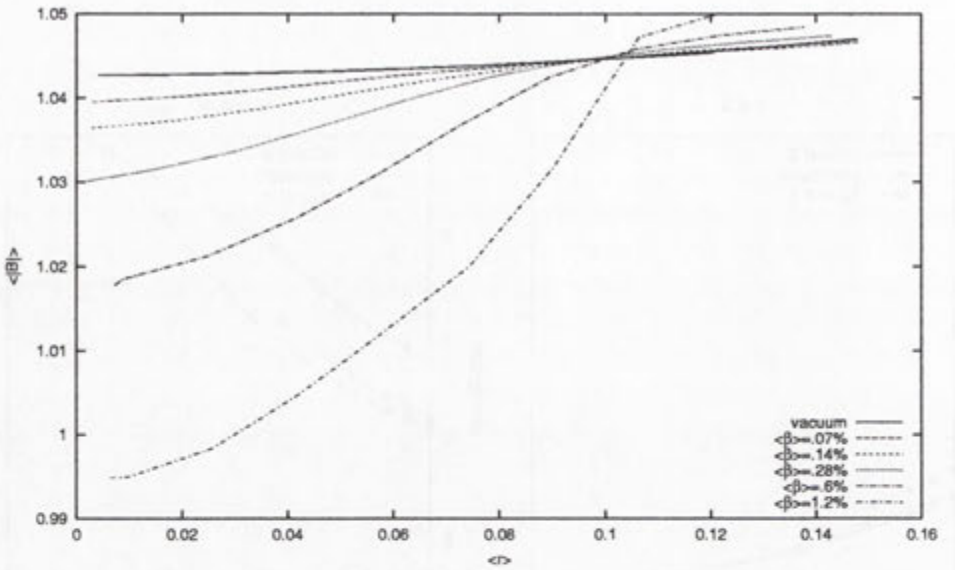

Figure 6.5: The magnetic well deepens in the Standard configuration with increasing β

6.3 Magnetic well depth

The magnetic well depth in all configurations of H-1NF deepened as plasma pressure was increased. The vacuum magnetic well or hill is insignificant compared with the equilibrium magnetic well at $<\beta> = .5\%$. Changes to the magnetic well with changes in β are shown in Fig. 6.5 for the Standard configuration and the results for other configurations were very similar to this. The increasing magnetic well depth can be attributed partly to plasma diamagnetism and partly to the increase in helical deviation of the magnetic axis.

The equilibrium MHD condition of force balance can be written as $\nabla p = (\nabla \times B) \times B$. If the magnetic field does not vary along a field line this becomes:

$$\nabla(p + B^2/2) = 0 \tag{6.1}$$

This reflects the tendency of a plasma to be diamagnetic due to the gyrations of all the charged particles in the magnetic field. While in H-1NF there is some variation in field along field lines and Eqn. 6.1 is not completely satisfied (even in the vacuum), the trend of plasma diamagnetism is still present. At low pressures its modification to $p + B^2/2 = B_{\text{vac}}^2/2$ is reasonably accurate for H-1NF. This is demonstrated in Fig. 6.6 for the Standard configuration at $<\beta> = .28\%$.

Plasma diamagnetism causes a deepening of the magnetic well with increasing β. Rearranging the above equation gives $B/B_{\text{vac}} = \sqrt{1 - \beta(r)}$. At low β if the vacuum magnetic well was small the change in magnetic well due to plasma diamagnetism will equal the peak β (β on the magnetic axis). This would predict about 3.6% well depth at $<\beta> = 1.2\%$. The measured magnetic well depth at this $<\beta>$ is about 5%.

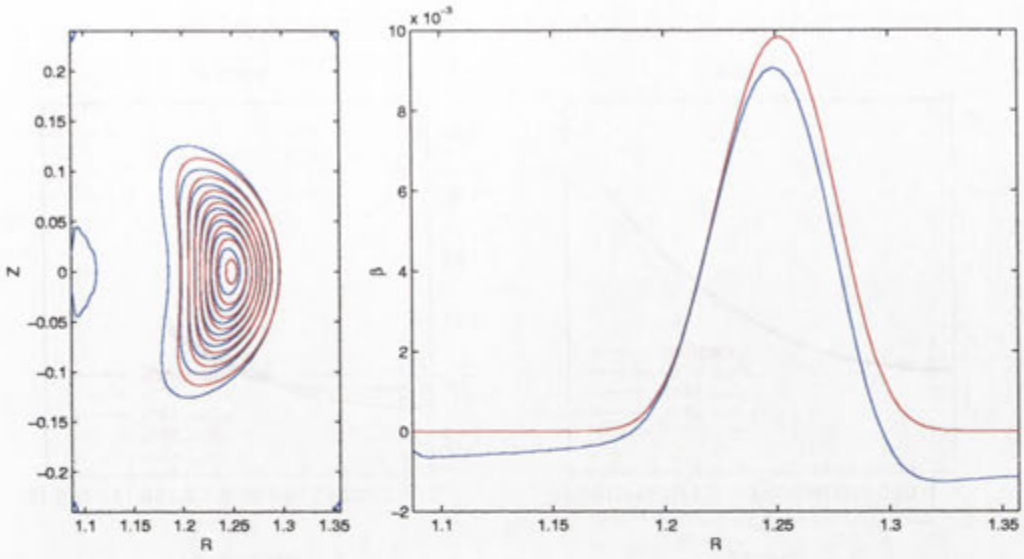

Figure 6.6: The plot to the left compares contours of $B^2_{\text{vac}} - B^2$ (blue) with pressure contours (red). The plot to the left is a transect of the previous plot at Z=0 and shows that $(B^2_{\text{vac}} - B^2)/B^2$ (blue) is well approximated by $\beta = 2p/B^2$

(red).

The remaining increase in magnetic well depth must be due to changes in the shape and position of magnetic surfaces. The major contribution to this comes from the helical magnetic axis drift moving the magnetic axis away from the main poloidal field coil towards a region of lower field strength. The outer magnetic surfaces are restrained from moving by the conducting boundary. Thus the inner magnetic surfaces reduce their average field strength while the outer surfaces maintain their higher field strength, and the magnetic well depth is increased.

6.4 Rotational transform profile

The six vacuum configurations had different values of rotational transform near the magnetic axis but the overall shape of the rotational transform profile was similar, with a flat profile near the axis and an increase in rotational transform towards the plasma boundary. As plasma pressure increased ι rose on and around the magnetic axis but maintained near vacuum values at the plasma edge. This trend was consistent across the configurations although the amount of rise on axis (and the behaviour of ι at intermediate surfaces differed between configurations. The rotational transform profiles for all the configurations are shown in Fig. 6.7

The rise in ι near the axis lead to a magnetic shear reversal within the central plasma region and a turning point in ι between this region and the normal shear region at the plasma edge. Reversed shear appeared at $<\beta> \approx .2\%$ and the turning

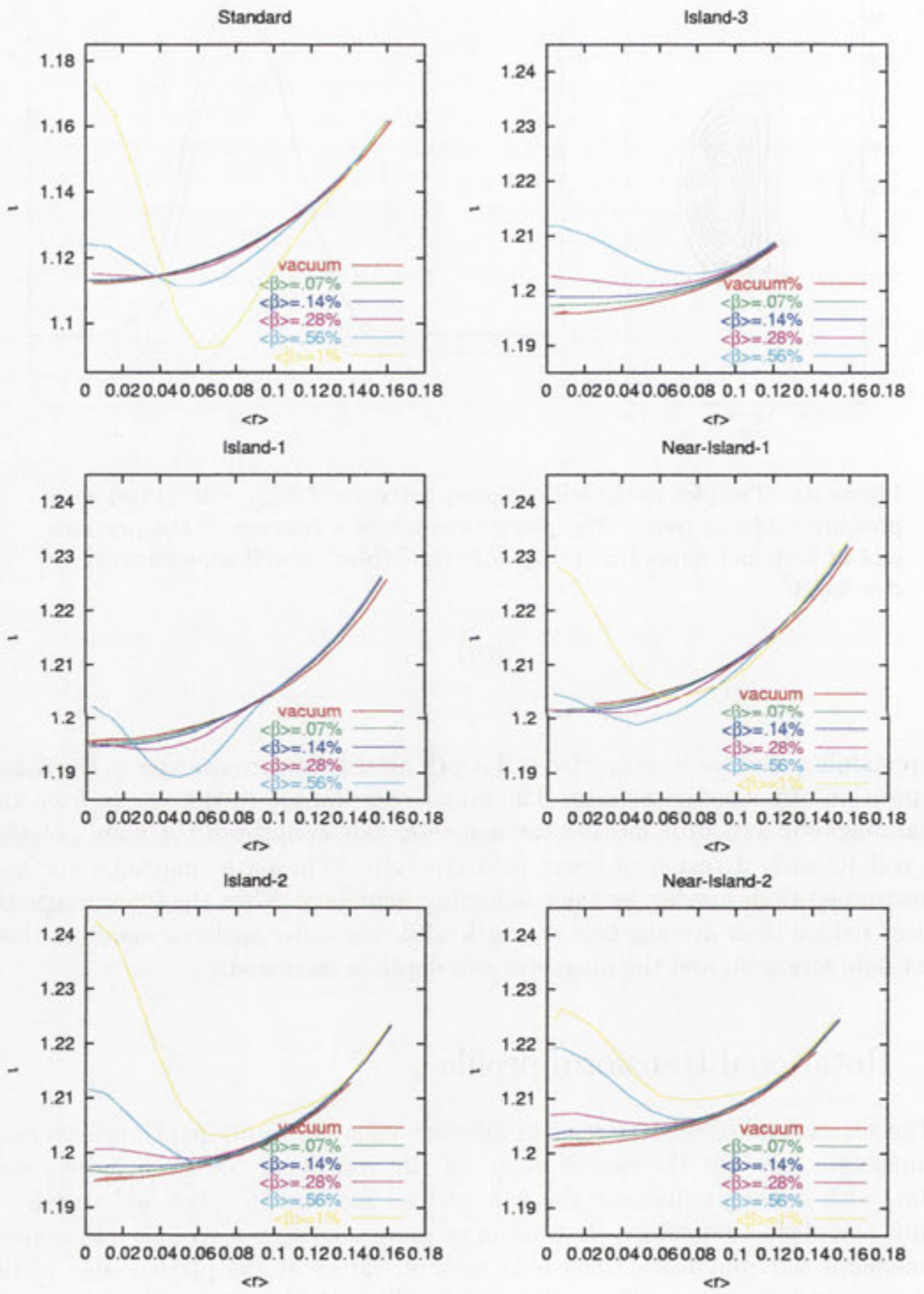

Figure 6.7: Plots show rotational transform profile changes with β for each of the H1-NF configurations

point in ι moved outward as pressure was increased.

Some insight into the change in ι by considering the results of the previous section which showed that the field strength changed with pressure according to $B/B_{vac} = \sqrt{1-\beta}$. If all of the decrease in magnetic field strength was due to decreasing the toroidal field component with no change to the poloidal field component (i.e. the plasma current is entirely poloidal) we would expect a the rotational transform profile to change as:

$$\iota(\psi) = \iota_{vac}(\psi)(1/\sqrt{(1-2p(\psi)/B^2_{zvac}}\ , \tag{6.2}$$

. At low β this reduces to

$$\iota(\psi) = \iota_{vac}(\psi)(1+\beta(\psi)/2)\ . \tag{6.3}$$

This relationship matches the rotational transform changes quite well, at very low β, for the Island-2, Near-Island-2 and Island-3 configurations. However it significantly underestimates the rise in rotational transform at higher β and does not give an explanation for the decreasing rotational transform, on surfaces midway between the axis and the edge, for the Standard, Island-1 and Near-Island-1 configurations. Changes to the poloidal component of the magnetic field (from toroidal current components) and changes to the positions of the magnetic surfaces will also affect the rotational transform profile.

The phenomena of rising rotational transform on axis with increasing β is a common feature of numerical calculations of stellarator equilibria (Harafuji *et al.* (1989),Hayashi *et al.* (1990),Gardner (1986),Hayashi *et al.* (1995),Hirshman *et al.* (1986). It is not restricted to heliacs or to any particular form of numerical simulation. The rise of rotational transform on axis is often accompanied by some decrease in rotational transform away from the magnetic axis and with minimal variation at the plasma edge. However the trend is not universal, configurations have been found for which the rotational transform decreased at the magnetic axis as beta was increased(Hayashi *et al.* (1994),Hayashi *et al.* (1990)).

I found the rotational transform profile, particularly near the magnetic axis, to be one of the most sensitive features of the equilibrium to pressure increase. This is partially due to the small shear so that small changes in rotational transform can make a large difference to the shape of the rotational transform and the placement of rational surfaces within the plasma. Rotational transform was also one of the slowest equilibrium features to reach a stable value. The slow convergence of rotational transform may be related to slow convergence in the net parallel current.

6.5 Plasma current distribution

In these HINT calculations the largest components of the plasma currents were perpendicular to the field lines but still confined to the magnetic surfaces. The perpendicular current flow is shown in Fig. 6.8 for the Standard configuration at $<\beta>$ = .28%. The features of this current flow do not change much with small

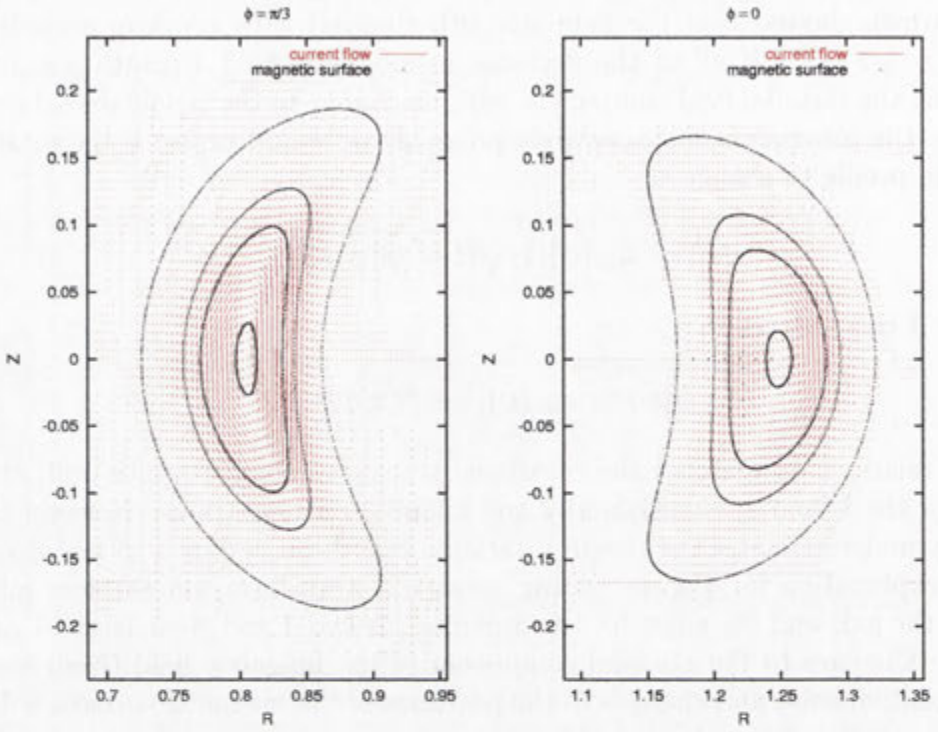

Figure 6.8: Red lines from each grid point show the relative magnitude and direction of the plasma current within the ϕ plane. Results shown are for the Standard configuration at $<\beta> = .28\%$ but the main features of the plot do not change significantly with changes to configuration or pressure.

increases in β or across the different configurations. The current increases proportionally with pressure for these relatively low β simulations. The current is concentrated on magnetic surfaces with the highest pressure gradients across them. These occur at about half the plasma radius.

Because the flux surfaces are not circular, the pressure gradient is not uniform over a flux surface. More perpendicular current is needed on the inner and outer sections of a flux surface than on the upper and lower sections. This does not disturb $\nabla \cdot \mathbf{J} = 0$ as it exactly matches the current between flux surfaces spreading out to cover the larger spacing between flux surfaces.

Some parallel current is needed to counter the variation in field strength across the flux surfaces. The field strength is highest near the main coil, and varies in x but very little in y (shown in Fig. 6.9). Thus, the parallel current is dominated by a positive parallel current between the magnetic axis and the main coil and a negative parallel current from the magnetic axis outward in R (see Fig. 6.10). Parallel current is concentrated at the region of highest pressure gradient and also near the $Z = 0$ line. The stellarator condition (naturally arrived at with a resistive equilibrium)

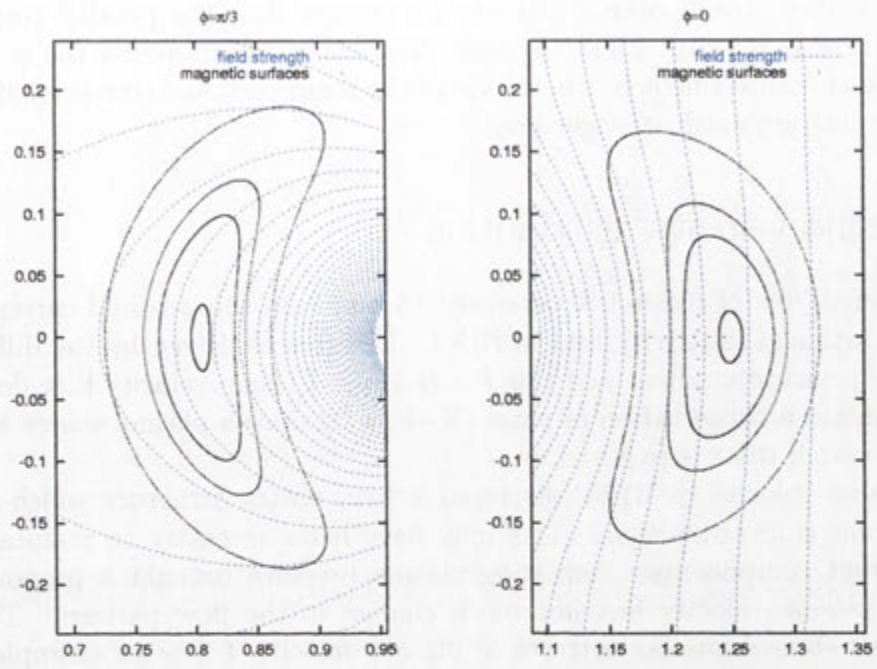

Figure 6.9: Contours of the field strength for the Standard configuration at $<\beta> = .28\%$

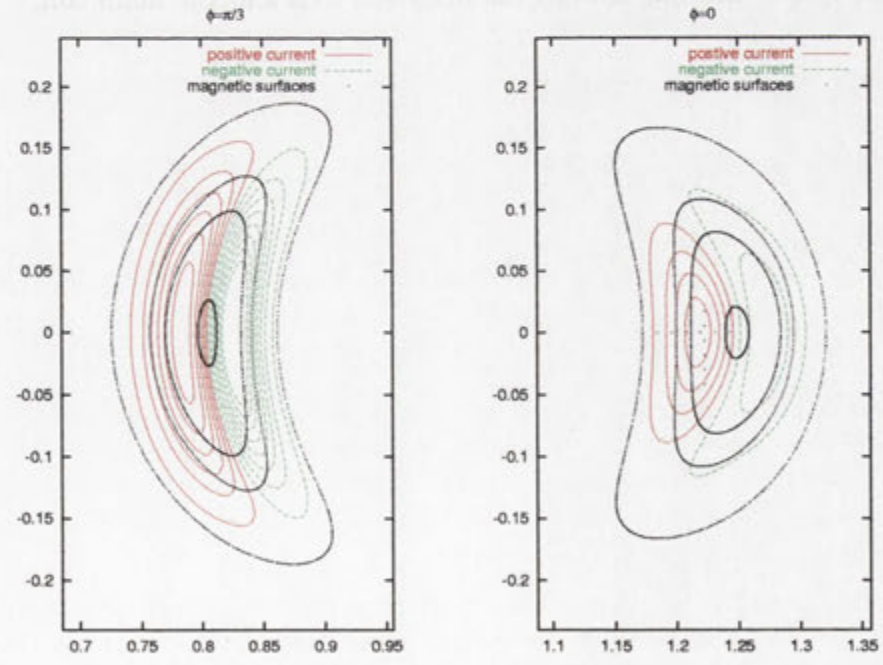

Figure 6.10: Contours of the parallel current for the Standard configuration at $<\beta> = .28\%$

of no net parallel current over a flux surface ensures that the parallel current at the magnetic axis is zero. Field strength varies much more across the $\phi = \pi/3$ cross-section (because this is on the inside of the main coil) and, consequently, the parallel currents are much stronger here.

6.6 Plasma velocity distribution

An outward flow of plasma is necessary to maintain the poloidal current flow against the artificial resistivity ised in HINT. This flow is driven by the difference between the pressure gradient and the $J \times B$ force. Plasma velocity flow does not need to maintain a conservation of mass ($\nabla \cdot V = 0$) since a plasma source term is assumed to match what is required.

The plasma velocity in HINT displayed a twin vortex structure which varied across different ϕ cross-sections. This may have been necessary to maintain the parallel current components. Increasing plasma pressure brought a proportional increase in plasma velocity but not much change in the flow pattern. The six configurations showed similar patterns of plasma velocity, I give an example from the Standard configuration in Fig. 6.11. On the $\phi = 0$ cross section the main outward flow was along the $Z = 0$ mid-line from the magnetic axis toward increasing major radius. On the $\phi = \pi/3$ cross-section the major outward plasma flow is along the least gradient ridge lines. Much of the plasma flows back along the magnetic surfaces on the side of the plasma away from the central coil. and there is an inward flow along the $Z = 0$ mid-line toward the magnetic axis and the main coil.

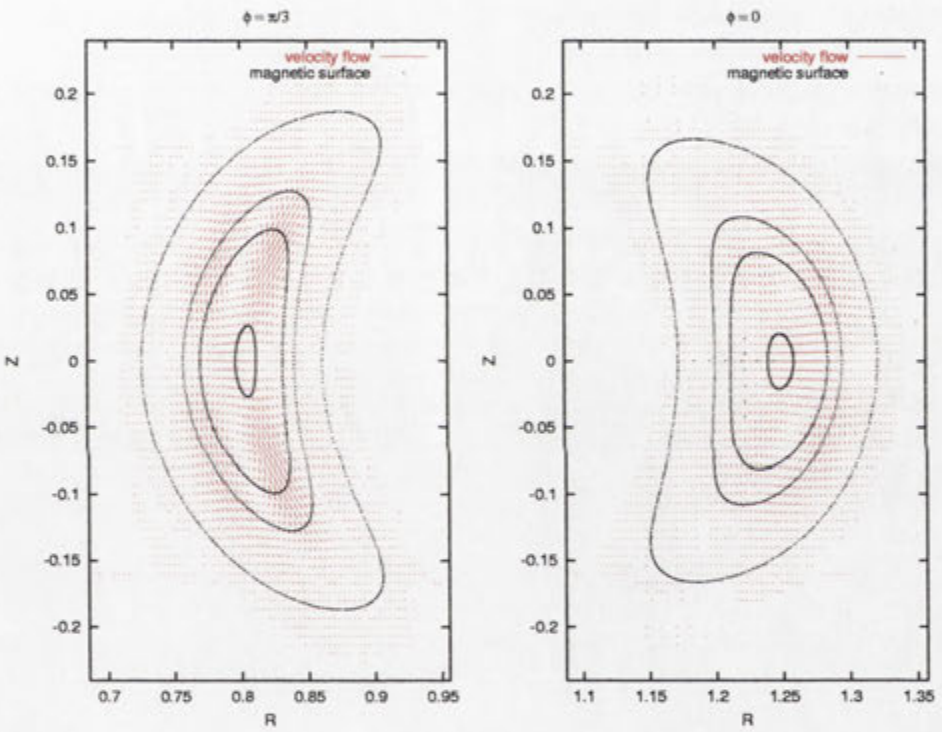

Figure 6.11: Red lines from each grid point show the relative magnitude and direction of the plasma velocity within the ϕ plane. Results shown are for the Standard configuration at $<\beta> = .28\%$ but the main features of the plot do not change significantly with changes to configuration or pressure.

CHAPTER 7

HINT Results - Island Growth

In this chapter, I examine the response of islands to pressure within the HINT simulations for the different configurations of Chapt. 5. The first three sections take a qualitative look at topological changes to islands in the simulated equilibrium magnetic fields. Poincaré sections are used to show the topology of the new flux surfaces near rational values of rotational transform.

In the Sect. 1, whether islands grow, shrink or change phase is determined for each configuration. I discuss how well this fits with the expectations of the theory introduced in Chapt. 2. Section 2 examines development of stochastic field lines at high beta. The beta at which stochasticity develops in different configurations is examined in terms of island theory. A maximum beta confinement limit due to breakdown of magnetic surfaces is suggested.

Other interesting flux surface topologies were also found in the HINT simulations and these are shown in Sect. 3. Some insight is gained by comparing them to the more unusual topologies modelled earlier with simple maps.

Section 4 shows the effect of changes in flux surface topology and island size on pressure and current distributions. Pressure flattening within islands, current exclusion from within the island and the deviation of current to follow the new flux surfaces are all modelled within the resolution of the HINT simulation.

In the fifth section I compare the island equilibria with their nearby non-island equilibria. The resonant currents are very different without the rational surface but the non-resonant currents should be little affected. Using the plasma currents from the near-island equilibria with the corresponding island configuration vacuum field gives an idea of the relative importance of resonant currents. The island sizes at low beta were surprisingly similar, implying that non-resonant currents make the dominant contribution.

In the sixth section I give the results of resistive stability criteria calculation for the HINT simulations. The results given here determine the relative importance of local island resonant currents and the linear global resonant currents on island growth or self-healing. In the seventh section I compare measurements of island size from the HINT simulations with predictions of island size for the theory of Bhattacharjee *et al.* (1995) using the stability criteria calculated in the previous section.

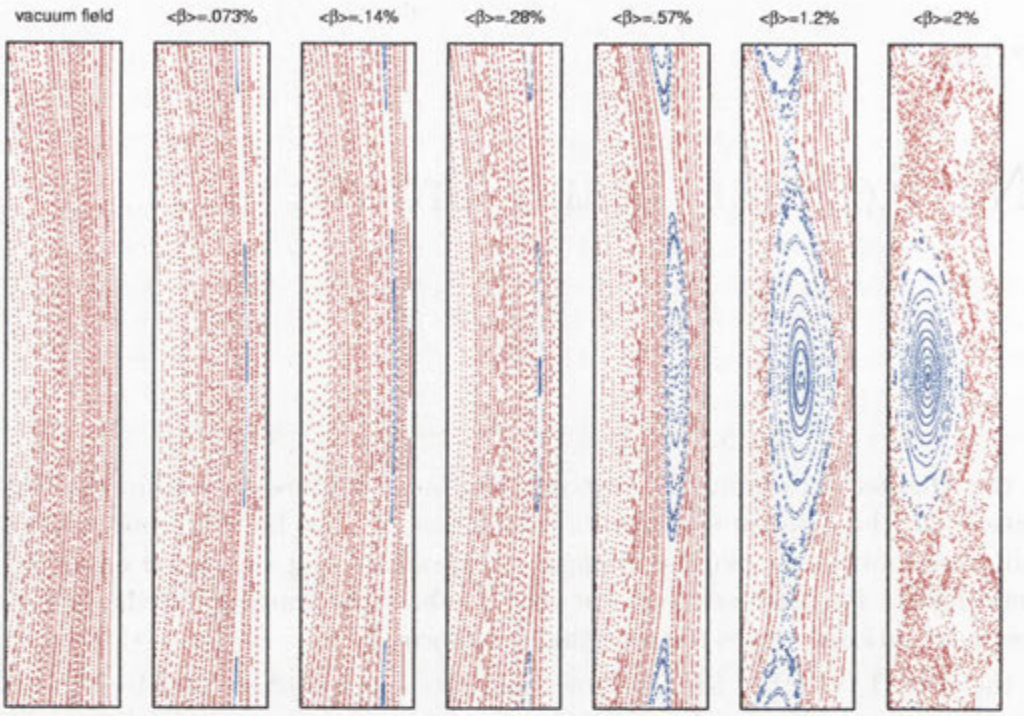

Figure 7.1: Detail of the Poincaré sections for the Standard configuration showing the growth of the 9/8 island with increasing $<\beta>$. The area shown is 10×60 mm (about 2.6×9 grid spacings) and is centered on $Z = 0$ between the poloidal field coil to the left and the magnetic axis to the right.

7.1 Island growth, shrinking and phase change

Four of the configurations I studied had low-order rational surfaces at which islands were observable in the field line traces (or became observable as the pressure was increased in the simulations).

Figures in this section are details of the $\phi = 0$ Poincaré sections showing the magnetic island centered on $Z = 0$. The magnetic axis is to the right of the pictures, with the poloidal field coil to the left. All the figures have the same spatial scale to allow comparisons of island size between configurations. A smaller range of β is used where self healing is shown to capture the details of a rapid change in island size or topology.

In the Standard configuration, the lowest order rational value of ι is 9/8 at about three quarters of the plasma radius, but the corresponding island is insignificant in the vacuum field. The island remained insignificant up to about $<\beta> = .3\%$. By $<\beta> = .6\%$ a chain of 8 islands developed at the rational surface, with O-points at the $Z = 0$ bisection of the $\phi = 0$ cross-section on both sides of the magnetic axis. At higher $<\beta>$ the island size increased quickly (See Fig. 7.1).

In the Island-1 configuration, the lowest order rational value of ι is 6/5 at about

half the plasma radius. A chain of five islands was visible around the rational surface in the vacuum field with an O-point at the outer side of the $\phi = 0$ cross-section and an X-point at the inner edge of this plane. The islands grew gradually with increasing β, as would be expected for a vacuum perturbation in phase with the field perturbation induced by the global plasma current. The growth of the 6/5 island in the Island-1 configuration is shown in Fig. 7.2. For $<\beta>$ between .5% and 2% the island in the Island-1 configuration is growing more slowly than the higher order island of the Standard configuration. By $<\beta> = 2\%$ the island widths in the two configurations are a similar size. This might be surprising because the island in the Island-1 configuration is lower order and has larger vacuum width than the island in the Standard configuration.

The growth rate of the island for the Island-1 configuration increases with pressure (see Fig. 7.1). This is also true for the Standard configuration. Comparing this with the growth patterns predicted from theory (Fig. 2.7) suggest a vacuum island in phase with the linear current perturbation with the influence of a *destabilising* non-linear term, $G > 0$. However both configurations have vacuum magnetic wells which deepen as pressure is increased which should give a *stabilising* non-linear term. This suggests that the non-linear stabilising currents predicted by theory are having little influence on the simulations for this configuration and that there may be some more influential global non-linear term not taken into account in the theory.

The Island-2 configuration also has a significant island chain at the $\iota = 6/5$ rational surface at about half the plasma radius. This island chain is of opposite phase to the island chain in the Island-1 configuration. It has an X-point on the outward side of the $\phi = 0$ cross-section and an O-point on the inner side. The island width stays approximately constant at low β but shrinks rapidly and changes phase at about $<\beta> = .2\%$ before growing fairly quickly in the opposite phase (see Fig. 7.3).

The theory of Bhattacharjee *et al.* (1995) gives this pattern of self-healing if the vacuum magnetic island is of opposite phase to the island induced by resonant global plasma currents, as long as the global currents dominate local island currents. The Island-2 configuration had a small magnetic hill which should give local island currents that reinforce the island perturbation and prevent complete self-healing of the island. The local island currents due to the magnetic hill do not seem to have made a large contribution to the island size. The result is qualitatively consistent with self-healing theory proposed by Bhattacharjee *et al.* (1995) but is not solid evidence in support of these theories.

This demonstration of self-healing in H-1NF simulations shows that we have succeeded in changing the phase of the resonant perturbation of the radial component of the vacuum field without changing the phase of the perturbations driving the linear plasma currents. The ability to selectively change the phase of the vacuum island, without effecting the phase of the field perturbations due to plasma currents, can be seen as a first step towards the use of external currents to counter the growth of islands with pressure.

Self-healing for this configuration occurs at very low β. This could be a useful

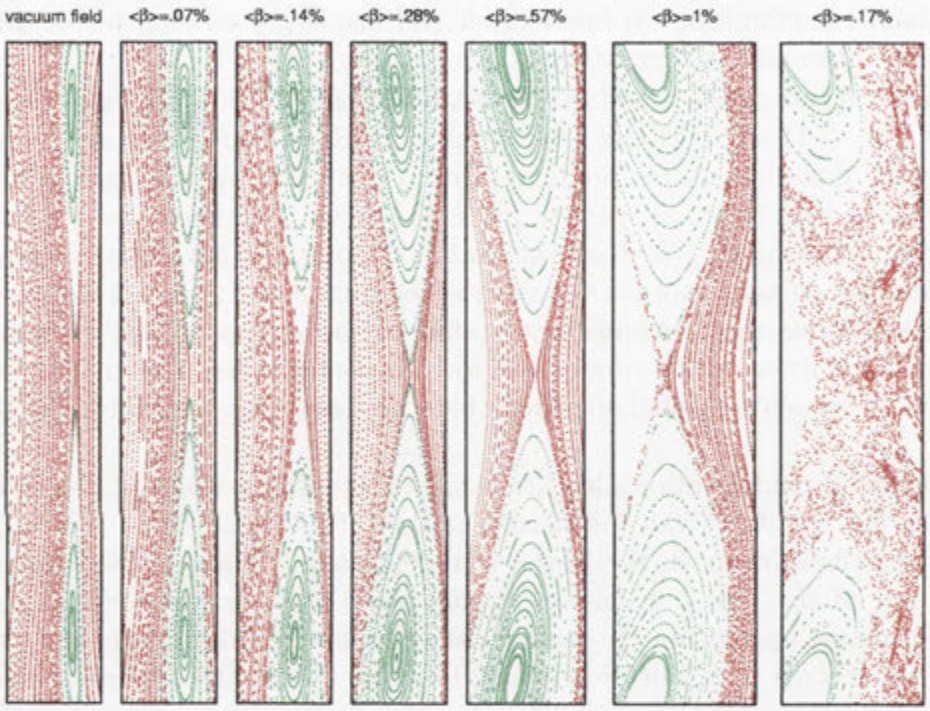

Figure 7.2: Detail of the Poincaré sections for the Island-1 configuration showing the growth of the 6/5 island with increasing $<\beta>$. The area shown for the vacuum field is 8×60 mm (about 2 *times* 9 grid spacings) and is centered on $Z = 0$ between the poloidal field coil to the left and the magnetic axis to the right. The horizontal range on the higher β plots has been increased to cover the growing island.

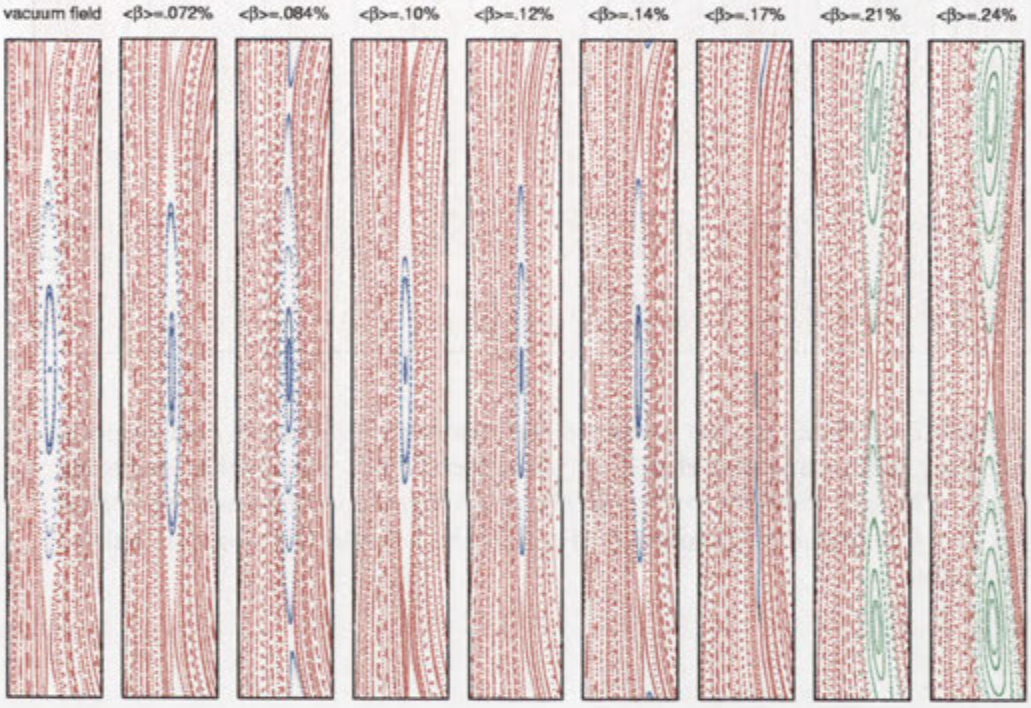

Figure 7.3: Detail of the Poincaré sections for the Island-2 configuration showing self-healing and change of phase for the 6/5 island with increasing $<\beta>$. The area shown is 8×60 mm (about 2 × 9 grid spacings) and is centered on $Z = 0$ between the poloidal field coil to the left and the magnetic axis to the right.

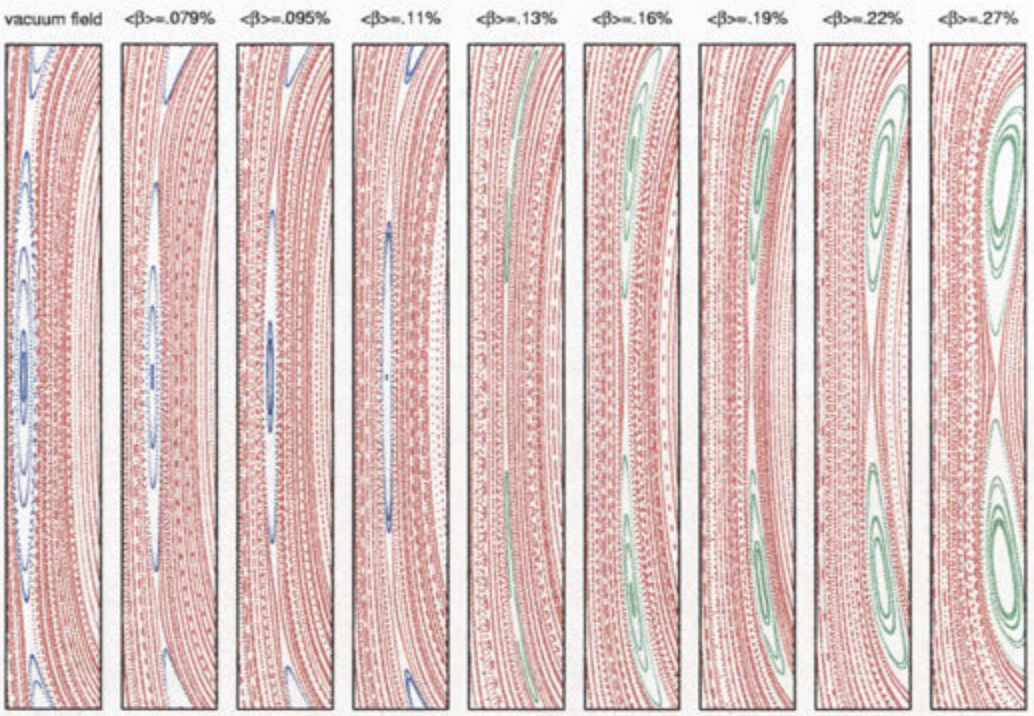

Figure 7.4: Detail of the Poincaré sections for the Island-3 configuration showing self-healing and change of phase for the 6/5 island with increasing $<\beta>$. The area shown is 8×60 mm (about 2 × 9 grid spacings) and is centered on $Z = 0$ between the poloidal field coil to the left and the magnetic axis to the right.

configuration for comparing simulation with experiment at pressures easily obtainable in H-1NF. However a much larger external field correction would be needed to produce magnetic islands that will heal at significant β, and so improve the maximum achievable β for H-1NF. Using the vertical field coil currents to achieve this might be problematic because the large changes to the currents in the vertical field coils needed would significantly change other field parameters such as the ellipticity of the magnetic surfaces and the size of the vacuum well or hill. (A purpose built coil designed for maximum effect on resonant field components would be needed.)

The island chain in the Island-3 configuration starts larger than the Island-2 vacuum islands but of the same phase, and exhibits similar self-healing followed by growth of the island with opposite (see Fig. 7.4). the change of island phase in the Island-3 configuration occurs at about .12%, also very similar to the $<\beta>$ at which the Island-2 configuration changed phase (.17%).

The Island-3 configuration has a larger magnetic hill and a slightly larger vacuum island than the Island-2 configuration. The larger vacuum island might be expected to heal at higher β but this was not the case. The larger hill should give less island stability and a more abrupt change of phase with less island shrinking beforehand.

If this effect is present, it is not obvious from pictures - more exact measurements of island size are needed to detect this effect.

Island-1 and Island-2 configurations show similar island growth patterns. This growth pattern is consistent with theoretical predictions for a vacuum island of opposite phase to global linear perturbations and with very little influence from local non-linear island currents. The island width in this pressure range is always smaller than two grid spacings so it is not surprising that local current effects are not seen. The smallest island widths near the transition in island phase are much smaller than the vacuum island width and suggest there is no restriciton on minimum island size, nor a significant pressure range where two equilibrium solutions are possible.

7.2 Breakdown of nested flux surfaces into stochastic field lines

Stochastic regions develop first around the island separatrix. This region is particularly vulnerable to being disturbed by non-resonant perturbations because of the high Lyapunov exponent associated with the approach to a rational rotation value. By about 3% average β large volumes of magnetic field toward the outer region of the plasma have become stochastic. Plasma confinement would be seriously degraded by this β. Pressure confinement would be reasonable only for the region of 'nice' magnetic surfaces in the center. This reduces the contained plasma volume to about a quarter of the original plasma volume. Further increases in peak pressure reduce the region of 'nice' magnetic surfaces, and the contained plasma volume, further. The ability of the stochastic field lines of the high β equilibrium of the Standard configuration to transport plasma can be seen in Fig. 7.6. A single field line, followed for 3500 periods covers all of the stochastic region allowing rapid plasma transport throughout this region. A substantial portion of the previously contained plasma volume is now connected to the boundary. This degradation of flux surfaces limits the maximum achievable $<\beta>$ of the Standard configuration of H-1NF to about 2.5%. This limit on $<\beta>$ given by magnetic surface breakdown is significantly stricter than the $<\beta>$ limit found in Chapt. 6 from magnetic island drift ($<\beta> \approx 4\%$).

The β onset of large scale stochasticity in the Island-1 configuration is not much different from the Standard configuration. The volume of contained plasma is also very similar to that of the Standard configuration at equivalent peak β. The presence of a low order rational surface and a significant vacuum island has not reduced the maximum achievable β for this configuration. It will ,however, degrade the plasma confinement somewhat at low β before stochasticity becomes crucial.

Large areas of stochasticity are expected when islands of different harmonics overlap. In the section on simple maps I showed that stochastic regions could form from the overlap of islands from different resonant surfaces. Cary & Kotschenreuther (1985) predicted that the reinforcing effect of local island currents in the presence of a magnetic hill will give overlapping islands, at all orders, for arbitrarily low β. Hegna & Bhattacharjee (1989) showed that at high β the resistive Mercier stability

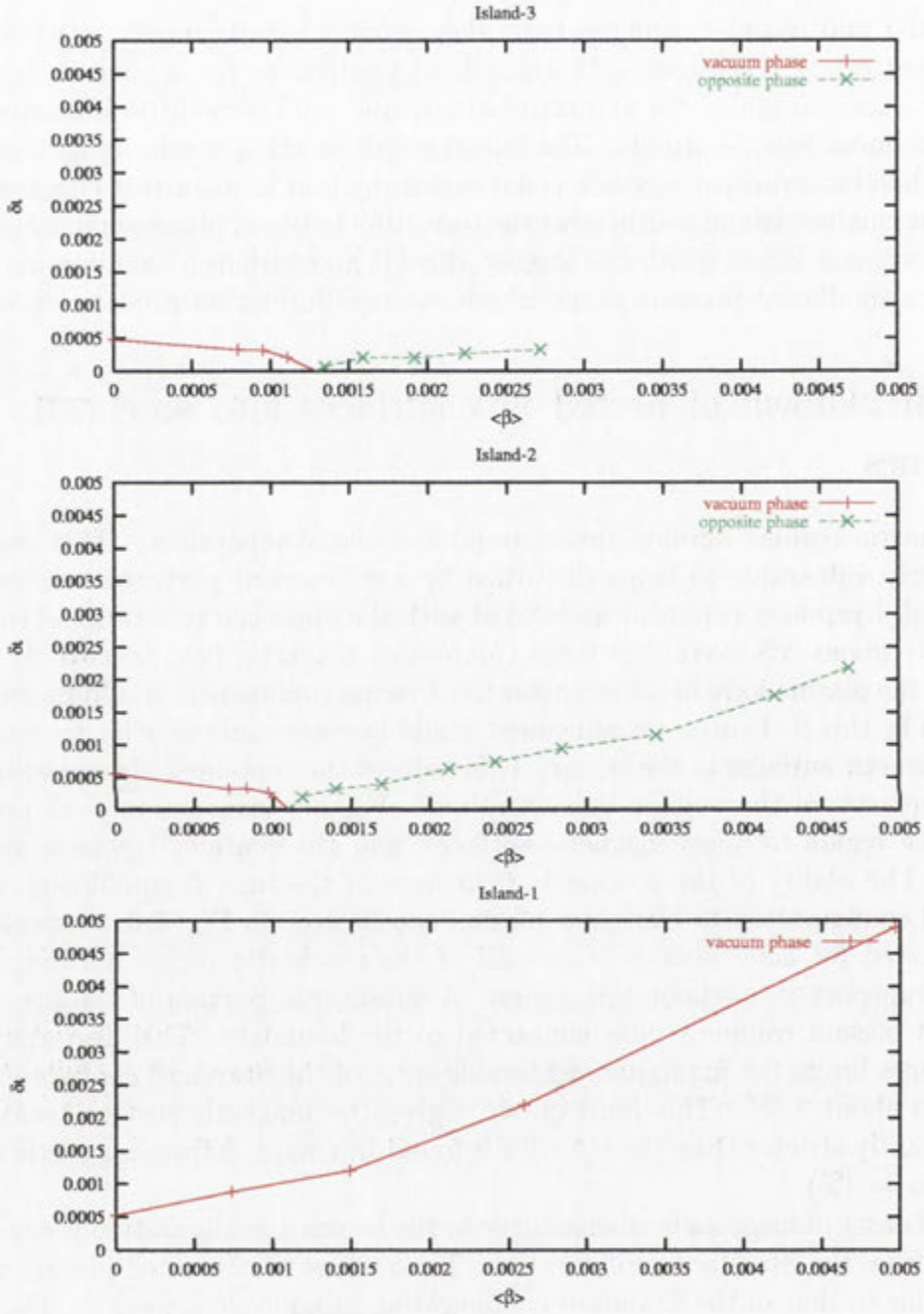

Figure 7.5: Island growth patterns for the three field configurations with significant vacuum islands. The island extent in rotational transform is measured from the rotation period at the centre of the island. Some unevenness in the island size is due to variation in the effective amount of relaxation for different calculations. This suggests that the equilibriums are not completely relaxed.

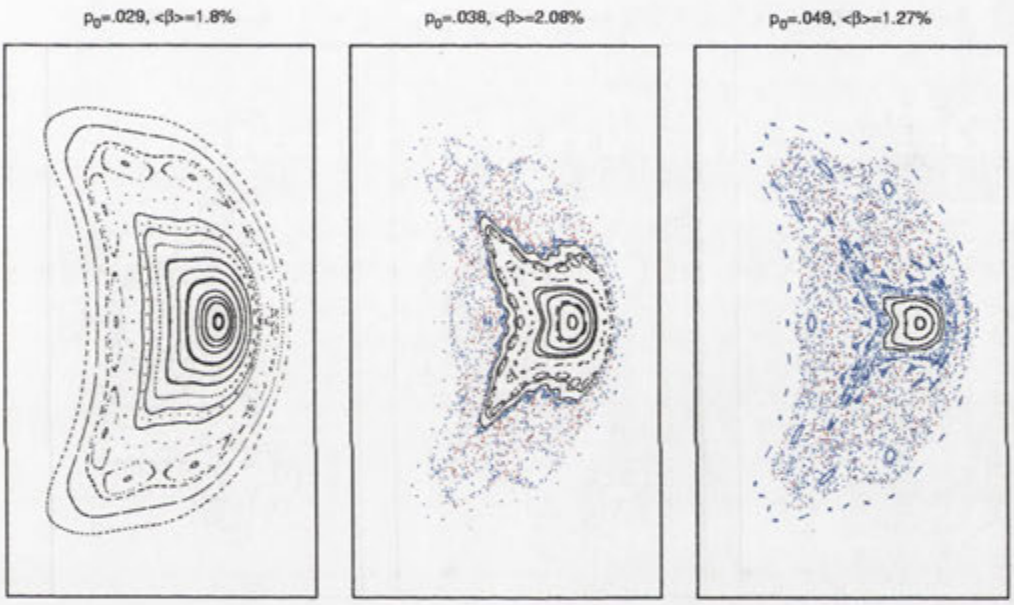

Figure 7.6: An increasing pressure series of Poincaré sections through $\phi = 0$ at high β for the Standard configuration. The area shown covers the full simulation region of 27×48 cm. While the peak pressure is increasing significantly in this series, increasing stochasticity and associated pressure flattening means the average β does not increase at the same rate.

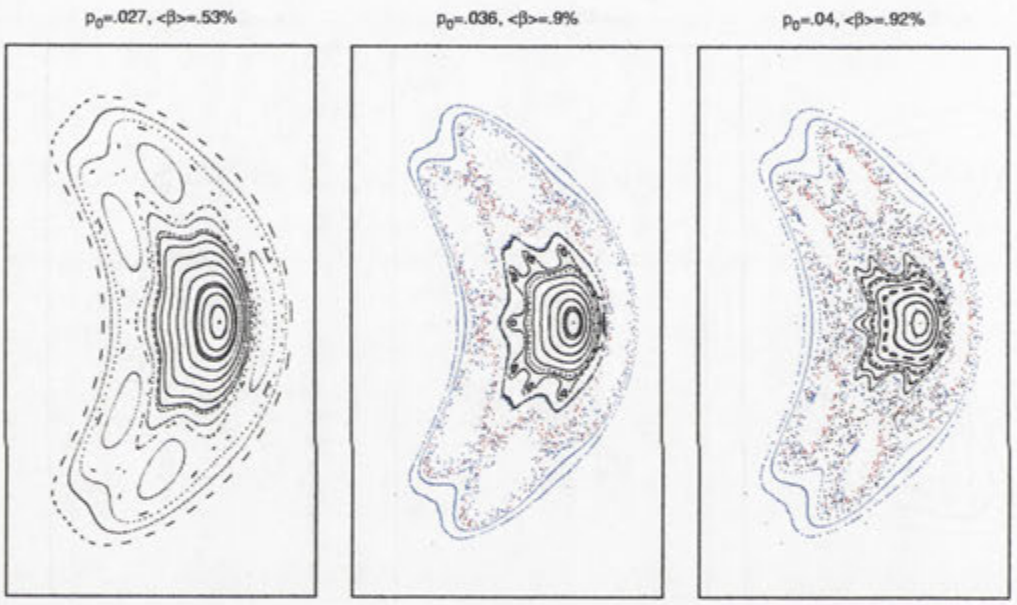

Figure 7.7: An increasing-pressure seriesof Poincaré sections through $\phi = 0$ at high β for the Island-1 configuration. The area shown covers the full simulation region of 27×48 cm. While the peak pressure is increasing significantly in this series, increasing stochasticity and associated pressure flattening means the average β does not increase.

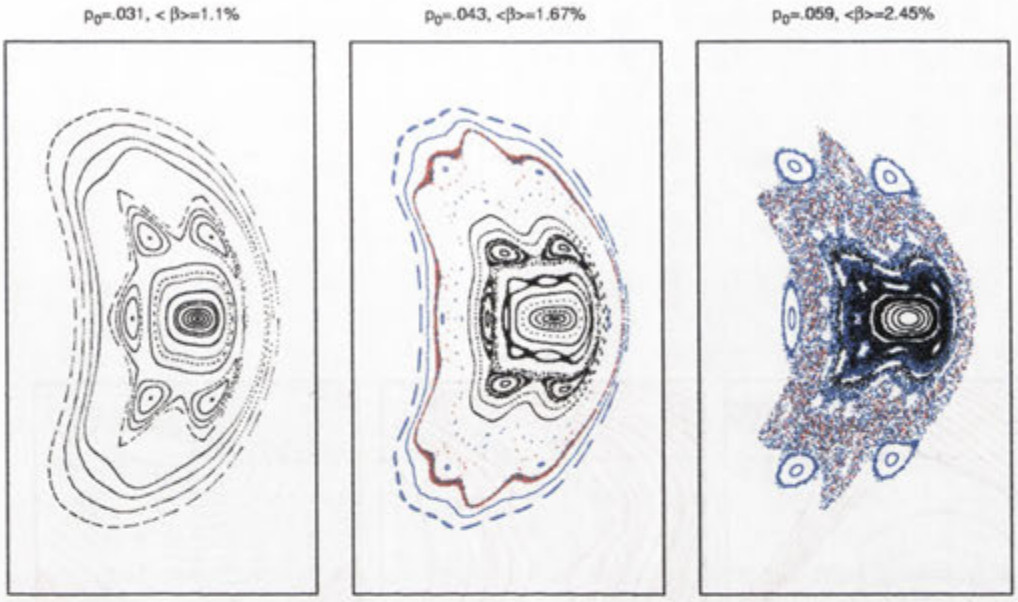

Figure 7.8: A pressure increase series of Poincaré sections through $\phi = 0$ for configuration Island-2. The area shown covers the full simulation region of 27×48 cm.

criteria, D_R, rather than the presence of a magnetic well or hill, was the deciding influence on local island currents. Thus as β reaches a critical value at which the destabilising geodeisic curvature counters the effect of the stabilising magnetic well, the equilibrium magnetic field becomes stochastic. Measurements of D_R (Fig. 7.15) showed that both the Standard and Island-1 configurations became unstable by $<\beta> \approx 0.7\%$. This would explain the similar β limit from the onset of stochasticity despite very different vacuum island size.

Very high order islands ($l = 25$) are noticeable in the good surfaces region of both the Standard and Island-1 configurations (Fig. 7.6c and Fig. 7.7c). This indicates that high-frequency perturbations to the magnetic field have grown large enough to get significant overlapping of islands from high order resonances.

The Island-2 configuration became stochastic at high β in a similar way to the Island-1 configuration. Because of the small magnetic hill, this configuration should be unstable to islands and the theory of Cary & Kotschenreuther (1985) would predict island overlap and stochasticity at arbitrarily low β. However, in these simulations I found the onset of stochasticity delayed until a similar β to the onset of stochasticity for configurations that had vacuum magnetic wells.

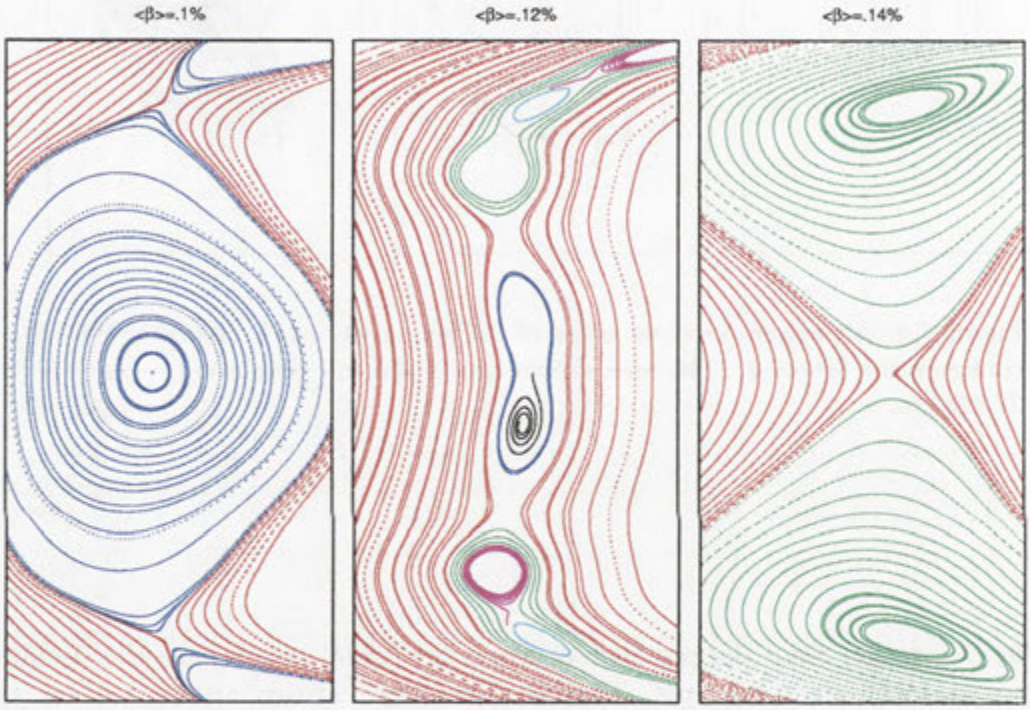

Figure 7.9: Detail of island phase change with evidence of higher harmonic perturbations at minimum island size for configuration Island-2. The area shown is about 1×60 mm (about 0.25×9 grid spacings with the horizontal scale stretched to show details of the narrow island topology. The spiralling field lines in the centre plot show that this island is nearly the smallest that can be resolved for this accuracy of field line calculation.

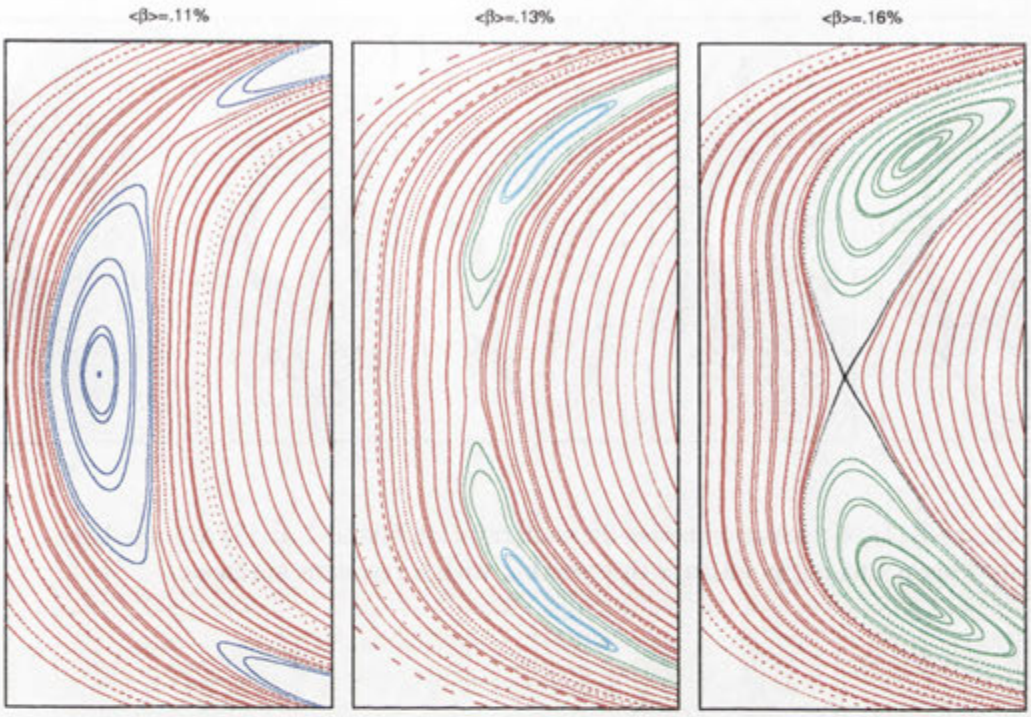

Figure 7.10: Detail of island phase change with evidence of higher harmonic perturbations at minimum island size for configuration Island-3. The area shown is about 3× 60 mm (or 0.8×9 grid spacings)

7.3 Unusual flux surface topologies

Looking in detail at the island topologies near the change of phase, it is possible to see the influence of higher harmonics of the resonant perturbation. This is shown for the Island-2 configuration in Fig. 7.9, where the island O-point splits and transforms into an X-point. The topology of these flux surfaces matches the topology seen earlier (Fig. 2.5) for a twist map with a large higher harmonic added to the lowest order harmonic. High-order harmonics are also significant at the phase change of the Island-3 configuration (Fig. 7.10). These harmonics are present in different strengths and phases from those present at the Island-2 phase change and give a different island topology. As the main harmonic perturbation is reduced to zero (from competition between the external vacuum perturbation and the plasma currents) the higher harmonics dominate the field line topology. It is highly unlikely that all resonant harmonics could be made to vanish at the rational surface at the same time. The presence of higher harmonics prevents complete self-healing. However the island width from higher harmonics is small enough so that this is unlikely to be a serious problem.

At larger β, in the Island-2 configuration, the rise of rotational transform on axis causes a second rational surface to develop in the plasma, moving outward from the

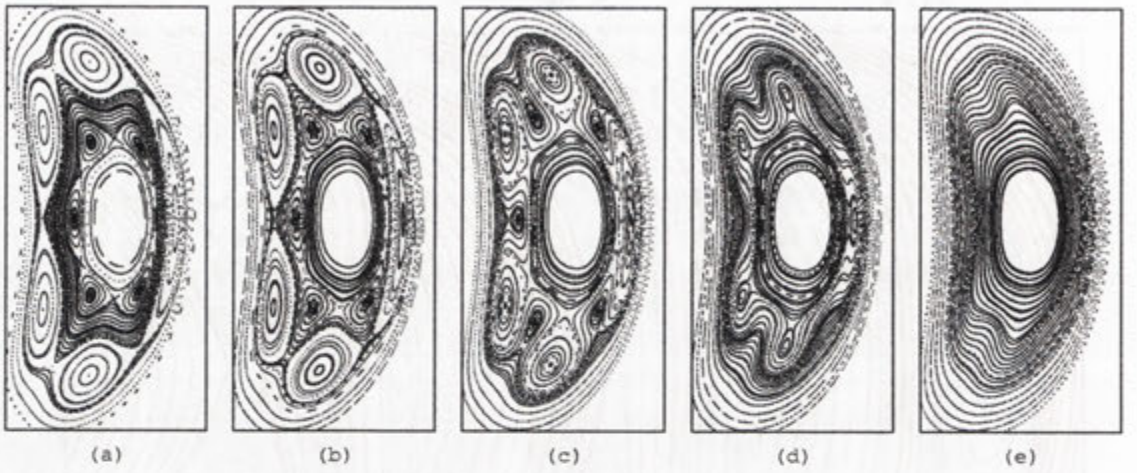

Figure 7.11: A relaxation series for configuration Island-2 at 1% average beta showing a turning point in ι intersecting with a resonant surface

magnetic axis. An island develops at this surface of opposite phase to the original island because the shear has opposite sign (see Fig. 7.11a). Further increases in β increase ι and drive the two rational surfaces together. A distinctive island topology develops as the rational surfaces come together and the island chains merge. This topology is easiest to see during a HINT relaxation, during which the rotational transform around the magnetic axis also rises. In Fig. 7.11b the separatrices of the two islands are nearly touching. Further increase in ι causes the two separatrices to merge joining the X-points of the two island chains together (not shown). In Fig. 7.11c, the island topology has changed, with the separatrix through the X-point of the outer rational surface surrounding the O-point of the inner rational surface, and vice versa. As the rational surfaces move closer together the island size shrinks. In Fig. 7.11d, only the outer O-points still have significant islands around them. Figure 7.11e shows the flux surface topology when ι rises enough to remove the rational surfaces from the plasma. The magnetic surfaces at the turning point in ι are still significantly deformed by the nearby resonant perturbation. This topology change is very similar to that demonstrated with the non-twist map (Fig. 2.3) in Chapter 2 section 2, with some differences due to a lack of symmetry between inner and outer flux surfaces.

This island topology has been seen before in HINT simulations of H-1NF (Hayashi *et al.* (1995)) and is likely to occur in any stellarator with a turning point in ι that produces two rational surfaces of the same value, closer together than the islands produced at these rational surfaces. The tendency for ι to increase near the magnetic axis, causes turning points in ι in many stellarators so this topology could be common.

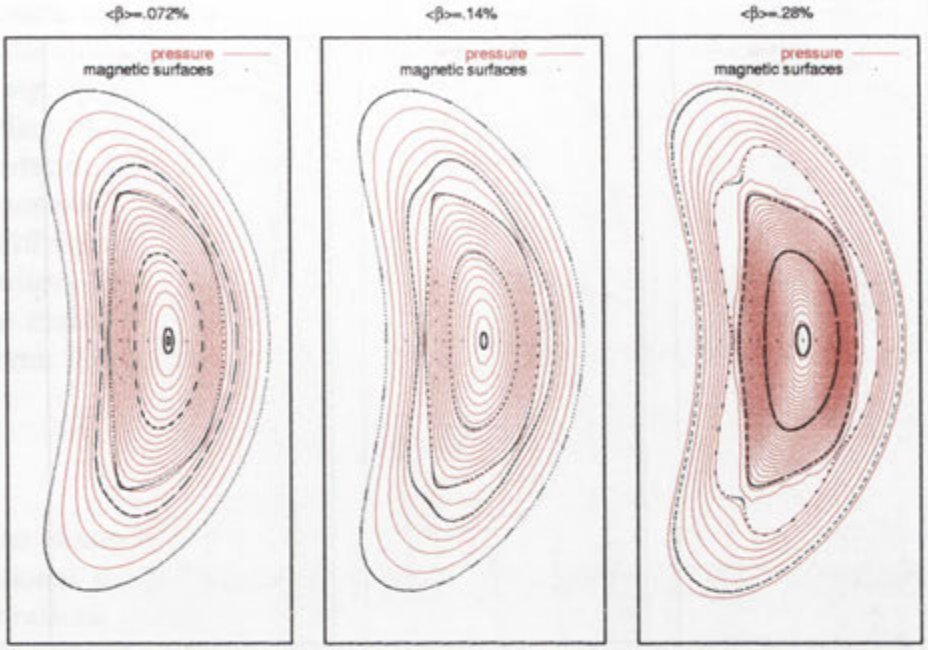

Figure 7.12: Pressure contours and flux surfaces for Island-1 equilibria showing pressure flattening within the island. Maximum island width shown is 9mm in the horizontal direction which is about two grid spacings.

7.4 Effect of islands on local pressure and current

An island in the equilibrium magnetic field influences the local pressure and current distributions. The pressure must be constant along the equilibrium flux surfaces within the island. Thus, the island will produce a region of significantly flatter pressure than the rest of the plasma with the possibility of a small local peak or dip in the pressure at its centre. The local current responds both to the change in the pressure profile and to the deformation of the magnetic surfaces within and near the island. The current must be contained within flux surfaces, so it will deform following the flux surfaces. The current within the island will also be substantially reduced by the flattening of the pressure profile. In order to model non-linear contributions to the growth of islands, HINT must be able to resolve the influence of an island on the surrounding pressure and current distributions.

The new pressure relaxation algorithm PR3 was introduced to ensure HINT could resolve pressure flattening within islands. Using this method, HINT achieved substantial pressure flattening within magnetic islands for all islands above a critical size in the simulations (shown for the Island-1 configuration in Fig. 7.12). The pressure profile within the magnetic island at $<\beta> = .28\%$ is completely flat. At lower β the smaller islands have some pressure gradient across them but the pressure is still flatter than in the surrounding plasma region.

Figure 7.13 shows the effect of the island chain in the Island-1 configuration on

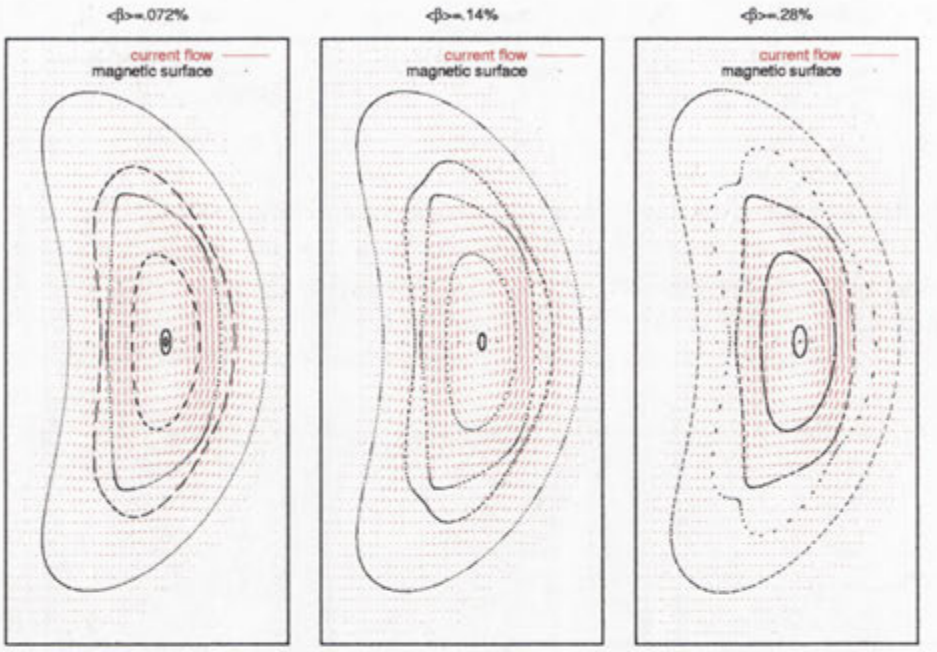

Figure 7.13: current flow lines and flux surfaces for Island-1 equilibria showing significantly diminished current within island. Maximum island width shown is 9mm in the horizontal direction which is about two grid spacings.

the local currents. HINT was able to resolve the drop to minimal perpendicular current within the island at $<\beta> = .28\%$ (where the island width is about two grid spacings) and also a reduction in perpendicular current within the island at $<\beta> = .14\%$ (where the island width is about 1.5 grid spacings) due to the reduced pressure gradient within this island. In the plasma region surrounding the islands, the direction of current flow within the plane follows the deformed flux surfaces.

Since the island has a noticeable effect on local currents within HINT, it is possible in principle for HINT to include the effect of local island currents on the growth of the island. I have not divided the current up into resonant and non-resonant components which would be needed to test whether the local resonant current peaks in the manner predicted by Cary & Kotschenreuther (1985) and by Hegna & Bhattacharjee (1989).

7.5 Shifted-Near-Island configurations

Initial vacuum fields of Near-Island configurations differ from their corresponding Island configurations by a small change to the current in the helical winding (see Chapt. 5.2). It was shown in the Chapt. 6 that the equilibria were very similar to the corresponding island configurations, having almost the same bulk properties except for a shift in rotational transform, so that the rational surface and associated

island were not present. The total plasma currents, flux surface ellipticity and indentation, magnetic axis position, well depth and magnetic shear of the Near-Island equilibria were very similar to the corresponding Island equilibria. There is a local effect of eliminating the island deformation of the magnetic flux surfaces with the corresponding deformation of the pressure contours and current flow surfaces. The resonant currents near the rational surface of an Island configuration, will be quite different from those at a similar position in the corresponding Near-Isand equilibrium, that contains neither island nor rational surface.

The main effect on the parallel currents comes from the change in rotational transform. The parallel current components are given (see Chapt. 2.5) by:

$$Q_{lm} = \frac{-p'(\psi)\mathcal{J}_{lm}(\psi)}{\iota(\psi) - m/l}$$

with the characteristic $1/(\psi - \psi_{lm})$ current singularity for the resonant current at the rational surface. The most important difference between parallel currents of configurations containing an island, and the corresponding Near-Island configurations, is a small constant term $\Delta\,\iota$ added to the rotational transform. This removes the singularity from the resonant current making it smooth:

$$Q_{lm} = \frac{-p'(\psi)\mathcal{J}_{lm}(\psi)}{\iota(\psi) + \Delta\,\iota - m/l} \cong \frac{-p'(\psi)\mathcal{J}_{lm}(\psi)}{\Delta\,\iota}$$

For non-resonant harmonics $\iota(\psi) - m/l \gg \Delta\,\iota$ so the non-resonant currents are largely unaltered.

The removal of resonant surfaces clearly prevents local-island resonant currents from forming in the Near-Island equilibria. Resonant parallel currents are changed drastically by the change in ι. The theory of Cary & Kotschenreuther (1985) and Hegna & Bhattacharjee (1989) assumes that changes in island size are due almost entirely to a combination of the singular resonant currents and to island induced resonant currents. They use a cylindrical approximation for flux surfaces to calculate island widths, which excludes the contribution of non-resonant currents.

An equilibrium magnetic field can be separated into the vacuum field and the magnetic field due to the plasma currents. I combined the vacuum magnetic field from the Island configurations, with the magnetic field due to plasma currents from the corresponding Near-Island equilibria to get shifted-Near-Island magnetic fields. These non-equilibrium magnetic fields had identical vacuum fields and almost identical non-resonant plasma currents to the corresponding island equilibrium but very different resonant plasma currents (both 'global-linear' and 'local-island'). (The direction of the global-linear resonant currents in the Near-Island equilibria can be reversed by changing the sign of the rotational transform shift, $\Delta\,\iota$). Comparing the island sizes of the two fields should give some idea of the effect of the non-resonant plasma currents.

The island widths of the Island-1 and the shifted-Near-Island-1 configurations are compared in Fig. 7.14. From identical vacuum fields islands of both these configurations grow linearly with increasing β, at nearly identical rates, until $<\beta> = .25\%$.

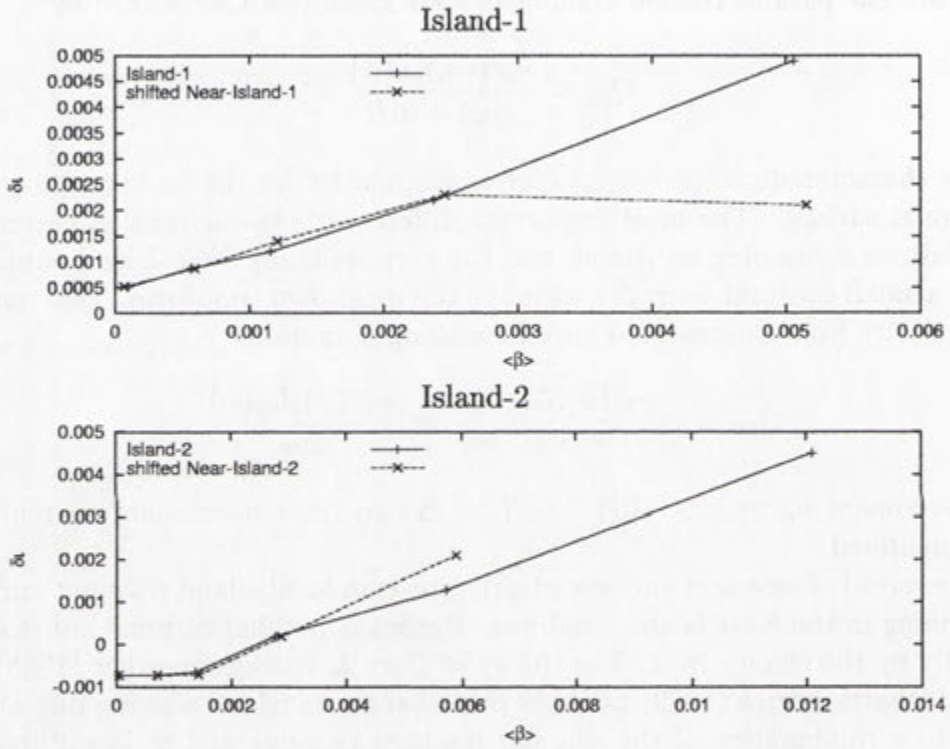

Figure 7.14: The upper plot shows a comparison of island width found in the Island-1 equilibrium magnetic fields and the shifted-Near-Island-1 magnetic fields. The lower plot shows a similar comparison for the Island-2 and shifted-Near-Island-2 magnetic fields.

At higher β than this, the island width in the shifted-Near-Island-1 configuration saturates while the island width in the Island-1 configuration continues to grow linearly. Islands of the Island-2 and the shifted-Near-Island-2 configurations (compared in Fig. 7.14) maintain their vacuum size and phase until $<\beta> = .14\%$ then change phase between this β and $<\beta> = .28\%$ after which they grow in the new phase, with the island of the shifted-Near-Island-2 field growing somewhat faster than that of the Island-2 field.

Thus, at low β, island widths for the shifted-Near-island fields are surprisingly similar to those of the corresponding Island configurations, despite having very different resonant currents. The global resonant-current effect, due to the currents discussed above, will be completely different for the Island and its corresponding shifted-Near-Island fields. The local resonant-current effect, from the perturbation in the flux surfaces caused by the island, will be completely absent from the shifted-Near-Island fields. Since the resulting island widths are the same neither, of these effects can be contributing significantly to the growth of islands at low β in HINT simulations. All the changes in island size must be due to global, non-resonant currents cross-coupling to give resonant field perturbations. The influence of cross-coupling was discarded in the theories of Cary & Kotschenreuther (1985) and Hegna & Bhattacharjee (1989) with the approximation of cylindrical flux surfaces. (Magnetic surfaces in H-1NF are a long way from circular. Toroidal effects are also significant and, clearly, this approximation does not apply.)

At high β island widths do appear to be influenced significantly by resonant currents. By $<\beta> = .5\%$, the island in the shifted-Near-Island-1 field is only half the width of the island in the Island-1 field. While at $<\beta> = .6\%$, the island of the shifted-Near-Island-2 field is nearly double the width of the island in the Island-2 field. At this stage, the islands of the Island-1 and Island-2 configurations are several grid spacings wide and have a significant effect on the currents around them. The difference between the island width in the shifted-Near-Island and that in the corresponding Island configuration is most likely to be due to these local current perturbations from the deformation of the flux surfaces. The balance between the global non-resonant currents and the linear resonant currents is unlikely to change much with increases in β.

7.6 Measurements of D_R and $\mathcal{J}_{mn}/\mathcal{J}_{00}$, G and C

For all configurations, and all β within the range I explored, $G = D_R s\, d\iota/ds$ was highest on axis and decreased linearly to zero at the plasma boundary. Fig. 7.15 shows the trends in G with $<\beta>$, measured from the VMEC equilibria for all of the configurations of H-1NF that I studied. The measurements of G were taken at $s = 0.5$ (at approximately the plasma radius of the rational surface). At low beta, $G = D_R$ is dominated by the contribution from the magnetic well and is proportional to β. This relationship held for G measured from the VMEC equilibria for $<\beta>$ up to about .2%. The Standard, Island-1, and Near-Island-1 configurations all had stabilising magnetic wells and so have linearly decreasing values of G for $<\beta>$ less

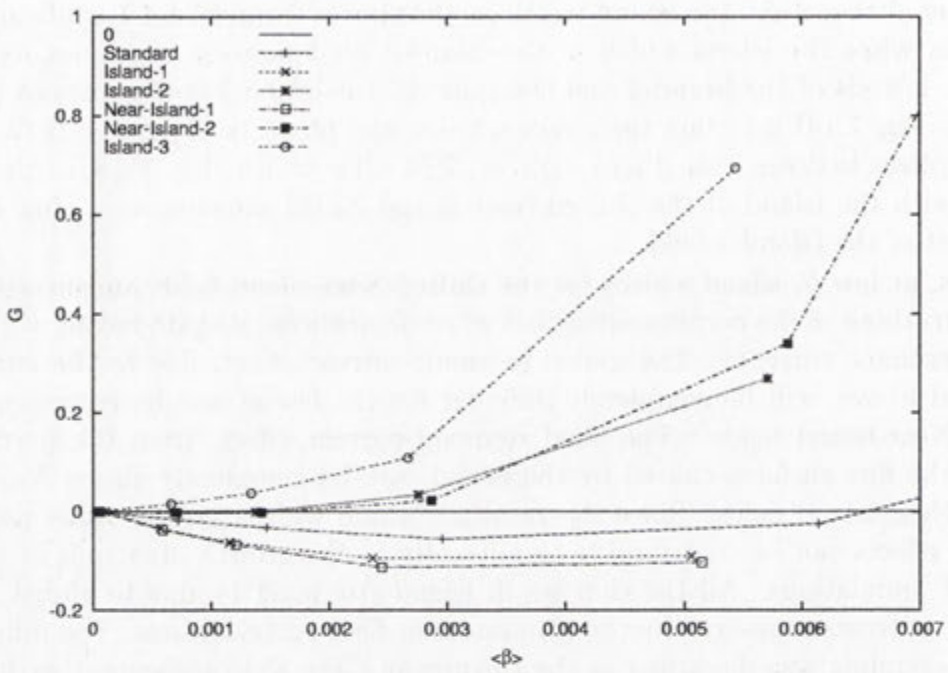

Figure 7.15: change of G with β for VMEC equilibria equivalent to HINT simulations

than .2%. The Island-1 and Near-Island-1 have very similar magnetic wells and very similar values of G. The Standard configuration has a shallower magnetic well and a smaller G. The deepening of the magnetic well as β increased made little impact on the trend.

Island-2 and Near-Island-2 had small vacuum magnetic hills as measured within HINT but VMEC gave them a very slight vacuum well. The measured G for these equilibria was close to zero for $<\beta> < .2\%$. The Island-3 configuration had a larger vacuum magnetic hill and an increasingly unstable G.

For $<\beta>$ above .3%, G became strongly influenced by destabilising parallel current terms. All configurations began to show an upward trend in G with the Island-1, Near-Island-1 and Standard configurations changing from stable to unstable at around $<\beta> = .7\%$. The Island-2, Near-Island-2 and Island-3 configurations were already unstable, but G increased more rapidly for $<\beta> > .3\%$.

The standard configuration has an initially stable G from the magnetic well. The magnitude of G increases linearly with the equilibrium β until G reaches .05 at about $<\beta> = .3\%$. After this β, the destabilizing parallel current term becomes significant. Initially this decreases the magnitude of the stable G but by $<\beta> = 0.7\%$ G is significantly unstable.

The theory of Cary & Kotschenreuther (1985) uses J_{mn}/J_{00} from the unperturbed vacuum field as the driving force for global contribution to island size. Hegna & Bhattacharjee (1989) contend that the total field J_{mn}/J_{00} is more accurate. I found J_{mn}/J_{00} to vary considerably over the plasma and with beta. It was

not possible to get an unperturbed vacuum field measurement of J_{mn}/J_{00} since the vacuum fields are perturbed with a vacuum island and the method of introducing the island included substantial field changes (not just the minimum necessary to remove perturbation). I have used the value of J_{mn}/J_{00} at $s = 0.5$ for the scale of the contributions from global resonant currents.

7.7 Comparison of theory and measurements of island size

The theory of Bhattacharjee *et al.* (1995) predicts that island widths respond to pressure increases according to :

$$\delta\, \iota = G/2 + \sqrt{(G/2)^2 + |C + \delta\, \iota_v^2|}, \tag{7.1}$$

where G is the effect of local island resonant currents to the island width, C is the contribution of global resonant currents to the island width and $\delta\, \iota_v$ is the original vacuum island width. I substitute the values of G and C (calculated in the previous section) into equation 7.1 to get predicted island widths for the HINT configurations Island-1 and Island-2. In Fig. 7.16 the predicted island sizes are compared with the actual island sizes measured from the HINT equilibrium magnetic fields.

For the Island-1 configuration the predicted island width shrinks rapidly from the vacuum island size and remains vanishingly small for all of $0 < <\beta> < .5\%$. This theoretical island width is dominated by the stabilising effect of the magnetic well giving a negative G with large magnitude. The island width measured from the HINT equilibrium magnetic field grows linearly with β, showing no influence from the magnetic well via the local island currents.

The predicted island width in the Island-2 configuration is also dominated by the effects of G. The Island-2 configuration had a positive value of G increasing quickly with β for $<\beta> > .3\%$. This caused the predicted island width to increase rapidly for $<\beta> > .3\%$, although it still allows for a change in the island phase. The measured island width of the HINT magnetic field grew much more slowly. At $<\beta> > .3\%$ and $<\beta> > .6\%$ the measured island width is less than a hundredth of the predicted value. The change in island phase is predicted by the competition between C and the vacuum island. It is completely independent of G.

The measured island width of the Island-3 configuration showed a similar pattern of growth to the Island-2 configuration. The Island-3 configuration has a significant magnetic hill and the predicted island width grows very rapidly from very low β. Similarly, G dominates island size calculation for Island-2 and Island-3 configurations. In this case islands will grow dramatically despite vacuum islands being of opposite phase.

The measured island sizes show very little actual contribution from local island currents. This discrepancy indicates that HINT does not include the peaked resonant currents around small islands. This may be because the spatial resolution is insufficient to catch highly peaked currents, because the pressure flattening around the island extends past the island boundary, or because the local currents take longer to develop than the relaxation times used here. The measured island sizes do

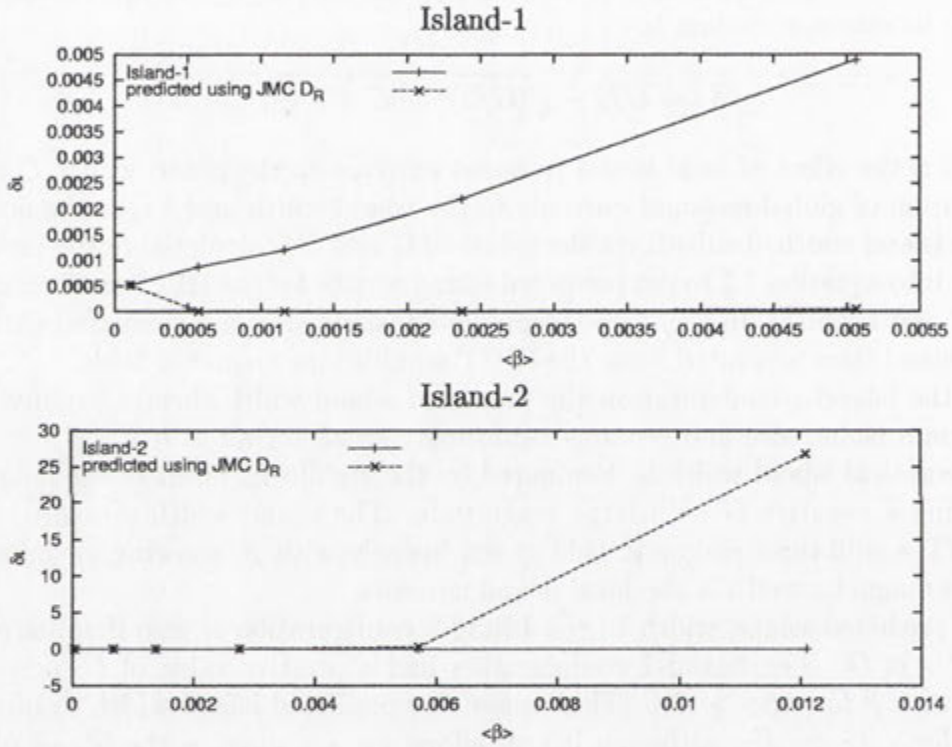

Figure 7.16: The upper plot shows a comparison of island width found in the Island-1 configuration and the predicted island width from the theory of Bhattacharjee *et al.* (1995) with the D_R measured using the JMC code. The lower plot shows a similar comparison for the Island-2 configuration

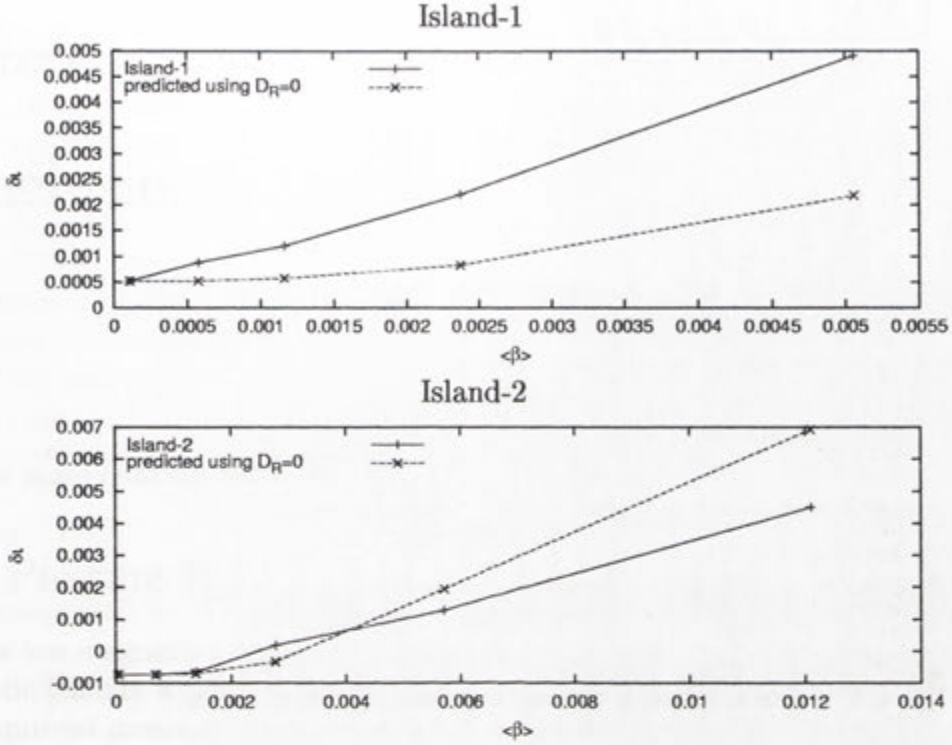

Figure 7.17: The upper plot shows a comparison of island width found in the Island-1 configuration and the predicted island width from the theory of Bhattacharjee *et al.* (1995) with the $D_R = 0$. The lower plot shows a similar comparison for the Island-2 configuration.

compare reasonably with the theory (see Fig. 7.17) if local island current effects are ignored and only global resonant current contribution is included giving the island width $\delta\, \iota = \sqrt{|C + \delta\, \iota_v^2|}$ (using C calculated from the equilibrium values of Jmn at $s = 0.5$). The results show appropriate trends and orders of magnitude considering the uncertainties of the Jmn measurements. Earlier comparisons of island sizes with shifted-Near-Island equilibrium island sizes in Sect. 7.5 showed that non-resonant currents are the largest contribution to island growth and self-healing. For the calculated values of resistive stability and field strength perturbation driving resonant currents the local island currents should dominate but actually had little effect on the simulations. This shows that HINT does not resolve the local island currents for island widths several times the grid spacing. This has a significant effect on the predicted island size and on the beta at which the magnetic surfaces break up into stochastic regions.

CHAPTER 8

Conclusions

The main conclusions of this thesis are summarised in this chapter

8.1 Pressure Relaxation in the HINT code

The low magnetic shear of heliacs leads to very slow rotation of field lines within magnetic islands which in turn makes pressure flattening very slow within HINT. My improved pressure relaxation algorithm, described in Chapt. 5, uses interpolation from sample points along the field lines to increase the efficiency with which information (from pressure averaging along field-lines) is used to calculate the relaxed pressure on the simulation grid. It is effective in reducing the convergence rate for the pressure within magnetic islands in low-shear stellarators. The time taken to flatten the pressure within an island for a particular H-1NF magnetic field was reduced by a factor of 50. Some additional averaging of the new pressure along the field lines was needed to reduce the local errors caused by the interpolation process. With this smoothing in place, my improved pressure relaxation had almost identical convergence for the overall HINT process, but with substantially less computation time to achieve pressure flattening within the islands.

8.2 Summary of island theory and applicability to HINT simulation

The island growth theories of CK and HB, based on resistive magneto-static equilibrium, consider the effect on the size of an island from the plasma currents which can be divided into three parts: global, non-resonant currents, global, resonant currents and local, island currents.

The global, non-resonant plasma currents can contribute to the resonant field perturbation which causes an island at the rational surface. This effect depends on the exact three-dimensional nature of the vacuum field and on the plasma currents. It is impossible to calculate analytically and the size of its contribution may vary dramatically. Cary and Kotschenreuther mentioned this effect but left it out of more detailed calculations by using a circular flux surface approximation. HINT includes this contribution which was quite large for H-1NF since its bean shaped

flux surfaces deviate substantially from a circle. The contribution of global currents to island size is linear, in that it is not substantially effected by the size of the island or details of the currents around it. This makes it fairly easy to add the effect back to the theoretical calculations once the contribution has been determined for the particular magnetic field by a numerical method such as this HINT simulation.

The linear, resonant current (described in Sect 2.5) is highly-peaked and singular at the rational surface. However, because it is antisymmetric about that surface the effect on the resonant field perturbation at the rational surface largely cancels out. The resonant currents far from the surface have unequal effects on the resonant field perturbation and their contributions can be just as important despite being significantly smaller than the current near the rational surface. For this reason these currents can be considered as a global effect despite being very highly peaked locally. The development of a small island removes the singularity of the current at the rational surface but does not change the main effect. Similarly, the grid spacing of HINT may not be able to resolve the highly peaked resonant current around the rational surface but it will capture most of the contribution of linear resonant current to island size.

The local island resonant current described in Sect. 2.7 is highly peaked at the island separatrix (though not actually singular). This current is caused by the perturbation in field strength on a surface due to the deformation of the magnetic surface around an island. It depends on the field strength gradient across the unperturbed flux surfaces (i.e. on the presence of a magnetic well or hill) and it is symmetric across the rational surface. The current is peaked in a similar way to the linear resonant current but its symmetry means that the effect on the resonant field is due only to the local currents which can be treated as a delta current at the center of the island. The inability of HINT's grid spacing to resolve the current peak near the island separatrix may substantially reduce the effect of this current on island size within the simulation.

8.3 Summary of results from island growth simulations

The results from comparing the shifted-Near-Island with the corresponding Island magnetic fields (presented in Sect. 7.5) showed that, at small island size and low β, the island-width changes were dominated by effects from global, non-resonant currents. The local island currents would obviously have been absent from the plasma currents of the shifted-Near-Island fields and the global resonant currents would have been completely different from those of the corresponding Island magnetic fields yet the island sizes were almost identical. At higher β, and larger island width, the shifted-Near-Island and corresponding Island fields started to differ significantly. The global-resonant and global-nonresonant plasma currents are likely to grow at similar rates as β increases. This effect is, therefore, more likely to be due to the effects of local island currents becoming important.

Theoretical predictions of island growth, using values of D_R and $\mathcal{J}_{mn}$ calculated from the equilibrium configurations, were compared with results from HINT simula-

tions in Sect. 7.7. These showed that the local island currents should dominate the island growth but that this effect was not being included in HINT. Island widths agreed better with theory if the local island current contributions were removed leaving only the global, resonant currents. Considering the shifted-Near-island results, and the uncertainty in the measurement of $\mathcal{J}_{mn}$, this island growth is more likely to be due to global non-resonant currents not included in the theory.

Two equilibrium solutions are predicted by theory around an island phase flip for the configurations that have a magnetic hill. We did not attempt to find two these two solutions with HINT or study the hysteretic transition between island phases since the island widths in the vicinity of the transition were smaller than the grid spacing and the non-linear island currents that lead to two solutions could not be resolved.

The conclusion is that HINT captures the effects of global, non-resonant currents and a small proportion of the effect of local island currents. Global, resonant currents did not seem to play a large role in either the theory or the simulation.

The effect of finite Larmor radius on island growth in physical experiments could be similar to the effect of finite grid spacings in numerical simulations. Both reduce the formation of highly peaked currents at an island separatrix or rational surface. It is essential to compare island growth predictions of theory and numerical simulations with equivalent experimental results if theory and numerical simulations are to be relied on to design new stellarators with favourable island properties. Very few direct comparisons of island growth have been made between the theories and numerical simulations covered in this thesis and comparable experimental situations. Detection and measurement of island widths within experiments is not easy, especially for small islands. However, tomographic reconstructions of plasma density profiles are now achieving high enough resolutions to detect these islands in H-1NF. The configurations studied here would be unsuitable for direct comparison with experiment instead full torus simulations of the 5/4 island would be needed.

Comparisons of equilibrium containing islands calculated by HINT with equilibria calculated by PIES, and other MHD equilibrium codes capable of handling islands, would also be beneficial.

8.4 Island minimisation through external currents

External current correction of islands has reasonable prospects where island size is dominated by linear contributions from global plasma currents. The self-healing and phase change of the island in the Island-2 configuration shows that resonant perturbations in the vacuum field (i.e. total field from external currents) can have a different phase than resonant perturbations in that part of the magnetic field caused by the plasma currents. This is a critical condition allowing for a system of minimising the size of finite pressure islands.

If local island currents were having a dominant effect on island growth then optimising stellarators for resistive Mercier stability at high β would be the best way of minimising island growth. Figure 7.16 shows that, if the local island currents

were having the full effect predicted from the theory, the Island-1 configuration of H-1NF has sufficient magnetic well stabilisation of islands to reduce their size to be significantly less than the vacuum island size at moderate β. In this case, the size of the perturbations caused by external currents and global plasma currents is counteracted by local currents flowing in response to the presence of an island. This would be simpler than controlling the island size by external currents since the feedback system is automatic.

If the magnetic configuration is significantly unstable by the resistive Mercier criteria (as at higher beta for the Island-2 configuration) then islands will grow large even with minimal linear perturbations. Some reduction in island size is possible using external currents but it is not very effective since the minimum island size will still be quite large.

If the influence of local island currents is small then techniques to change the phase of the vacuum island by adding external currents (as was done in these configurations between Island-1 and Island-2) can be effective in minimising the island size for some particular beta.

In an experiment or reactor design, island control would be needed across a large range of beta and a dynamic system of changing the external field perturbation as the beta in the device changed. Getting the external currents right would require either detailed and accurate calculations of expected island size with beta and external current, or a real time measurement and feed back system.

It would be desirable that the external currents that changed the size and phase of the resonant perturbation of the external field had minimal effect on other parts of the vacuum field. This was not the case for the method of changing external field perturbation used to get from Island-1 to Island-2. Changes to currents in the vertical field coils to enable self-healing at low beta produced significant changes in the vacuum magnetic well and plasma shape. Larger changes to currents in the vertical field coils would be needed to enable self healing at beta approaching the confinement limits and this change in current is likely to take other magnetic field characteristics out of a desirable range. To avoid this problem a special coil with maximum effect on the resonant perturbation could be designed.

8.5 Development of stochasticity

All of the observed stochasticity started to develop at island separatices and progressed to cover a large proportion of the plasma volume. Configurations not originally containing a low order rational surface developed one as the rotational transform changed with high beta. Investigations to examine more configurations where large islands are not present even at high beta might delay stochastic breakdown. This could be done either with more careful management of the rotational transform by choice of helical current, or with more sophisticated use of external currents to counter island growth when a low order rational surface is present.

The development of wide-spread stochasticity imposes a limit on the maximum beta of a magnetic configuration. For all the configurations studied, the maximum

$<\beta>$ before widespread stochasticity was between 2% and 4%. This beta limit was not well predicted by theories of island growth and overlap that included local island currents but which did not take into account finite grid spacings or finite Larmor radius. The theory would have predicted earlier onset of stochasticity governed by the resistive Mercier criteria becoming unstable. This is a very important limit on the usefulness of stellarators and more work needs to be done to understand and predict its onset and to find configurations in which the onset is delayed. Our simulations showed little benefit is gained in H-1NF by changing the size of the vacuum magnetic well.

Bibliography

Bauer, F., Betancourt, O. & Garabedian, P. (1978). *A Computational Method in Plasma Physics.* Springer-Verlag, New York.

Bhattacharjee, A., Hayashi, T., Hegna, C. C., Nakajima, N. & Sato, T. (1995). Theory of pressure-induced islands and self-healing in three-dimensional toroidal magnetohydrodynamic equilibria. *Physics of Plasmas* **2**, 883–888.

Boozer, A. H. (1981). *Phys Fluids* **24**, 1999.

Cary, John R. & Kotschenreuther, M. (1985). Pressure induced islands in three-dimensional toroidal plasma. *Phys. Fluids* **28**, 1392–1401.

Chirikov, B. (1979). A Universal Instability of Many Dimensional Oscillator Systems. *Physics Reports* **52**, 263.

Chodura, R. & Schlüter, A. (1981). A 3D Code for MHD Equilibrium and Stability. *Journal of Computational Physics* **41**, 68–88.

Cottingham, W. N. & Greenwood, D. A. (1986). *An Introduction to Nuclear Physics.* Cambridge University Press.

Gandy, R. F., Hartwell, G. J., D., Hanson J., Knowlton, S. F. & Lin, H. (1993). An Experimental Study of Magnetic Islands as Hamiltonian Systems. *Physics of Fluids B, Plasma Physics* **5**, 4384.

Gardner, Henry J. (1986). *The Free Boundary Equilibrium Problem for Helically Symmetric Plasmas.* Ph.D. thesis, Australian National University.

Glasser, A. H., Greene, J. M. & Johnson, J. L. (1975). Resistive Instabilities in General Toroidal Plasma Configurations. *The Physics of Fluids* **18**, 875.

Hamberger, Sydney M., Blackwell, Boyd D., Sharp, Leslie E. & D.B., Shenton (1990). H-1 Design and Construction. *Fusion Technology* **17**, 123–130.

Harafuji, Kenji, Hayashi, Takaya & Sato, Tetsuya (1989). Computational Study of Three-Dimensional Magnetohydrodynamic Equilibria in Toroidal Helical Systems. *Journal of Computational Physics* **81**, 169–192.

Harris, J. H., Cantrell, J. L., Hender, T. C., Carreras, B. A. & Morris, R. N. (1985). A Flexible Heliac Configuration. *Nuclear Fusion* **25**, 623.

Hayashi, T., Miura, H., Sato, T., Kanno, R., Nakajima, N. & Okamoto, M. (2000). Island Formation and Nonlinear Stability for Helical Plasmas Using the HINT code. In *EPS conference on Plasma Physics and Controlled Fusion.*

Hayashi, T., Sato, T., Gardner, H. J. & Meiss, J.D. (1995). Evolution of Magnetic Islands in a Heliac. *Physics of Plasmas* **2**, 752–759.

Hayashi, T., Sato, T., Merkel, P., Nuhrenberg, J. & U., Schwenn (1994). Formation and 'self-healing' of magnetic inlands in finite-beta Helias equilibria. *Phys. Plasmas* **1**, 3262–3268.

Hayashi, T., Sato, T. & Takei, A. (1990). 3D studies of helical equilibria and magneti surface breaking due to finite beta effect. *Phys. Fluids B* **2**, 329–337.

Hazeltine, Richard D. & Waelbroeck, François L. (1998). *The Framework of Plasma Physics*, volume 100 of *Frontiers in Physics.* Perseus Books, Reading, Massachusetts.

Hegna, Chris C. & Bhattacharjee, A. (1989). Magnetic island formation in three-dimensional plasma equilibria. *Phys. Fluids B* **1**, 392–397.

Hender, T. C., Carreras, B. A., L., Garcia, Rome, J. A. & Lynch, V. E. (1985). The calculationof Stellarator Equilibria in Vacuum Flux Surface Coordinates. *Journal of Computatinoal Physics* **60**, 76–96.

Hirshman, S. P. & Meier, H. K. (1985). *Physics of Fluids* **28**, 1387.

Hirshman, S. P., van Rij, W. I. & Merkel, P. (1986). Three-dimensional Free Boundary Calculations using a Spectral Green's Function Method. *Computer Physics Communications* **43**, 143–155.

Holdren, J. P. (1978). Fusion Energy in Context: Its Fitness for the Long Term. *Science* **200**, 168.

Hudson, S.R. & Dewar, R.L. (1997). Manipulation of Islands in a Heliac Vacuum Field. *Physics Letters A* **226**.

Ichiguchi, K., Nakajima, N. & Gardner, H. J. (1996). Free-Boundary Studies for the Large Helical Device. *Nuclear Fusion* **36**, 1157.

Kruskal, M. D. & Kulsrud, R. M. (1958). Equilibrium of a Magneticall Confined Plasma in a Toroid. *The Physics of Fluids* **1**, 265–274.

Lloyd, S. S., Gardner, H. J., Hayashi, T. & Hudson, S. R. (1997). Self-Healing of Magnetic Islands in a Heliac. In *Joint Conf. ISC-11 and ITC-8.*

Mourogov, Victor M. (1997). Nuclear power development: Global challenges and strategies. *IAEA Bulletin* **39**.

Nührenberg, J. & Zille, R. (1984). In *in Stellarators (Proc. 5th Int. Workshop Schloss Rinberg)*.

Park, W., Monticello, D. A., Strauss, H. & Manickam, J. (1986). Three-dimensional Stellarator Equilibrium as an Ohmic Steady State. *Phys. Fluids* **29**, 1171–1175.

Priddle, Robert (1997). Good signs for sustainable development: Nuclear energy's contributions. *Fusion Technology* **39**.

Priddle, Robert (1999). Energy and Sustainable Development. *IAEA Bulletin* **41**.

Reiman, A. & Greenside, H. (1986). Calculation of Three-dimensional MHD Equilibria with Islands and Stochastic Regions. *Computer Physics Communications* **43**, 157–167.

Reiman, A. H. & Boozer, A. H. (1984). Island Formation and Destruction of Flux Surfaces in Three-dimensional MHD equilibria. *Pysics of Fluids* **27**, 2446.

Sears, Francis W, Zemansky, Mark W. & Young, Hugh D. (1987). *University Physics*, chapter 11.5. Addison-Wesley, Reading, Massachusetts, seventh edition.

Solovev, L. S. & Shafranov, V. D. (1970). *Reviews of Plasma Physics* **5**, 1.

T.J. Dolan, T.J., D.P. Jackson, D.P., Kouvshinnikov, B.A. & D.L., Banner (1995). Global co-operation in nuclear fusion: Record of steady progress. *IAEA Bulletin* **37**.

Van Milligen, B.P., Van Lammeren, A.C.A.P., Lopes Cardozo, N.J., Schüller, F.C. & Verreck, M. (1993). Gradients of electron temperature and density across $m = 2$ islands. *Nuclear Fusion* **33**, 1119–1132.

White, R. B. (1989). *Theory of Tokamak Plasmas*, chapter 3. North-Holland Physics, Amsterdam.